Study of deep–inelastic scattering events with a jet at high pseudorapidities

Dem Fachbereich Physik
der Universität Dortmund
zur
Erlangung des akademischen Grades eines
Doktors der Naturwissenschaften
vorgelegte

DISSERTATION

von
M. Sc. Jesús Guillermo Contreras Nuño

Dortmund
Mai 1997

Gedruckt mit Unterstützung des Deutschen Akademischen Austauschdienstes

To my parents.
To you.

Preface

The current understanding of the structure of matter is based on the marriage of the parton model, proposed in the late 1960's, with the idea of asymptotic freedom in nonabelian gauge theories from the early 1970's leading to the birth of quantum chromodynamics (QCD), which in the last two and a half decades has become a basic ingredient of the standard model of particle physics.

Deep–inelastic scattering (DIS) experiments where a high energetic electron (e) scatters off a proton (p) have played a key role in this development. At the beginning, they triggered the appearance of parton model ideas to explain the scaling behavior observed in the first DIS measurements done at SLAC in 1967 [1], and then, under the assumption that DIS processes factorize, allowing to test the predictions of perturbative QCD (pQCD), helping thus to establish it as the theory of the strong nuclear force [2].

Keeping up with this tradition the ep collider HERA has opened a new kinematic domain which makes it possible to test the limits of the standard pQCD evolution of partons (quarks and gluons) inside the proton (called DGLAP evolution) and offers exciting prospects in the search for processes which go beyond it. In this context A.H. Mueller proposed to look for DIS events at small x with an energetic jet at high rapidities – so called forward jet [13]. This signature was designed to mark the end of the applicability of DGLAP evolution and the set in of pQCD á la BFKL.

The present work is concerned with the measurement of this kind of events and with the analysis of their characteristics. In the first chapter the phenomenological differences between the BFKL and DGLAP approaches are introduced and used to define Mueller's proposal whose signature consist of an scattered electron at low x and a jet produced at high rapidities. Furthermore the observables measured in this work will be presented here. The second chapter describes the components of the H1 detector which are needed to measure these events. For the HERA reference frame the electron is scattered backward and the jet produced forward, allowing to measure them independently, so in this chapter and the next two, the issues related to the electron will be treated first and then those related to the forward jet. The cuts used to select the data and their experimental and/or phenomenological motivation will be explained in chapter 3. Chapter 4 deals with the understanding of the selected data, the subtraction of the background, the estimation of the errors and how the data is corrected for detectors effects. The corrected cross sections of the measured observables introduced in chapter 1 will be shown in chapter 5 and they will be confronted to expectations from Monte Carlo models and analytical calculations. A short summary concludes this work

Acknowledgments

During my time as *Doktorand* I have enjoyed and benefited from the knowledge, helpfulness and friendship of many people. I can not name them all, but I thank all and every one of them.

To the Physics Department of the CINVESTAV–IPN, the CONACyT (both in Mexico), the DAAD (Deutscher Akademischer Austauschdienst) and the Bundesministerium für Bildung und Forschung, FRG (contract number 6DO571) for their support …

the crew of the HERA machine who provide the luminosity …

the members of the H1 collaboration who designed, built and keep running the detector …

all my colleagues from Dortmund University who were every time ready to help me, in spite of my needing help quite often …

Manfred and Joachim who read early versions of this work and whose comments and suggestions helped so much …

Ewelina, Jürgen and again Joachim who spent so many hours hunting forward jets with me …

Albert de Roeck who was involved in every single step of this analysis, from the conceptual stages to the final corrections to this work …

Prof. Buchholz who kindly accepted to be correferent of this work …

Karin, Jo, Raúl and Roman who make Hamburg such a wonderful place to live in …

Javier, Miguel Angel Peréz and Rubén for reasons they well know …

Herr and Frau Wegener who not only gave me the chance to come to Germany, but also gave me their help, support and hospitality …

my sister, my brother and especially to Monika and my parents …

… thank you, thank you very much!

J. G. C. N.
Hamburg,
February 1997

Contents

List of Figures

List of Tables

Chapter 1

Introduction

After a brief historical review, the idea of deep–inelastic scattering (DIS) experiments is presented along with the definition of some kinematic variables. Next, the main phenomenological features of leading log (LL) approximations of perturbative quantum chromodynamics (pQCD) are explained and used to discuss experimental signatures to look for at HERA; especially A.H. Mueller's proposal of DIS events with an energetic jet at high pseudorapidity – a so called forward jet, which are the subject of this work.

1.1 The quest for fundamental particles

The idea that matter is formed out of a few basic building blocks and forces which hold them together had its origin in philosophical speculations and has established itself through the history of modern science (see table 1.1) as a cornerstone of our understanding of the structure of matter.

The standard model, which is the current paradigm to explain nature at a fundamental level, is a quantum field theory where the view that two types of components – particles and forces – are enough to describe all the material world is realized through fermionic and bosonic fields respectively (see table 1.2).

There is an important difference between the fermionic fields for leptons and quarks: the former can be observed as free particles – for example electrons and positrons – but

Models	**Building Blocks**	**Forces**
Democritus	∞ Atoms	Mechanic
Aristotle	4 Elements	Mixture
Chemistry	$\mathcal{O}(100)$ Elements	Electricity
Standard Model	12 Fermions	13 Bosons

Table 1.1: Examples of fundamental forces and building blocks of matter through history. Neither Democritus nor Aristotle, had a concept for a force – at least not in today's sense – to hold the basic building blocks together. Nevertheless from our current perspective the idea that the atoms were held together via hooks (Democritus) corresponds to a mechanical force, while for Aristotle by mixing in different proportions and quantities of the basic elements the observed diversity of material objects was attained.

Fields		
Fermions		**Bosons**
Leptons	**Quarks**	
e, μ, τ	u, c, t	γ, Z^0, $W^\pm$
ν_e, ν_μ, ν_τ	d, s, b	8 gluons, H

Table 1.2: The fields of the Standard Model.

the latter, due to the nonabelian nature of the strong interaction, can not, i.e. they are *confined*, appearing only in the form of hadrons, which are bound states composed of two or three valence quark fields – for example the proton consists of one down and two up valence quark fields.

1.2 Deep–inelastic scattering experiments

What structure do hadrons have? How are their constituents distributed? What holds them together? Deep–inelastic scattering (DIS) experiments approach these questions using a leptonic probe on the hadron under study. They are made to collide at high energies such that the boson which mediates the interaction carries enough momentum to resolve the partonic structure of the hadron, kicking off one of its quarks, who due to confinement produces particles – this process is called hadronization – which are then detected.

Collider experiments have almost a 4π coverage in the laboratory reference frame and when looking for DIS events their task is first to find the scattered lepton (or lack of it in the case of neutrinos) used as a probe, and then to detect all other particles and use them to perform detail studies of the structure of the hadron.

The present analysis considers the case where the lepton is an electron or a positron[1], the hadron is a proton and the boson which mediates the interaction is a photon. Figure 1.1 shows an schematic representation of such DIS process.

In HERA there is a redundancy in the measurement of kinematic variables and they can be determined through different methods [3, 4, 5]. The present analysis used the electron method, because it offers the best resolution for the kinematic region studied here. In this method the measured energy E_e and polar angle θ_e of the scattered lepton are used along with the energies of the incoming proton p_0 and electron k_0 to determine the kinematic variables according to (*cf.* fig. 1.1):

- Total energy in the ep center of mass system:

$$\begin{aligned} s &= (k_\mu + p_\mu)^2 \\ &= 4k_0p_0. \end{aligned} \tag{1.1}$$

---

[1] Both were used at HERA during 1994, but for this analysis there is no difference between them, so in the following the terms electron, positron and lepton will be used interchangeablely

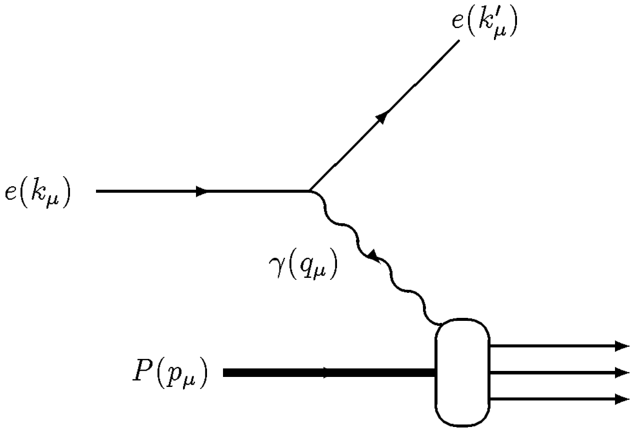

Figure 1.1: Schematic representation of a DIS process. The incoming lepton with momentum k_μ interacts with the hadron P(p_μ) through a boson $\gamma(q_\mu)$ and is scattered with momentum k'_μ.

- Square of the transferred four momentum:

$$\begin{aligned} Q^2 &= -q_\mu q^\mu \\ &= -(k_\mu - k'_\mu)^2 \\ &= 4E_e k_0 \cos^2(\frac{\theta_e}{2}). \end{aligned} \tag{1.2}$$

- Energy transferred in the proton rest frame:

$$\begin{aligned} y &= \frac{pq}{pk} \\ &= 1 - \frac{E_e}{k_0}\sin^2(\frac{\theta_e}{2}). \end{aligned} \tag{1.3}$$

- Fraction of the longitudinal momentum of the proton carried by the struck quark in the naive quark–parton model, normally called x–Bjorken:

$$\begin{aligned} x &= \frac{Q^2}{2pq} \\ &= \frac{Q^2}{sy}. \end{aligned} \tag{1.4}$$

In equations (1.1) to (1.4) the masses of the electron and the proton have been neglected. The convention adopted here is to measure polar angles with respect to the proton direction which defines the z–axis. Small (big) polar angles define the forward (backward) direction. Given that at HERA s is fixed, only two of these variables are independent. It is common practice to choose x and Q^2 to describe DIS.

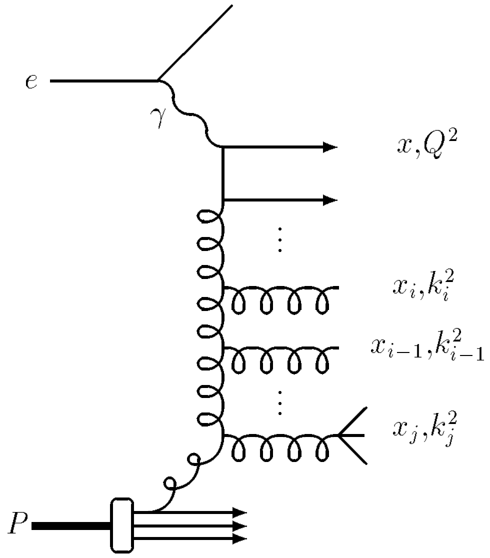

Figure 1.2: Ladder representation of a DIS process. The longitudinal and the square of the transverse momenta of parton i are labeled by x_i and k_i^2 respectively

1.3 Leading log approximations

To treat DIS from the theoretical point of view, its necessary to use a factorization theorem [6] to separate the nonperturbative part of the process which has to be provided by experiments in the form of parton distributions in x and Q^2, from the hard part which can be approximately calculated using pQCD either in the form of matrix elements (ME) obtained by operator product expansion (OPE) techniques [7] or parton showers (PS) from a parton evolution prescription [10, 11].

To date the ME can only be calculated to the first very few orders and they have to be completed with PS which sum all orders, but consider only (next to) leading logarithmic terms in the expansion variable. Using a physical gauge DIS process in a leading log (LL) approximation can be represented in pQCD by ladder diagrams like the one shown in figure 1.2 (see for example pages 32 to 34 in ref. [8]), where the quark box on top is calculated within the OPE formalism and the ladder itself comes from the evolution of the parton distributions inside the proton at a given initial scale x_0, Q_0^2 to the x and Q^2 of the interaction.

Summed Terms	**DGLAP**	**BFKL**
$(\alpha_s \ln \frac{1}{x} \ln Q^2)^n$	Yes	Yes
$(\alpha_s \ln Q^2)^n$	Yes	No
$(\alpha_s \ln \frac{1}{x})^n$	No	Yes

Table 1.3: Considered terms in LL resummations of pQCD.

There are two approaches to LL pQCD[2]: DGLAP[10] and BFKL [11]. They sum different terms of the perturbative series (see table 1.3), thus they are also often referred to as the LL Q^2 or LL $1/x$ approximations. Both are based on evolution equations of the general form

$$\frac{\partial f(a,b)}{\partial \log a} = \int da' \mathcal{K}(a,a') f(a',b), \tag{1.5}$$

where the kernel $\mathcal{K}$ gives the prescription to take the parton distribution f from the point (a',b) to (a,b). As any integro–differential equation they need a boundary condition. This boundary condition is not known from the theory and it has to be given by the experiment in a coordinate a_0 for the whole range in b. The problem is that experiments have only measured part of the available phase space, so extrapolations based on parameterizations or in some theoretically motivated *Ansatz* have to be used, introducing therefore an uncertainty on the pQCD predictions.

From the phenomenological point of view there is a characteristic behavior for each of these two formalisms that may allow to distinguish one from the other. The following differences between them [12, 13] will be used in the course of this investigation (*cf.* fig. 1.2):

- Ordering of the longitudinal momenta of the partons along the ladder.
  - DGLAP: $x_i < x_{i-1}$.
  - BFKL: $x_i \ll x_{i-1}$.
- Ordering of the square of the transverse momenta of the partons along the ladder.
  - DGLAP: $k_i^2 \gg k_{i-1}^2$.
  - BFKL: $k_i^2 \sim k_{i-1}^2$.
- Range of applicability.
  - DGLAP: medium to high x.
  - BFKL: very small x.

These differences are summarized in table 1.4. The numerical meaning of very small x is not precise, so its not clear when DGLAP should cease to be applied and BFKL effects would start to set in. Fixed target experiments have reached $x \sim \mathcal{O}(10^{-3})$ and calculations using the DGLAP equations have been quite successful in describing the measured data for a variety of observables. On the other hand HERA has opened a completely new kinematic domain reaching values of x several orders of magnitude smaller than in fixed target experiments (see figure 1.3). Therefore the natural question is if the onset of the BFKL paradigm can be detected at HERA.

---

[2] There is a third approach which in the appropriate limits reproduces the other two [9]. This third option will not be discussed here further, because this work concentrates on the phenomenological differences between the BFKL and the DGLAP approaches.

BFKL	**DGLAP**
$x_i \ll x_{i-1}$	$x_i < x_{i-1}$
$k_i^2 \sim k_{i-1}^2$	$k_i^2 \gg k_{i-1}^2$
$x \ll 1$	$x < 1$

Table 1.4: Phenomenological differences between the BFKL and the DGLAP approaches

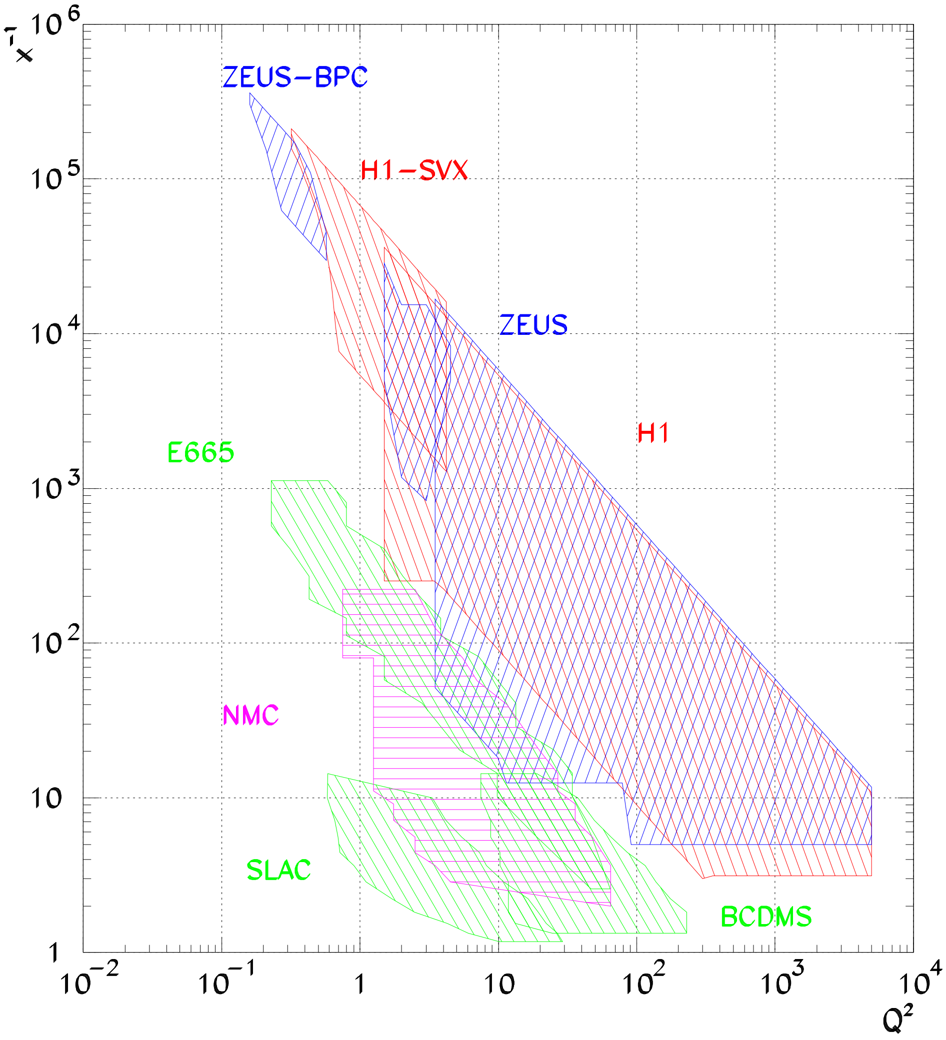

Figure 1.3: Kinematic reach of HERA experiments, H1 and ZEUS, compared to the fixed target experiments E665, NMC, SLAC and BCDMS. The labels H1–SVX and ZEUS–BPC stand for dedicated methods used by the H1, respectively ZEUS, collaborations to extend their kinematic reach.

1.4 Leading log $1/x$ signatures at HERA

Using the phenomenological behavior summarized in table 1.4, three footprints of BFKL dynamics will be discussed in the following subsections. The most inclusive one, corresponding to look only at the upper part of figure 1.2, is just to measure the dependence on x of the total cross section, or equivalent of F_2 (see for example [14, 15]). Another possibility is to look at the transverse energy (E_T) flow along the ladder and the third option is to perform an exclusive measurement selecting DIS events with a jet at high pseudorapidities.

1.4.1 Rise of F_2 at low x

At low x the most dominant parton distribution is that of the gluon $g(x,Q^2)$ which from the point of view of evolution equations is expected to have the following behavior:

BFKL Solving the evolution equation for fixed running coupling $\overline{\alpha_s}$ leads to

$$xg(x,Q^2) \sim x^{-\lambda} \tag{1.6}$$

where

$$\lambda = \frac{12\ln(2)}{\pi}\overline{\alpha_s} \tag{1.7}$$

with a typical value of $\lambda = 0.5$. If the running coupling effects are taken into account the exponent λ has to be calculated numerically yielding slightly lower values which are dependent upon a infrared cutoff [16, 17, 18, 19].

DGLAP Here there are two schools of thought: Parametrizations and dynamical generation.

Parametrization: These groups parameterize input parton distributions at a given scale, say $Q_0^2 = 4$ GeV^2 using all existing data[3] and then extrapolate to new kinematic domains. They expect the same functional form as in equation 1.6 with either $\lambda \approx 0$ or $\lambda \approx 0.5$ depending on the use of conventional ($xg(x,Q_0^2)$ $\sim$constant) or BFKL inspired ($xg(x,Q_0^2) \sim x^{1/2}$) initial gluon distribution [22, 23].

Dynamical generation: This is the GRV approach which postulate theoretically motivated parton distributions at $Q_0^2 = 0.3$ GeV^2 [24]. Their gluon distribution for x tending to zero and Q^2 tending to infinity generates a form [25]

$$xg(x,Q^2) = \exp\left[\sqrt{\frac{144}{33-2N_f}\ln\left(\frac{\ln(Q^2/\Lambda^2_{QCD})}{\ln(Q_0^2/\Lambda^2_{QCD})}\right)\ln\left(\frac{1}{x}\right)}\right] \tag{1.8}$$

---

[3] The newest parameterizations of the CTEQ ($Q_0^2 = 0.5$ GeV^2) [20] and MRS ($Q_0^2 = 1$ GeV^2) [21] groups use a lower initial value of Q_0^2.

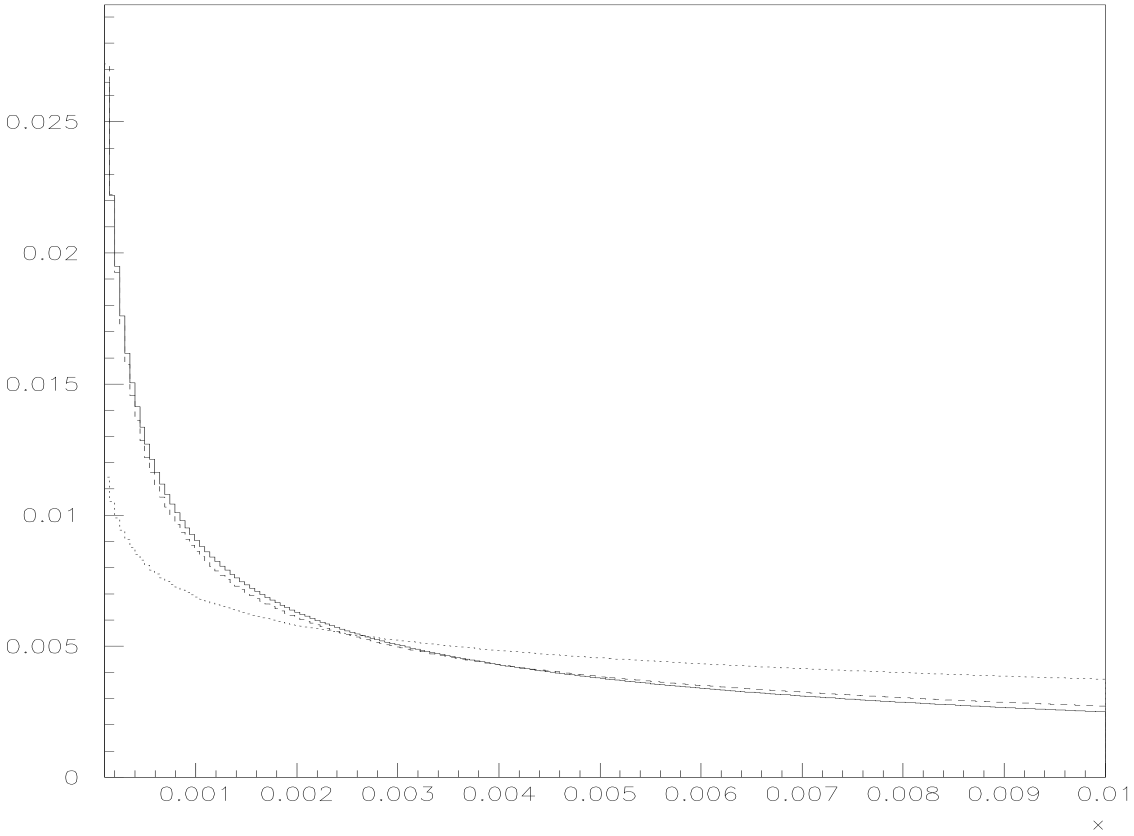

Figure 1.4: Shape of $xg(x, Q^2)$ at small x according to the GRV approach (equation 1.8) for $Q_0^2 = 0.3$ GeV^2 and $Q^2 = 20$ GeV^2 (solid line), and for $Q_0^2 = 5.0$ GeV^2 (dotted line) compared to the BFKL expectation (equation 1.6) for $\lambda = 0.5$ (dashed line). Each curve was normalized to one to compare their shapes. The values used are for N_f=5 and $\Lambda_{QCD} = 0.2$ GeV.

> where N_f is the number of flavors involved in the process. Note that because the Q^2 evolution is started at so small scale Q_0^2, there is enough phase space to generate partons, and this equation produces within the HERA kinematic range a slope of the gluon distribution about that predicted by the BFKL scheme (equation 1.6) as shown in figure 1.4.

The first results from HERA [26, 27, 30] showed a rise of F_2 for decreasing x ruling out the extrapolations based on a $\lambda \sim 0$ and being consistent with BFKL inspired models and the DGLAP prediction á la GRV. The ZEUS and H1 collaborations have refined their results increasing their precision and the number of measured bins in the (x, Q^2) plane reporting an excellent agreement with expectations based on DGLAP [28, 29]. For example the H1 collaboration has produced a parameterization of its data plus fixed target experiment results [29], based on next to leading log DGLAP evolution which describes the measurements perfectly over several orders of magnitude in x and Q^2. Furthermore this fit was performed using only data with $Q^2 > 5$ GeV^2 and the backward evolution

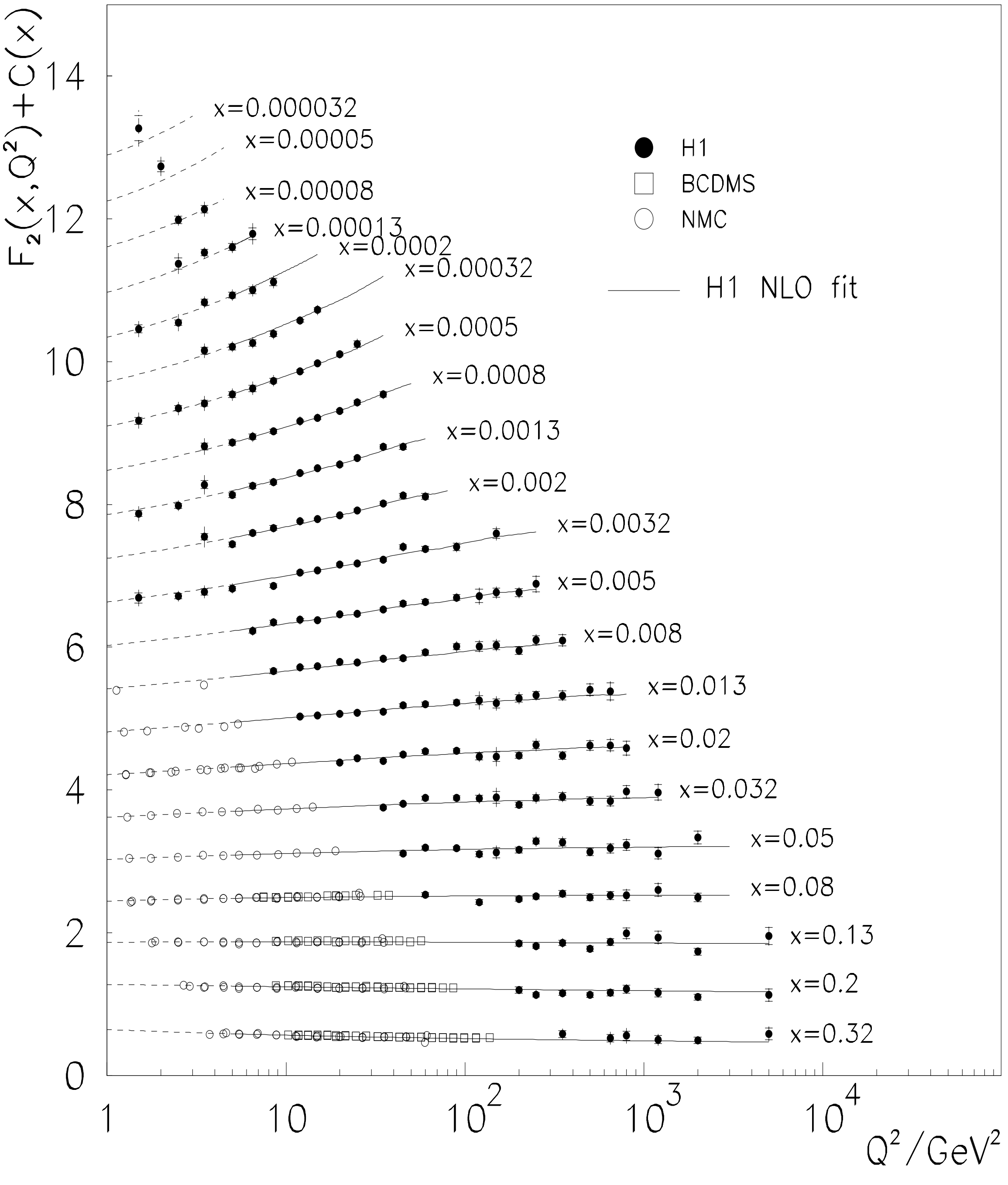

Figure 1.5: H1 and fixed target data on F_2. The full line corresponds to the H1 fit based on next to leading order DGLAP equations. The extension of the curves below 5 GeV^2 (dashed line) represents the backward evolution of the fit. The F_2 values are plotted in a linear scale adding a constant $c(x) = 0.6(i - 0.4)$ where i is the x bin number starting at $i = 1$ from $x = 0.32$. [29].

from this scale describes perfectly the data below $Q^2 = 5$ GeV^2 as shown in figure 1.5.

It has recently been shown that a pure BFKL approach is not enough to describe the new HERA data [31]. So in spite of the success of BFKL inspired models to reproduce the first HERA results, given the current error bars only the DGLAP approach describes the behavior of F_2.

1.4.2 E_T flow

Due to the difference between the ordering of the square of the transverse momenta along the ladder in the DGLAP and BFKL cases (see table 1.4) the measurement of the E_T flow between the struck quark and the remnant was thought to be a good candidate to discriminate between both formalisms. There were two observables proposed. The pure E_T flow, i.e. the measurement of the amount of transverse energy per unit of pseudorapidity η, defined for a four vector p_μ as[4]

$$\begin{aligned} \eta &= \frac{1}{2}\ln\left(\frac{|p| + p_z}{|p| - p_z}\right) \\ &= -\ln\left(\tan\left(\frac{\theta}{2}\right)\right), \end{aligned} \tag{1.9}$$

where θ is the polar angle of the object having momentum p_μ. As the pseudorapidity is related to the longitudinal momentum of the parton i in the ladder (for large pseudorapidity $\eta_i = \ln(x_i/x)$) it was expected that for large x_i and small x the total E_T would be larger for the BFKL than for the DGLAP case [36]. The other observable consisted in averaging the E_T in a central bin in pseudorapidity in the hadronic center of mass system (corresponding to the forward direction – large pseudorapidities – in the HERA frame) and looking at its x dependence for fixed Q^2: the bigger x is, the less remaining phase space for BFKL evolution and thus the less E_T, meanwhile for the DGLAP case there is not much change (the ordering in the longitudinal momentum along the ladder is softer; see table 1.4) and analytical calculations show that indeed, for the DGLAP case the average E_T for fixed Q^2, in contrast to the BFKL behavior, increases slightly with increasing x [36].

In 1994 the H1 collaboration published its measurement of E_T flows as a function of pseudorapidity η [32]. The data were presented for two ranges in x (see figure 1.6) and compared to different Monte Carlo (MC) generators (see section 4.1) with the conclusion that the DGLAP based MCs (labels MEPS and HERWIG in the figure) do not describe the data especially for the lowest x bin and the only MC which followed the data was ARIADNE [33] (label CDM) which it is based on a color dipole model (CDM). This model has been claimed to be a kind of effective BFKL model [34, 35], because it does not have a strong ordering in the square of the transverse momenta of the radiated partons.

---

[4] The rapidity $y = \frac{1}{2}\ln((E + p_z)/(E - p_z))$ has the property that it changes only in a constant factor when a Lorenz transformation along the z axis is applied to it. Thus differences of rapidities are in this case invariant. For massless objects rapidity and pseudorapidity are equivalent.

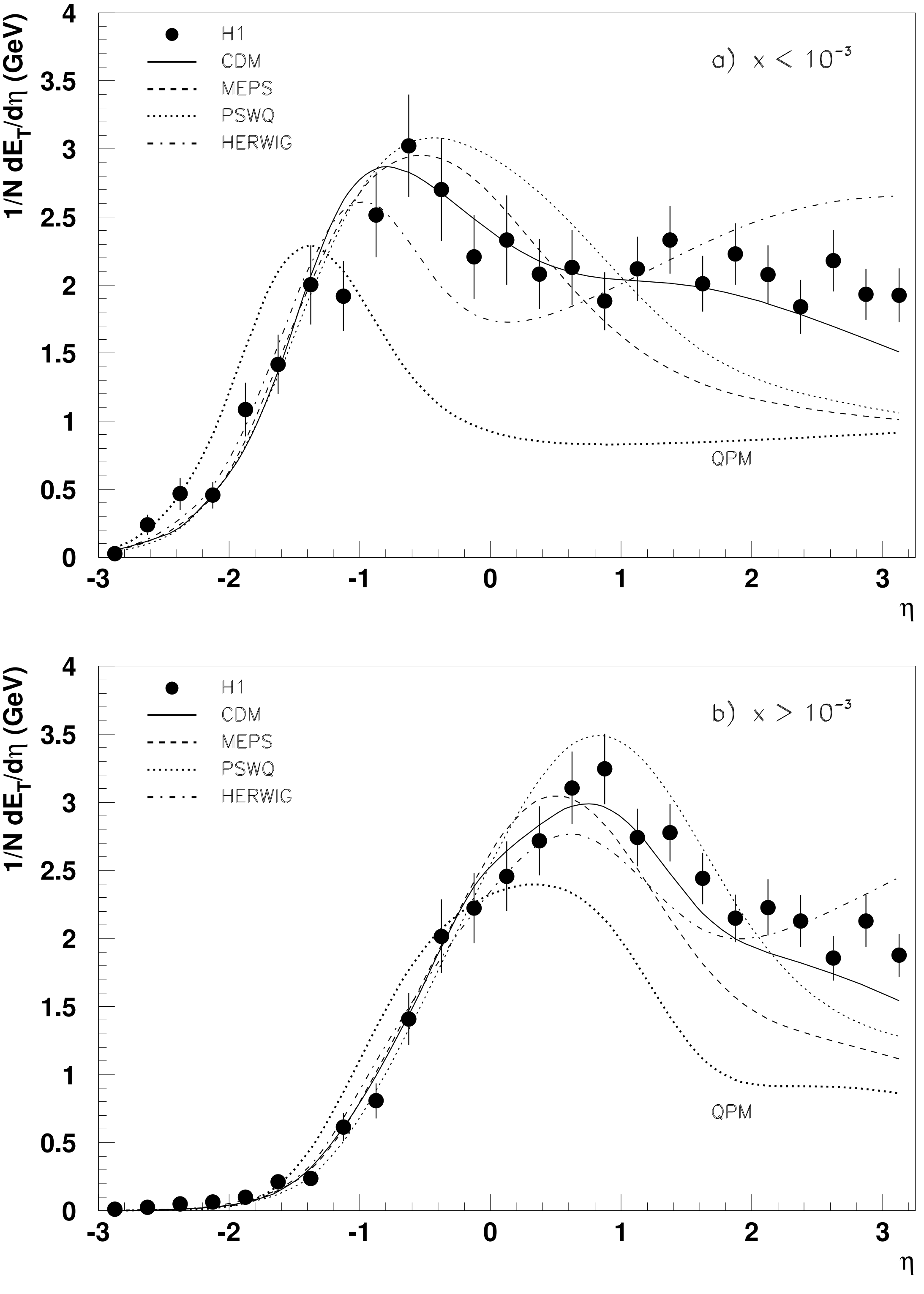

Figure 1.6: E_T flow as a function of pseudorapidity for two ranges in x measured by the H1 collaboration [32] compared to different MC predictions: CDM [33], MEPS, PSWQ [39] and HERWIG [83].

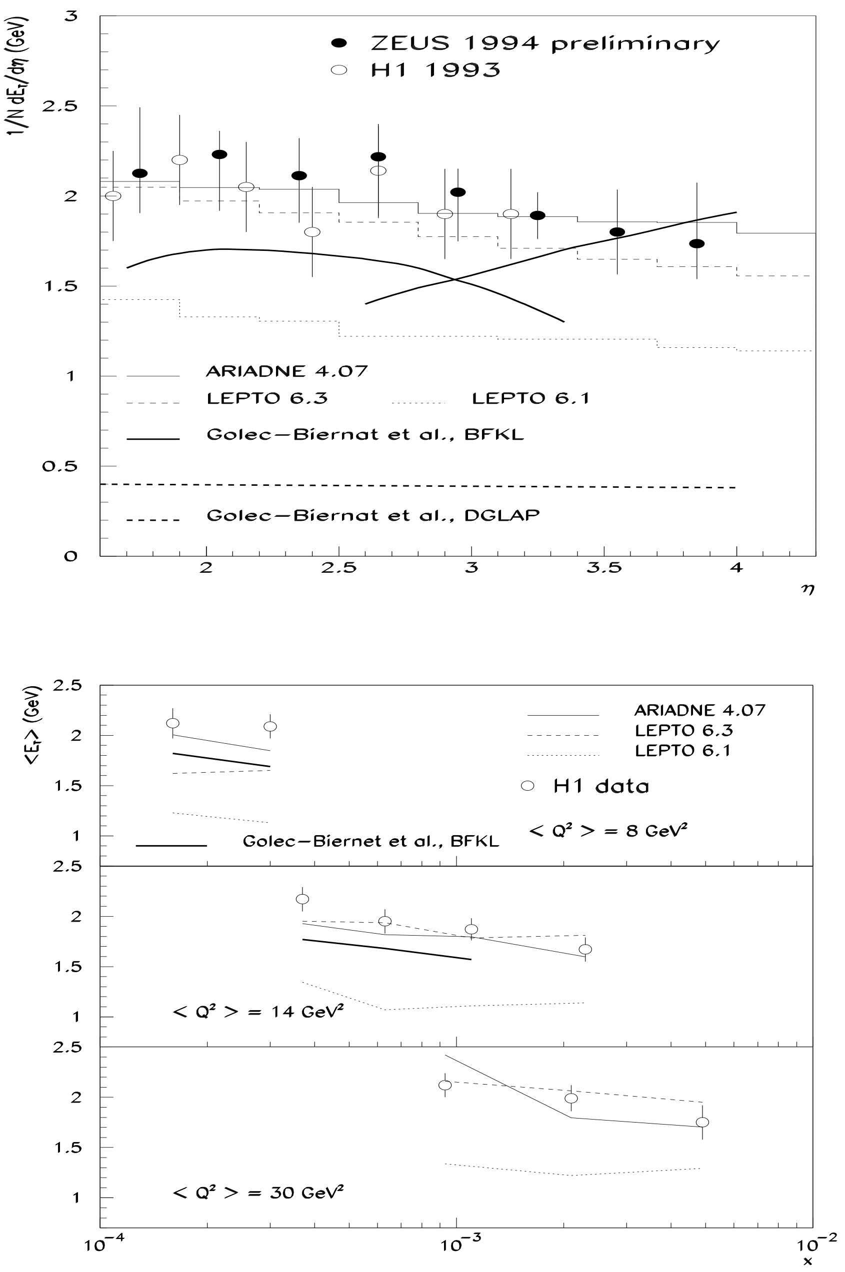

Figure 1.7: The two E_T flow observables defined in the text measured by the H1 collaboration against different MC predictions in particle level and analytical calculations in parton level [36, 37, 38].

Simultaneously analytical calculations for both cases were presented [36] supporting a BFKL explanation of the measured E_T flow. Here should be stressed that these calculations are done at parton level, i.e. don't include hadronization effects, so to compare them directly to the measured data which are corrected only for detector effects, is somewhat arbitrary and prevents drawing strong conclusions. Another point to stress is that these calculations are only valid in the middle of the ladder, and can be performed approaching from the remnant side or from the struck quark side, causing an uncertainty in the prediction (see solid line in the upper plot of figure 1.7). The results for the second observable mentioned above (the measurement of the x dependance of the average transversal energy in a pseudorapidity between -0.5 and 0.5 in the hadronic center of mass system) also showed (see lower plot of figure 1.7) that the CDM and BFKL calculations followed the data, whereas the DGLAP based MCs did not [36, 37, 38].

But there have been developments in the area of MCs which allowed a better description of the measured data. An example is the DGLAP based LEPTO MC [39] (also labeled MEPS in figure 1.6) which shows a greatly improved behavior from version 6.1 to 6.3 [40]. The behavior of both versions of LEPTO, the analytical calculations and the data are depicted in figure 1.7. The change in the predictions of LEPTO from version 6.1 to version 6.3 are mainly due to the new sea quark treatment (see section 4.1).

The fact that MCs could show such a dramatic change in its predictions of E_T flows without touching their implementation of the DGLAP equations weakened the implications of the analytical calculations and posed the question of the suitability of this observable to discriminate between the BFKL and DGLAP approaches.

1.4.3 Forward jets in DIS events

Sometime ago A.H.Mueller proposed [13] to look at DIS events with one jet (which should not be the current jet coming from the struck quark) fulfilling the following characteristics (*cf.* fig. 1.2):

x_j large: This requirement enables the use of parton distribution in a domain where they have already been experimentally measured, reducing thus one of the biggest theoretical sources of uncertainty from the measurement. For the HERA reference frame this requirement also means that the jet is produced forward, hence the name for these events.

x small: Selecting the smallest x–Bjorken experimentally possible helps in going away from the DGLAP regime and trying to come close to the range of BFKL applicability. Also together with the previous requirement makes available enough phase space for BFKL evolution.

$k_j^2 \sim Q^2$: This selection suppresses DGLAP ladders because of the strong ordering, $k_i^2 \gg k_{i-1}^2$, without affecting the BFKL condition $k_i^2 \sim k_{i-1}^2$. It also keeps the theoretical calculations outside the dangerous infrared zone, providing cut off independent predictions.

As both formalisms require an ordering in longitudinal momenta, these criteria select events with one hard scale at the top of the ladder (Q^2), a hard scale at the bottom (k_j^2), and a big longitudinal phase space ($x \ll x_j$), providing a well defined experimental signature and a clear perturbative process for the calculation of theoretical predictions [41, 42, 43, 44, 45]. In particular the authors of [45] have performed their calculations precisely taking into account the selection criteria used in this analysis.

1.5 Measurements presented in this work

Here the following observables will be studied in the frame of the forward jet proposal of A. H. Mueller:

- As already pointed out the smaller the x reached the closer to the region where BFKL effects are expected and the farther away from the range of validity of the DGLAP approach (see table 1.4). The first measurement here presented consists thus in studying the behavior of the cross section as x varies. Due to the suppressed phase space in DGLAP with respect to BFKL a difference in rate between both cases is expected [45]. The H1 collaboration has already published the first measurement of this observable [38] using data taken in 1993 and preliminary results of the analysis using data taken in 1994 [46]. The present study continues this effort with increased statistics which allowed the selection of cuts closer to the philosophy of Mueller's proposal and also permitted to have a finer binning in x. Furthermore this observable is presented for the first time for different bins in the jet energy – equivalent to x_j – and in the amount of energy between the scattered lepton and the forward jet. The stability of the result for different hardness of the forward jets is also presented.

- Due to the different ordering of the squared of the transverse momentum of the radiation along the ladder for the DGLAP and BFKL cases, it is expected that the naive quark–parton model correlation between the azimuthal angles of the scattered lepton and the forward jet is weaker for the latter evolution prescription than for the former [45]. The measurement of this observable is here for the first time presented. Also studies of its dependence on the amount of energy between the scattered lepton and the forward jet and its dependence on x are shown.

- Finally and also for the first time the cross section for events having two forward jets is presented along with some comments on the behavior of such events.

Chapter 2

The H1 detector

The signature proposed by Mueller consist first of a neutral current (NC) DIS event at low x, that means an scattered electron at high polar angles (*cf.* eqs. 1.2, 1.4), and second, of a jet at high pseudorapidity i.e. small polar angles (*cf.* eq. 1.9). These conditions define the sub detectors of H1 to be used to perform the measurement: first the time of flight system (ToF) and the central jet chambers (CJC) to select an event, then the backward proportional chamber (BPC) and the backward electromagnetic calorimeter (BEMC) to measure the scattered lepton and finally the liquid argon calorimeter (LAr) to identify the forward jet. After a short introduction to HERA and the triggering scheme of H1, these sub detectors will be briefly discussed in this chapter along with a short description of the H1 luminosity system needed to normalize the measured rate to the cross section. The next two chapters explain how they are used to select the data and discuss their responses to the events.

2.1 HERA

The HERA facility [47] is the first electron–proton (ep) collider ever built. It has a circumference of 6336 m where independent accelerators store 820 GeV protons using superconducting magnets, and electrons or positrons with an energy of 27.5 GeV in 1994. It is supported by an injection complex which includes a 500 MeV linac, DESY II and the modified PETRA II ring as preaccelerators for the leptons and a 50 MeV linac, DESY III and PETRA II for the protons. Some of HERA parameters during 1994 are listed in table 2.1.

There are four interaction regions in HERA where two general purpose detectors, H1 [49] and ZEUS [50], and two dedicated experiments, HERA–B [51] for the study of CP–violation and HERMES [52] to investigate polarized structure functions are installed. In what follows only the H1 detector will be discussed.

2.2 Overview of the H1 Detector

A diagram of the H1 detector showing the relative position of each sub detector is found in figure 2.1, and a close up of the backward part is shown in figure 2.2. Note that sub detectors which play no role in the present analysis will not be discussed here; information

Parameter	$e^{\pm}$ beam	p beam
Beam energie (GeV)	27.5	820.0
Number of colliding bunches	153	153
Number of pilot bunches	15	17
Number of empty bunches	42	40
Average current (mA)	17.1	41.0
Maximal luminosity (10^{30}cm^{-2}s^{-1})	3.2	
Distance between bunches (ns/m)	96/28.8	

Table 2.1: Some HERA parameters during 1994 [48]. Pilot bunches are those which do not have a partner to collide with.

about them along with more details of the components of H1 which are described in this chapter can be found in [49] and references therein.

The H1 detector is a complex conglomerate of subdetectors built around the point IP (see figures 2.1 and 2.2) where the electron and positron beams are brought into collision. All values for polar acceptance of the detectors given in this chapter are calculated for an interaction originating precisely at the IP, and will vary a little bit when taking into account that the actual interactions happen in an interval around the IP. The clear asymmetry seen in the design of the detector is due to the boost caused by the different energies of the colliding beams. Going from the IP outwards there is first a layer of trackers (important for this analysis are CJC and BPC). The next layer consist of calorimeters: BEMC and the inner most part of the LAr calorimeter are designed to measure the energy of electromagnetic showers, while the PLUG calorimeter and the outer part of the LAr calorimeter measure hadronic deposition of energy. All this is surrounded by a superconducting solenoid producing an almost uniform magnetic field of 1.15 T parallel to the HERA beams. The return iron yoke is instrumented and forms the central muon system. Between BEMC and the return yoke a time of flight system (ToF) is located. These subdetectors are complemented by the luminosity system formed by two arms: the electron tagger placed 33 m from the IP in the direction of the electron beam and the photon arm situated 103 m from the IP in the same direction.

2.3 The H1 trigger system.

Due to the smallness of potentially interesting cross sections and the need of high statistics data to do proper studies, high luminosities are required from the accelerator. The approach taken is to have a large number of bunches in the machine, which for the design values of HERA corresponds to have 210 bunches for a total of 2.1(0.8)x10^{13} particles in the proton(electron) ring. There is a collision at the IP every 96 ns.

Problems arise once the following two factors are considered:

- The rate for DIS events was about 5 Hz in 1994, but the most common sources of background, namely the interaction of protons with parts of the accelerator (p–wall

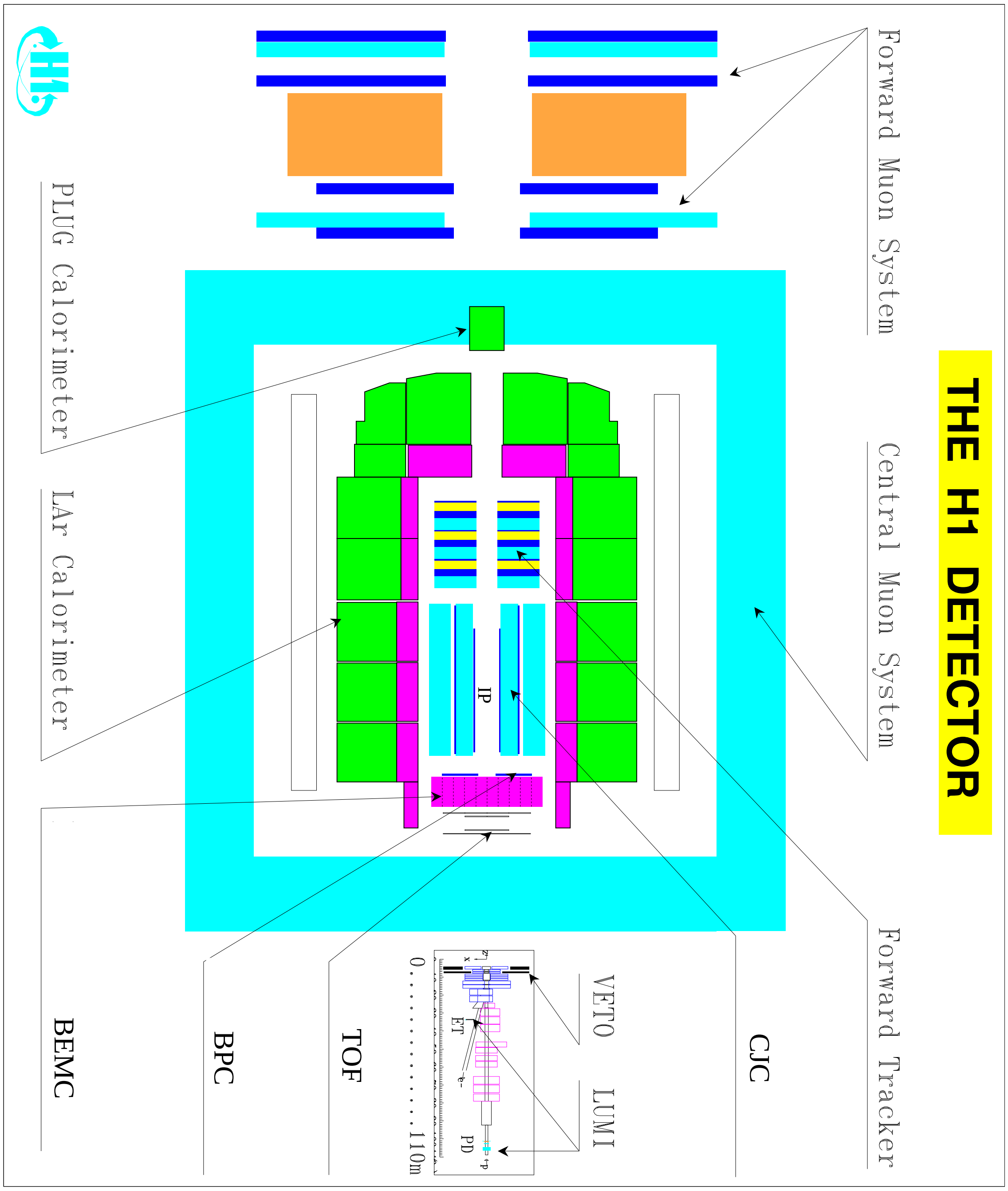

Figure 2.1: The H1 detector. The protons come from the right, the electrons from the left and the collision takes place at the point labeled IP (short for interaction point). Important for this analysis are the time of flight system (ToF), the central jet chambers (CJC), the backward multiwire proportional chamber (BPC), the backward electromagnetic calorimeter (BEMC) and the LAr calorimeter. The luminosity system, shown to the right in the inserted rectangle with a different scale, is used to normalize the rate to a cross section.

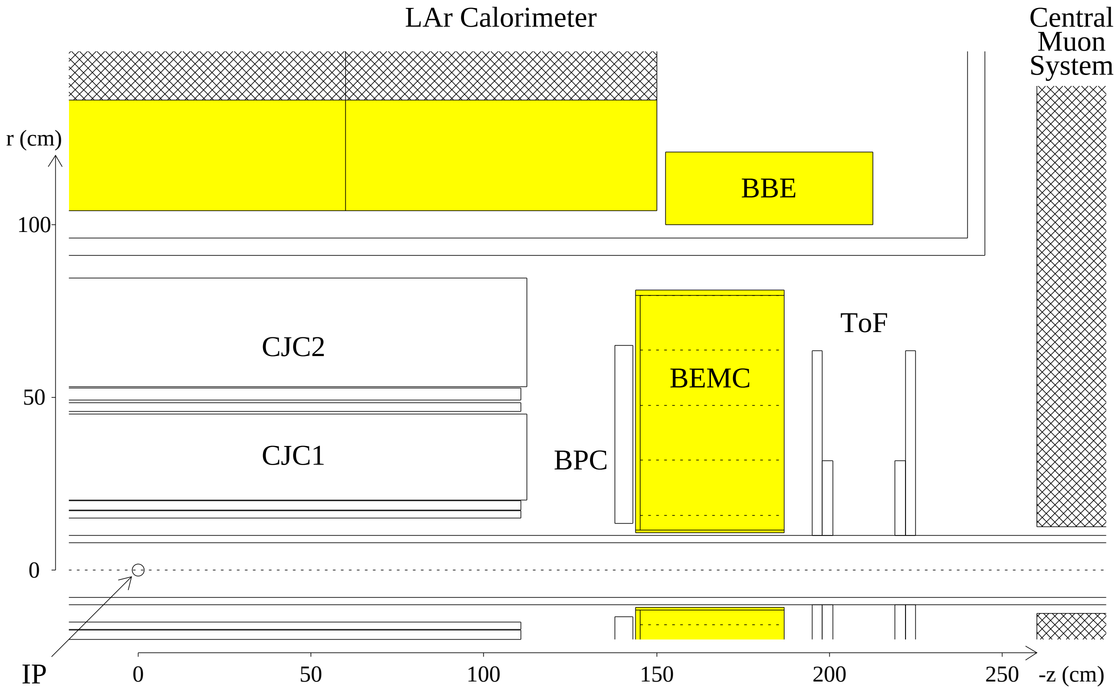

Figure 2.2: View of the backward region of H1. The label IP stands for interaction point and signals the place where the proton (coming from the right) and electron (from the left) beams are brought into collision. Important for this analysis are the time of flight system, the central jet chambers (CJC), the backward multiwire proportional chamber (BPC), the backward electromagnetic calorimeter and the liquid argon calorimeter. Figure from ref. [57].

events) and with the gas remaining in the beam pipe "vacuum" of about 10^{-9} hPa (p–gas events), have rates of $\mathcal{O}(50)$ kHz.

- The time needed to process the signals in the different sub detectors spans from the 250 ns needed by the ToF to produce a signal for the trigger, to the 2.5 μs decision time of the calorimeter trigger chain, to be compared with the 10.4 MHz HERA collision rate.

The solution was to construct a trigger system with multiple layers (see [49, 53] and [54]). For the 1994 data taking period it had only two active levels:

Level 1 The emphasis is to have dead time free processing at this level. Taking into account that the signals from the trigger electronics are available to make a decision after about 2.1μs, a 24 event buffer was used. The system consist of 128 trigger elements, out of which more complicated triggers can be constructed to be used either in this or in other levels.

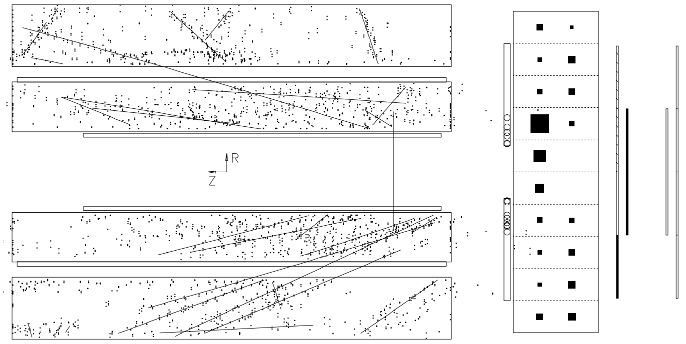

Figure 2.3: A typical background event in H1. It is clearly seen that the tracks reconstructed by the CJC point to a region just before BEMC. Figure from ref. [56].

Level 4 For this level all the information from the detector is available. The same programs used to reconstruct the data are applied at this stage to select or reject events according to the following three criteria:

- The decisions done by the first level trigger are checked using the full reconstructed information from H1. If the decision of the level 1 trigger is corroborated then the event is accepted, otherwise is rejected.
- Clear signals of interesting events, either to control the function of the detector or to select candidates for further analysis are accepted.
- Clear signals of background are rejected.
- 1% of all rejected events are accepted to study the efficiencies of the trigger.

2.4 Detecting a NC DIS event

As already mentioned the rate of background interactions is huge compared to those coming from *ep* collisions and it is necessary to distinguish between them. Due to the longitudinal momentum of the proton beam, *p*–wall and *p*–gas interactions are boosted forward as seen in figure 2.3. So they create a signal in BEMC which may fake the signal of a scattered lepton from an *ep* event, only when they happen before it. As H1 is built around IP, to cut away *p*–wall and *p*–gas background it is required that the extrapolated tracks of some of the particles in an event should join in a vertex around the IP and no vertex lying outside this region of the detector should be found (for the precise cut applied see section 3.2). The task of the CJC with respect to this analysis, is to reconstruct the main vertex of the event.

It can also happen that the *p*–wall and *p*–gas events produce a signal in BEMC without creating tracks which point outside H1. In these cases the ToF situated just before BEMC, is used (see figure 2.2). The HERA machine has a clock which gives a time window where the interaction should occur. If the energy deposited in BEMC coincides with a signal of ToF outside of the interaction window the event is rejected.

2.4.1 The central jet chamber (CJC)

The CJC [55] consists of two concentric drift chambers: CJC1 with 30 cells of 24 sense wires each, and an inner (outer) radius of 203(452) mm and CJC2 with 60 cells of 32 sense wires each, and an inner(outer) radius of 530(844) mm. Both have an active length of 2200 mm, cover the polar angle from 15^o to 165^o and have a resolution of 0.170 mm in the radial–azimuthal plane and 22 mm along z. They are immersed in an homogeneous magnetic field of 1.15 T and achieve a transverse momentum resolution of $\delta p_T/p_T < 0.01 \cdot p_T/\mathrm{GeV}$.

The ep interaction region at H1 is of the order of few hundred μm in the xy–plane and very stable over several runs[1], allowing the measurement of the position of the interaction vertex in this plane using high momentum tracks from a few hundred events. Given a known xy position of the vertex, its z coordinate is determined on an event by event basis from all tracks fitting to the xy–coordinates of the vertex.

2.4.2 The time of flight detector (ToF)

The ToF consist of two walls made up of a sandwich of scintillator and lead, which are mounted perpendicular to the beam pipe. They are situated just behind BEMC at $z = -1.95$ m and $z = -2.25$ m respectively. The first plane has 16 counters of 317x317 mm^2, while the second consist of only 8 measuring 317x634 mm^2 each. The ToF detector has a 4 ns resolution [49].

Signals produced by p–wall, p–gas interactions behind BEMC arrive to the ToF before those produced by ep collisions around the IP (see figure 2.4). This allows the definition of time windows to discriminate between physics processes and background events due to beam–gas or beam–wall interactions. If the time signal from the ToF is 6 or more ns earlier than expected for signals originating in the IP, the event is rejected.

2.5 Detecting the lepton at small x

The next step is to find the lepton in BEMC. The main background for this signal comes from photo production where a π^0 mimics the lepton. To reduce this background, a track in the BPC, spatially matching the energy deposition found in BEMC, is required.

2.5.1 The backward proportional chamber (BPC)

The BPC is a four plane multiwire proportional chamber. Each plane has a wire orientation differing in 45^o from the one before. It is attached to the front surface of BEMC and its active zone covers from 135 mm to 650 mm in the radial coordinate and the polar angle ranges from 155^o to 174.5^o. It has a spatial resolution of about 1.5 mm in the transverse plane.

---

[1] A run is a set of events sequentially registered under the same experimental conditions of H1

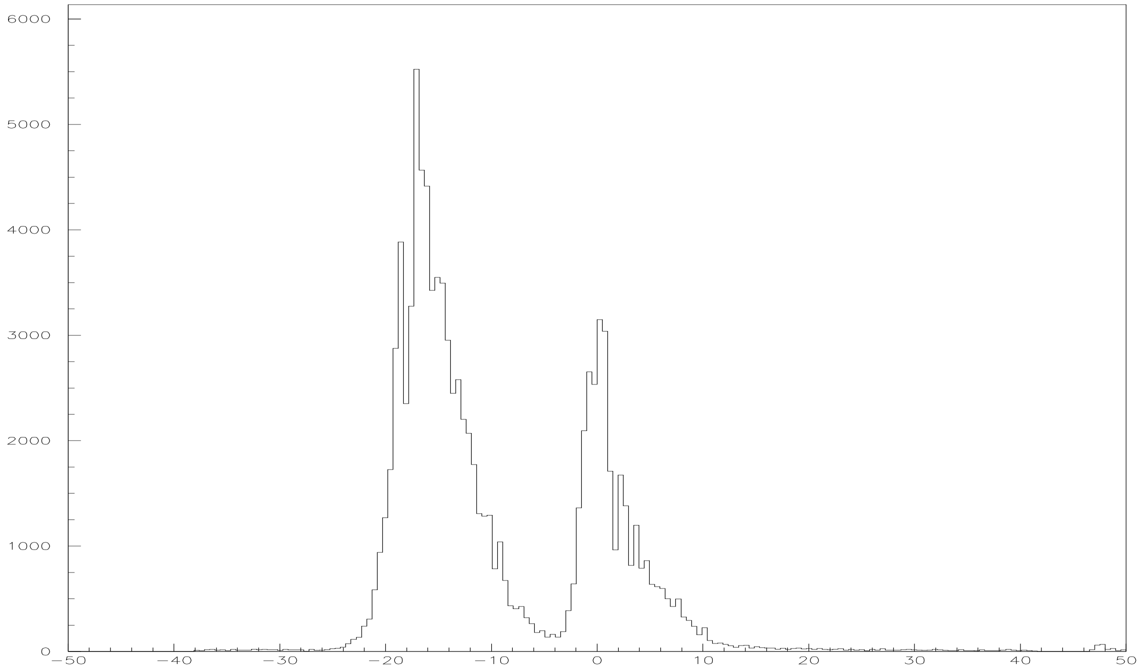

Figure 2.4: Time signals from the ToF system. Example of the time difference between signal in ToF produced by background or physics processes. The ordinate shows the time variable in ns, where the origin is defined for the expected arrival time of signals from the IP. The two clearly visible peaks originate from beam–gas or beam–wall interactions (peak to the left) or physics interactions (seen around zero). The scale of the abscissa is arbitrary. Figure from ref. [56].

2.5.2 The backward electromagnetic calorimeter (BEMC)

The BEMC [57] is a sandwich type lead–scintillator electromagnetic calorimeter consisting of 88 modules, with a wavelength shifter (WLS) optical readout (see figure 2.5). Its front end is placed at $z = -144$ cm, has a length of 34.3 cm, an inner radius of 10.8 cm and a diameter of 162.1 cm. It covers polar angles from 151^o to 176^o and has a 7 mm spatial resolution of the lateral shower position [57].

It has a depth of 21.7 radiation lengths, corresponding to about one hadronic interaction length and a resolution function given by [57]:

$$\frac{\sigma}{E} = \frac{0.039(2)}{E} \oplus \frac{0.100(3)}{\sqrt{E}} \oplus 0.017(5) \tag{2.1}$$

where E is given in GeV and leakage, sampling fluctuations and the readout by photo diodes and preamplifiers contribute to the resolution terms proportional to E, $\sqrt{E}$ and E^0 respectively. The absolute energy scale has been calibrated to a 1% using the kinematic peak – dominated by systematics – and has been globally cross checked using QED

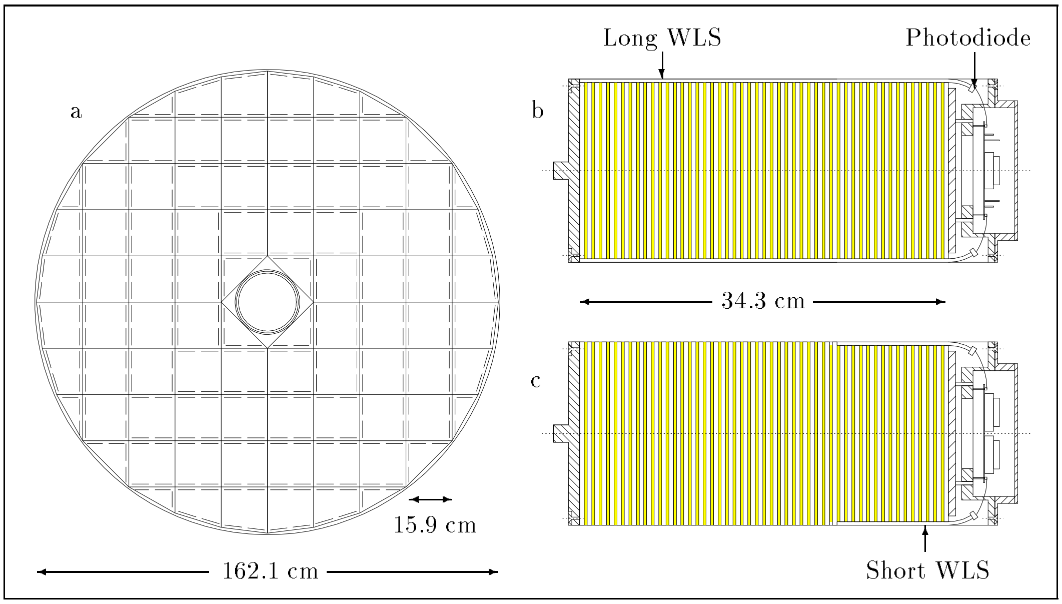

Figure 2.5: The BEMC readout scheme. There are two types of wavelength shifters (WLS) in the readout of BEMC: long and short. For every module there are four independent long WLS each connected to a photodiode (the outer triangular stacks have only three WLS). Their positions are shown in diagrams (a) and (b). For all square modules and for the big trapezoid stacks the last 15 sampling layers are read via short WLS as shown in diagram (c). Figure from ref. [57].

Compton events. The angular dependence of the calibration has been studied comparing the lepton energy to that calculated with the help of the double angle method [57].

The lepton candidates are defined via BEMC clusters [58]: the module with the highest energy is merged (clustered) with all the direct neighbors which present a signal, so there are maximal 9 BEMC modules contributing to one BEMC cluster. Requiring coincidences of three out of the four planes of the BPC and a spatially matching BEMC cluster allows to select with a great efficiency the scattered lepton (see section 3.3 for the precise cuts used in this analysis and 4.2.1 for their efficiencies).

2.6 Detecting the forward jet

The last part of the signature is a jet at high pseudorapidity. This jet consists of the particles produced through hadronization of the partons ejected out of the proton due to the interaction and it is measured in the liquid argon calorimeter of H1.

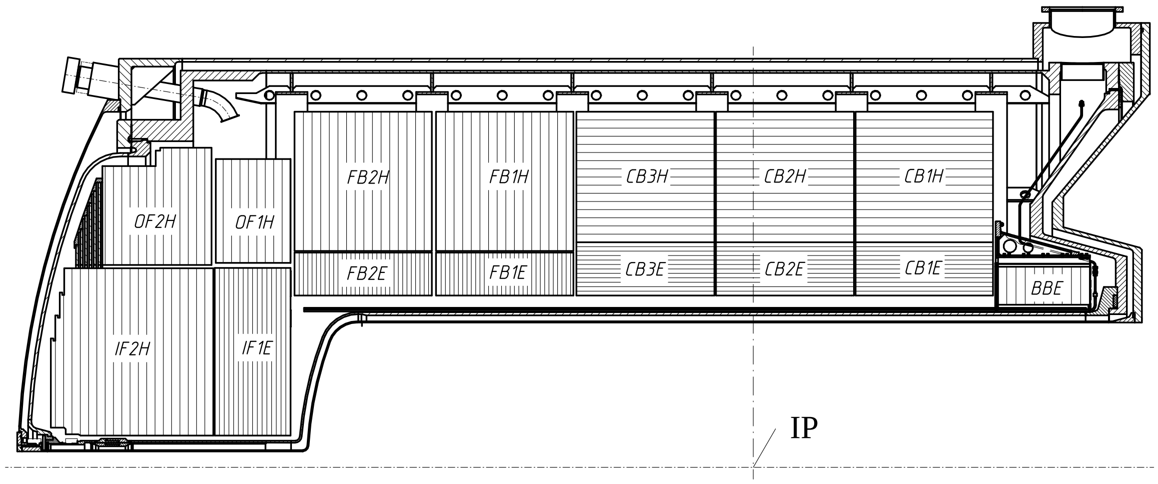

Figure 2.6: Transversal view of the LAr calorimeter. The letters H and E at the end of the labels in the figure refer, respectively, to the hadronic and electromagnetic parts of the calorimeter. The orientation of the absorber plates is indicated by the horizontal and vertical lines respectively. Figure from ref. [59].

2.6.1 The liquid argon (LAr) calorimeter

The LAr calorimeter [59] consist of eight rings of eight modules each, having an electromagnetic section with lead absorbers and a hadronic part made of stainless steel (see figure 2.6).

It is contained in a cryostat of stainless steel kept at a stable temperature of 90.2±0.1 K. It covers a polar angle from 3^o to 155^o, has a depth of 20–30 radiation lengths in the electromagnetic section and of 4.5–8 interaction lengths for the hadronic part (see figure 2.7).

A particle deposits its energy through showering producing a signal in several cells. The reconstruction of the deposited energy from this measured signal is done as follows (for further details see [60]). First a cut to suppress the influence of the electronic noise in the readout of the cells is applied. The cells are so calibrated that the mean value of the noise is zero in each cell. The standard deviation of the noise signal σ_{noise} varies from 15 MeV to 30 MeV as shown in figure 2.8. A given cell contributes to the measurement of the deposited energy if the absolute value of its signal is above the cut $f \cdot \sigma_{noise}$ where f is a factor which depends on the module of the LAr calorimeter according to table 2.2. The next step is to perform a topological noise cut. A cell will be used in the analysis only if its signal is smaller than $-4 \cdot \sigma_{noise}$ or if its signal or the signal of a direct neighbor cell is bigger than $4 \cdot \sigma_{noise}$. Note that this cut is not symmetric, and prefers cells with positive signals. Once the cells which will contribute to the measurement are thus selected they are merged into clusters. The clustering algorithm is fine tuned for electromagnetic showers [61], so a weighting algorithm is needed to obtain the energy of hadronic showers [62, 63]. It has been found that the description of jets in the forward region is better

Wheel	BB	CB	FB	OF	IF
f	2	2	2.5	3	3

Table 2.2: Noise suppression factors of the LAr calorimeter. The positions of the wheels can be read from the first two letters in the labels of figure 2.6.

using cells instead of clusters as input for the jet algorithm (see appendix A and reference [64]), so in this analysis the latter will be used, except to define the SQ_CUT (see section 3.4 and 4.3.4) which uses clusters in the central region of the LAr calorimeter.

The energy resolutions measured in test beams are $12\%/\sqrt{E}\oplus 1\%$ and $50\%/\sqrt{E}\oplus 2\%$ for clusters in the electromagnetic and hadronic sections respectively. The absolute energy scale for hadrons is known with a 4% uncertainty from studies of transverse momenta balance between the scattered lepton and the hadronic final state (see section 4.3.6 and reference [95]).

2.7 The H1 luminosity system

The measurement of luminosity in H1 is based on the Bethe–Heitler process $ep \to ep\gamma$ (see figure 2.9) which has a clear experimental signature, a very high cross section and the possibility to calculate it analytically, allowing thus the extraction and monitoring of the luminosity from the rate of events detected (for a detailed description of this method along with other methods used as a cross check see [65]).

The system consist of two arms (*cf.* figure 2.9):

- The electron tagger (ET) is situated at $z = -33.4$ m, it is built out of 49 KRS-15 crystals and has a polar angle acceptance from 0 to 5 mrad.

Figure 2.7: Depth of the LAr calorimeter. Lines of constant interaction lengths λ and radiation lengths X_0 in the LAr calorimeter along a cut in the azimuthal midplane of an octant. Figure from ref. [59].

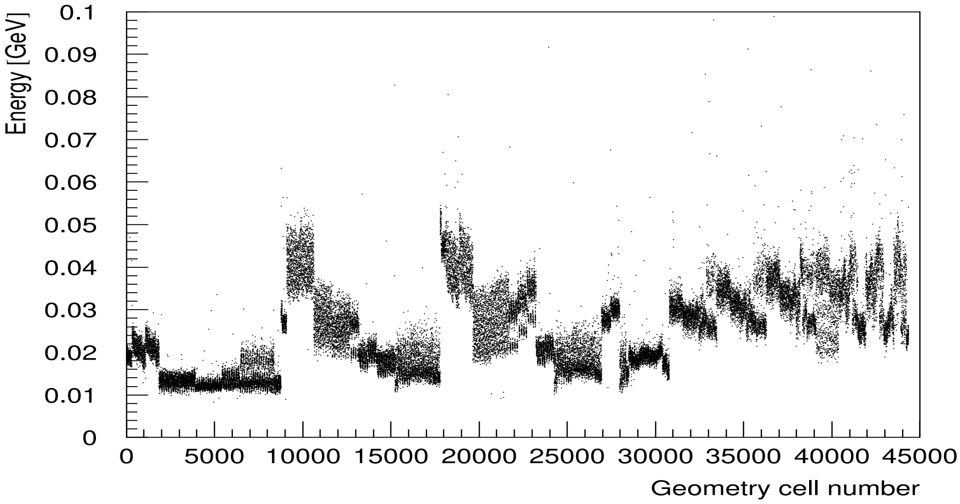

Figure 2.8: RMS of noise in the cells of the LAr calorimeter. The geometry cell number refers to the internal numeration scheme of the cells in the LAr calorimeter. The structures seen correspond to the different cell capacities of the calorimeter.

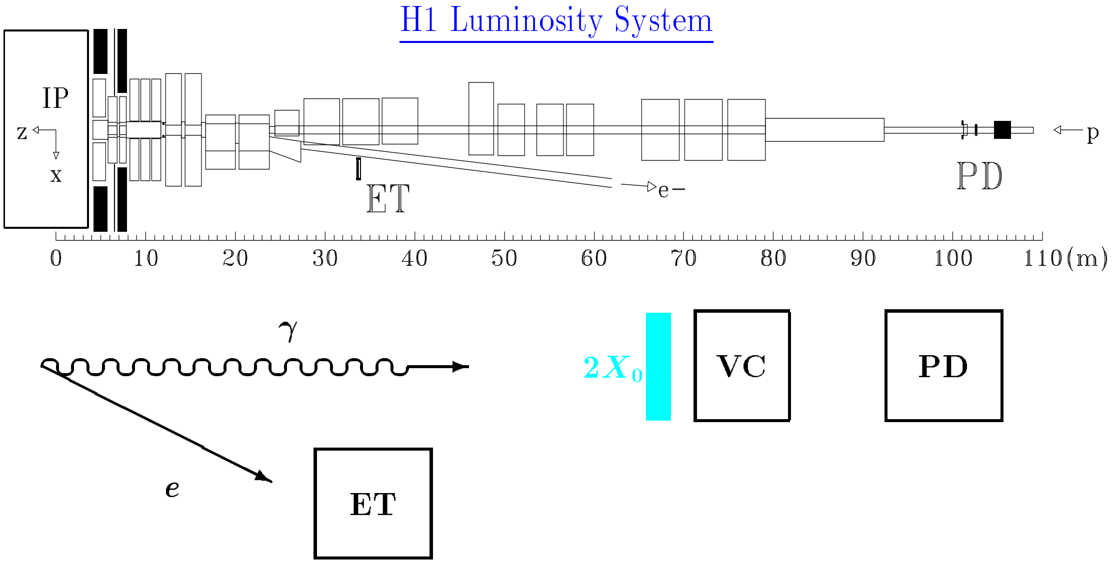

Figure 2.9: The luminosity system of H1. In the upper part of the diagram the position of the two arms of the luminosity system are marked with the labels ET and PD for the electron and photon arm respectively. In the lower part of the diagram the electron and photon produced by a Bethe–Heitler process $ep \rightarrow ep\gamma$ are shown along with the subdetectors which are used to measure their energy.

- The photon detector (PD) is at $z = -102.9$ m, is built out of 25 KRS-15 crystals of 22 radiation lengths and covers the polar angles between 0 and 0.45 mrad. It is protected from the high synchrotron radiation flux by a filter of two radiation lengths made of lead and a water Čerenkov veto counter (VC) with a depth of one radiation length.

A Bethe–Heitler process is tagged when in both arms a signal is detected with a total energy from ET, PD and VC equal to that of the incoming lepton. During 1994 the total systematic error in the determination of the luminosity was 2.0% for the runs with electrons and 1.4% for the runs with positrons [66].

Chapter 3

Selection of data

At this point, the motivation to study forward jets and the H1 detector to measure them have been presented. In this chapter both of them, theoretical and experimental input, will be brought together to define the selection of data on which the studies presented in this work are based. A pictorial representation of this union is shown in figure 3.1. The scattered lepton, the struck quark along with some QCD radiation, the forward jet and the remnants of the proton after the interaction sketched (counterclockwise) in the diagram are clearly seen in the longitudinal view of the H1 detector. Also shown are the incoming lepton (e) and proton (p) together with the trajectories of the particles created during the interaction.

As it was done in the previous chapter first the trigger will be discussed, then how to cut away the p–gas, p–wall background. Afterwards, once the sample consists of ep events, the selection of the scattered lepton and the forward jet will be presented, emphasizing the background for each individual signal and the cuts applied to reduce it. So the selection is driven on the one hand by the theoretical requirements and on the other hand by the constrains imposed by the detector itself via its geometry or via its ability to distinguish between the forward jet events and other sources of physics which may mimic the signature looked for. The efficiency of this selection will be discussed in the next chapter.

3.1 Triggering on a NC DIS event

The first step in the selection procedure is to determine which events will be written on tape to be available for further analysis. The subdetectors of H1 have a two branch read out. One of them is relatively slow, but carries all the information from the experiment, the other is coarser, but very fast and is used for the first trigger level (a complete review of the H1 trigger system with special emphasis on triggering of NC DIS events can be found in [67]). This analysis used a trigger composed from a logical AND of the following elements:

!TOF_BG: No veto from ToF to ensure the collision happened during the interaction window and avoid p–gas, p–wall background (see chapter 2.4.2 and figure 2.4).

!BSET_EQ1IN: In BEMC the stacks near the beam pipe (the inner triangular stacks seen in figure 2.5.a) are prone to collect background, so they were disabled as

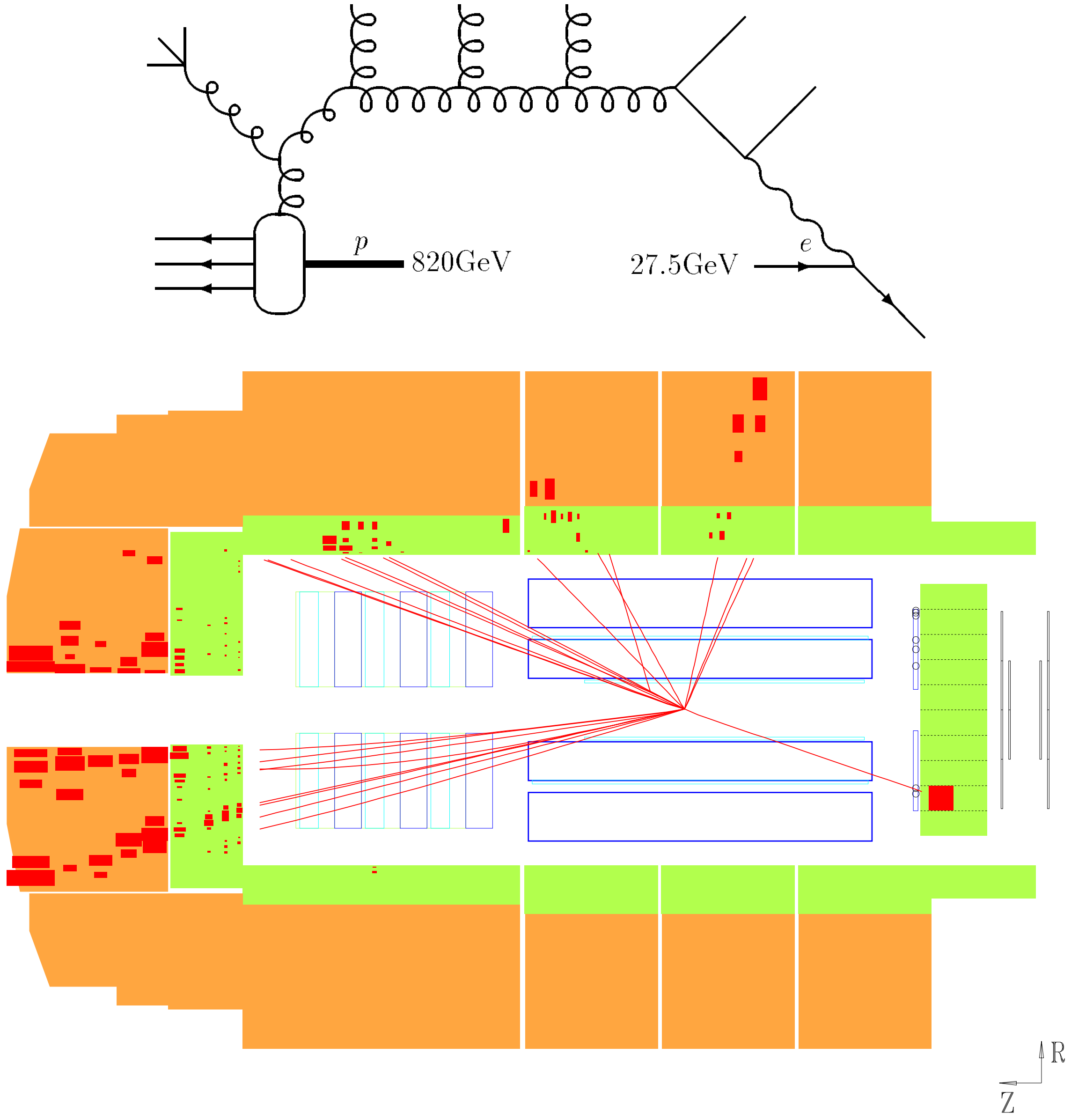

Figure 3.1: Forward jets in theory and praxis. A diagram representation of a forward jet event, along with the response of the H1 detector in a longitudinal view. In counterclockwise direction starting from the right side of the diagram are: the scattered lepton, the struck quark jet, some QCD radiation, the forward jet and the remnant of the proton. In the longitudinal view of the H1 detector the forward jet is seen in the lower hemisphere.

trigger initiators. This effect is of no importance here due to the angular cuts applied to the scattered lepton (see the definition of the TH_E cut in section 3.3).

!BSET_SDE: One source of false triggers was the sensitivity of the photo diodes in the read out of BEMC (see figure 2.5) to synchrotron radiation. It can happen that photons from synchrotron radiation hit one of the photodiodes of a particular stack causing a trigger to be produced. Therefore triggers due to the signal of only one photo diode in the stack were disabled. This was done for the largest polar angles (inner triangular modules of the BEMC in figure 2.5.a) in level one of the trigger and for all other modules of the BEMC in level 4.

BSET_CL2: A cluster of at least 7.5 GeV (measured by the trigger branch see ref. [67]) was required.

During 1994 the rate of this trigger varied between 5 and 12 Hz, and except for some short luminosity periods which were excluded from this analysis, was not prescaled; i.e. all triggered events were written to tape and were available for detailed analysis. The efficiency of this trigger will be determined in section 4.2.1.

3.2 Selecting a NC DIS event

Once the events are on tape the next steps of the selection occur off–line. In this section the Z_VTX and E-P_Z cuts, which are designed to reject background events originated by p–gas, p–wall interactions, will be discussed.

In HERA the proton bunches have a RMS of 11 cm in the z direction, producing ep collisions not only at the IP but in a region around it. During the 1994 data taking period the mean of the z coordinate of the vertex (z_{vtx}) was displaced by about +4 to +5 cm from the IP, which is reflected in a cut of about 3σ being applied to the data (see figure 3.2):

Z_VTX: The event is accepted if

$$-25\text{cm} < z_{vtx} < 35\text{cm} \tag{3.1}$$

Another cut applied at this stage was

E-P_Z: The event is accepted if

$$35\text{GeV} < E - p_z < 80\text{GeV} \tag{3.2}$$

where

$$E - p_z = \sum_i E_i - p_{z_i}$$

and i runs over all particles of the event.

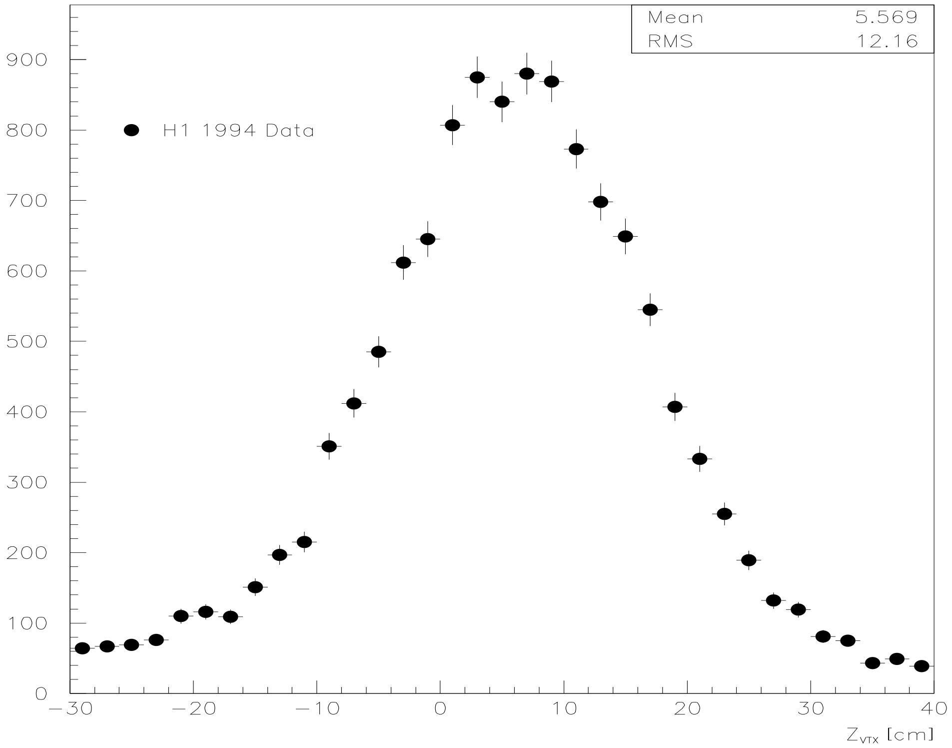

Figure 3.2: Distribution of the z coordinate of the interaction vertex for the region considered in this analysis.

Due to four–momentum conservation at the interaction vertex, this quantity (for events without an initial radiated photon) should be equal to two times the incoming lepton energy, which in 1994 was $k_0 = 27.5$ GeV. On the other hand for p–gas, p–wall it is expected that $E - p_z$ tends to zero. So this cut rejects p–gas, p–wall events which were not thrown away by ToF system.

3.3 Selecting the lepton at small x

The main background to an electron or positron in BEMC comes from events at very low Q^2 – called γp or photoproduction events due to the quasi real status of the intermediate boson – where part of the hadronic final state deposits its energy in BEMC and mimics the lepton signal [69].

To compare the behavior of the γp and DIS events under the applied cuts, a γp sample was selected and used in the plots of this section. As it only serves as an illustration the requirements applied to select events to the γp sample were only to have an energy deposition in the electron tagger detector (signature of a photoproduction process) and no signal in the photon arm (to avoid Bethe–Heitler events) of the luminosity system, along with a cluster in BEMC (so that they can fake DIS events).

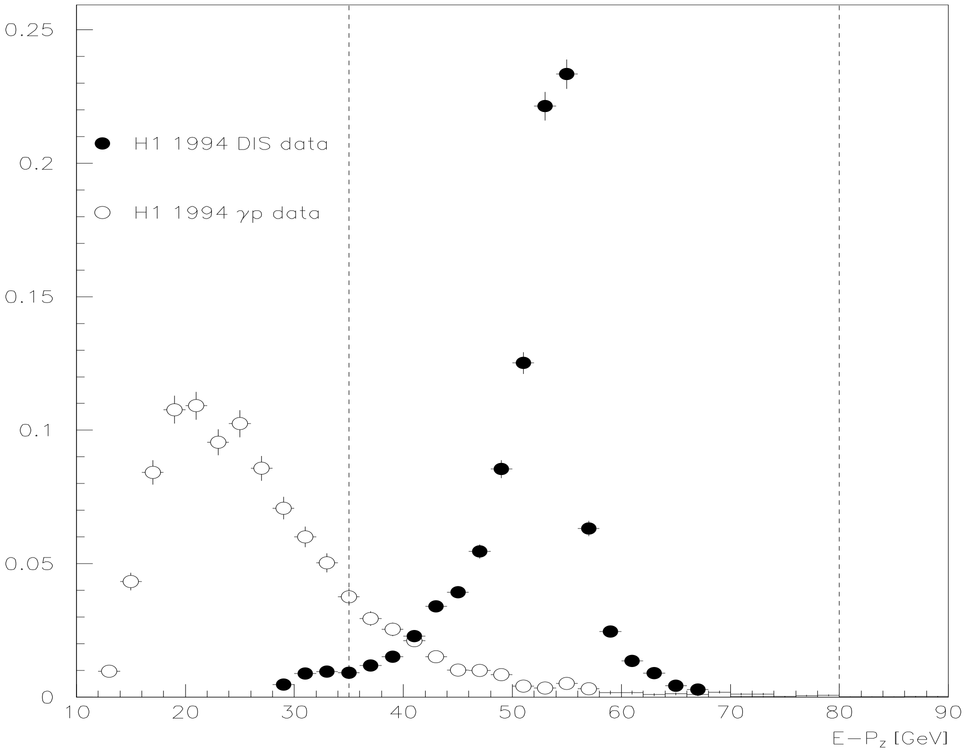

Figure 3.3: The distribution of the $E - P_Z$ variable for events of the γp (empty bullets) and DIS (full bullets) samples is shown along with the cuts used in this analysis (dotted lines). The error bars reflect the statistics used.

It is worthwhile to mention that in γp events the lepton is scattered at very small angles (*cf.* equation 1.2) and often escapes detection in H1 allowing the use of the E-P_Z cut to suppress photoproduction background (see figure 3.3) which is further reduced through one kinematic (E_E) and two topological cuts (CLU_R and D_BEMC_BPC) to be discussed in this section. Also the TH_E and X_CUT requirements along with their motivation will be presented. The efficiency of these cuts and their effect in the suppression of photoproduction background will be discussed in the next chapter.

It is a known fact that deposition of energy in a calorimeter produce showers which have a bigger lateral profile for hadrons than for electrons or positrons [70]. Note that for BEMC the Molière radius is 3.5 cm [1]. Taking advantage of it a "radius" is defined and used to reject those events with a hadronic origin (see figure 3.4).

CLU_R: The event is accepted if

$$r < 4\text{cm} \tag{3.3}$$

where

$$r = \frac{1}{E}\sum_i E_i\sqrt{(x_i - x_c)^2 + (y_i - y_c)^2},$$

---

[1] The Molière radius gives an estimation of the lateral shower size. See for example [70]

the sum runs over all modules – with coordinates x_i, y_i at the center of the module – in BEMC which contribute energy to the lepton candidate and

$$x_c = \frac{1}{E}\sum_i E_i x_i, \qquad y_c = \frac{1}{E}\sum_i E_i y_i, \qquad E = \sum_i E_i.$$

In H1 the point in BEMC given by (x_c, y_c) is projected to the BPC plane and the distance D_BEMC_BPC between it and the nearest track in the BPC is calculated. Most of the background from γp events comes from neutral particles, a π^0 for example, so they don't always leave a signal in the BPC, as the charged scattered lepton does. Furthermore, when it does the distribution of the variable D_BEMC_BPC is quite different for both cases (see figure 3.5):

D_BEMC_BPC: The event is accepted if

$$\text{D\_BEMC\_BPC} < 4\text{cm}. \tag{3.4}$$

The following two cuts ensure a good energy and polar angle measurement of the lepton.

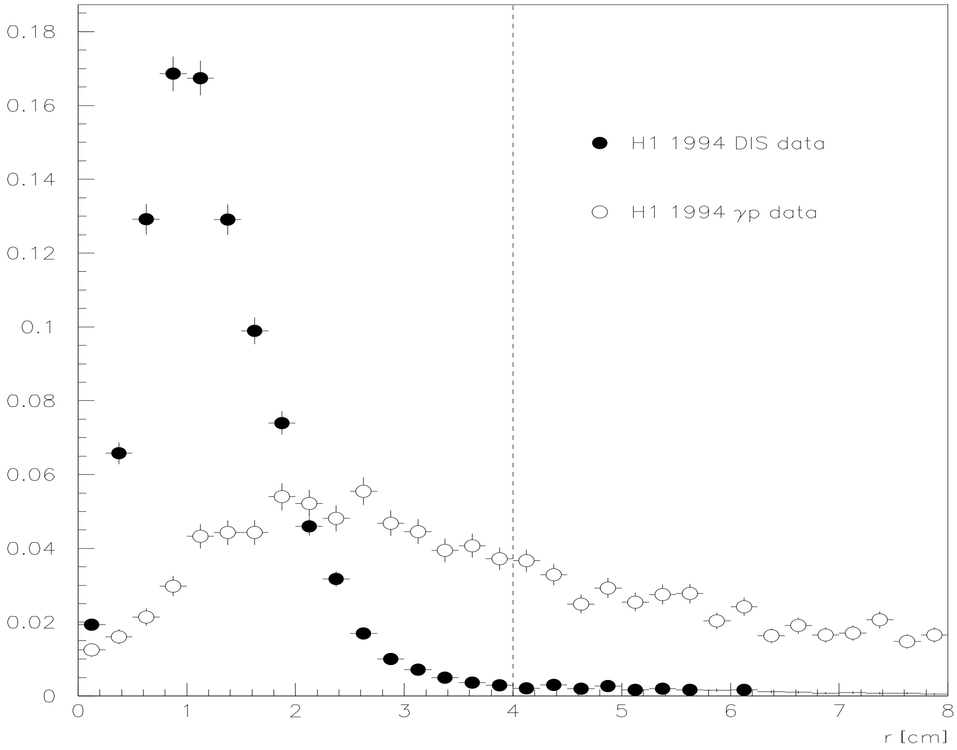

Figure 3.4: The distribution of the r variable (see 3.3) for events of the γp (empty bullets) and DIS (full bullets) samples is shown along with the cuts used in this analysis (dotted line). The error bars reflect the statistics used.

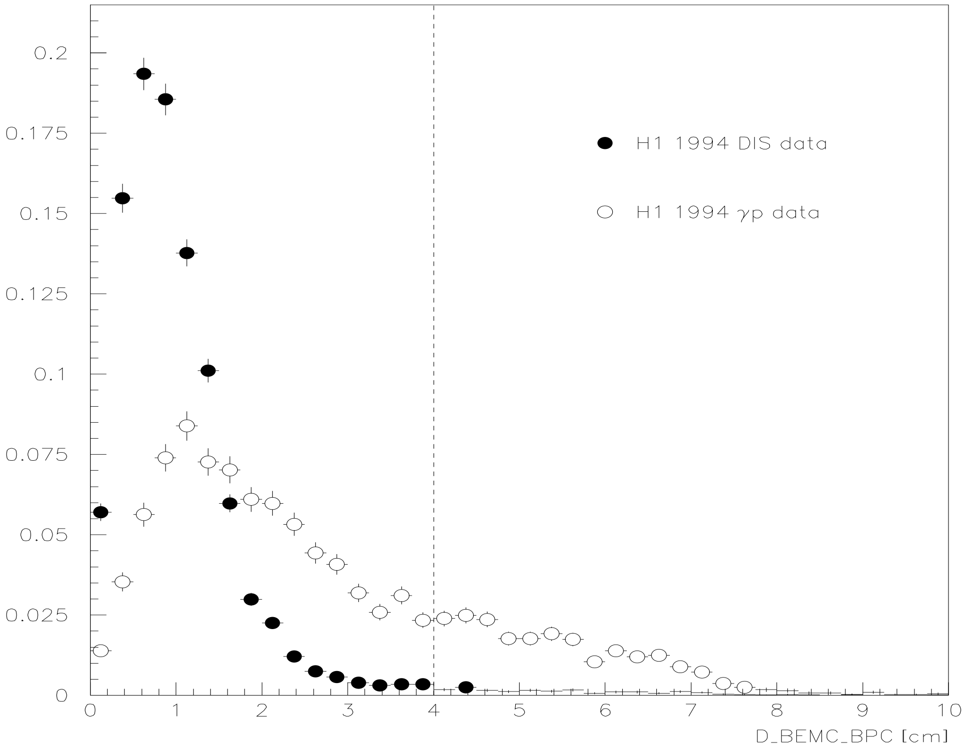

Figure 3.5: The distribution of the D_BEMC_BPC variable for events of the γp (empty bullets) and DIS (full bullets) samples is shown along with the cuts used in this analysis (dotted line). The error bars reflect the statistics used.

E_E: The event is accepted if

$$E_e > 11\text{GeV} \tag{3.5}$$

where E_e is the energy of the lepton candidate. Note that due to the proton boost of the HERA system the hadrons from γp interactions which go to BEMC and may fake the DIS lepton are constrained by kinematics to have small energies (see figure 3.6), so this cut serves to suppress photoproduction background, to obtain a good energy measurement and to measure well above of the trigger threshold of 7.5 GeV (see the trigger efficiency in figure 4.1).

TH_E: The event is accepted if

$$160^o < \theta_e < 173^o \tag{3.6}$$

where θ_e is the polar angle of the lepton candidate. This cut restrict the sample to be within the acceptance region of both, BEMC and BPC. Due to the PT2_Q2 cut (see section 3.4) it is not possible to extend the measurement to higher polar angles.

X_CUT: Using the electron method (*cf.* eq. 1.4) the event is accepted if

$$0.0001 < x < 0.004 \tag{3.7}$$

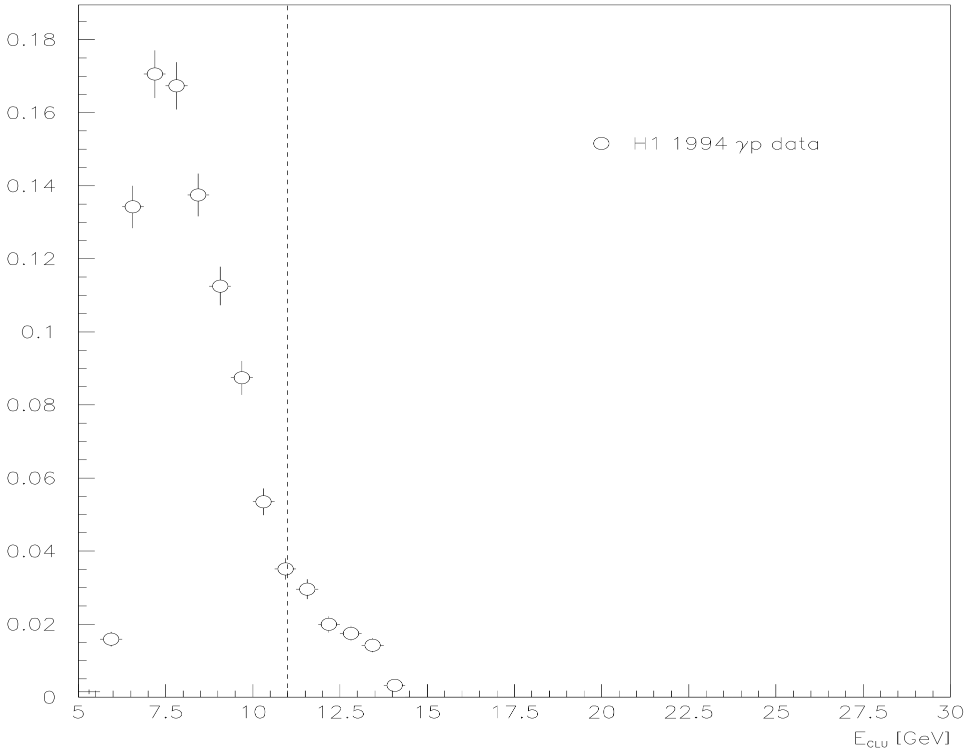

Figure 3.6: Energy distribution of the cluster in BEMC with the highest energy for the γp sample.

The upper cut is because the region of interest for this analysis is low x, also for x bigger than 0.004 there were very few events. The constrains imposed by the PT2_Q2 cut (see next section) define the lower end of the cut on x.

3.4 Selecting the forward jet

The necessity to measure jets arise from the confinement properties of QCD, which doesn't allow free partons to be detected, forcing a hadronization process between the hard interaction and the actual measurement. A review of hadronization models can be found in [71].

There are different ways to define a jet (see for example [72, 73]), each one adapted to the particular needs of the analysis where they are applied. The algorithm used here is a slight modification of the cone prescription used in H1 [74] (see appendix B). The cone algorithm was used with a value $R_j = 1$ for its radius. The main difference with respect to the standard cone jet algorithm of H1 is how the four momentum of the jet is obtained from its components. In this analysis the covariant convention was used, i.e.

$$p_{\mu_j} = \sum p_{\mu_i}$$

where i runs over all cells forming a jet.

As already mentioned in section 1.4.3 the jet to be selected should not be produced by the struck quark. To avoid it two cuts are introduced, Y_MIN and SQ_CUT. In the naive quark–parton model, where QCD radiation is neglected, there is a relation between the polar angle of the struck quark and the kinematic variable y (see figure 3.7) making it possible to cut away events where the struck quark goes forward.

Y_MIN: Using the electron method (*cf.* eq. 1.3) the event is accepted if

$$y > 0.1 \tag{3.8}$$

Unfortunately, it can happen that the incoming lepton radiates a photon pushing thus the measured y to a higher value than the real one (*cf.* equation 1.3 and figure 3.8). This may unable the Y_MIN cut to reject events where the forward jet originates indeed from the struck quark. To avoid this situation the SQ_CUT cut was implemented. It is based on the observation that (see figure 3.1) when there is a struck quark jet in addition to the forward jet, there is deposition of energy in the LAr calorimeter which does not originate from the forward jet (the struck quark jet and radiation between it and the forward jet). Vice versa if only the struck quark jet exists and it goes forward only the forward jet should be found in the LAr calorimeter and nothing else.

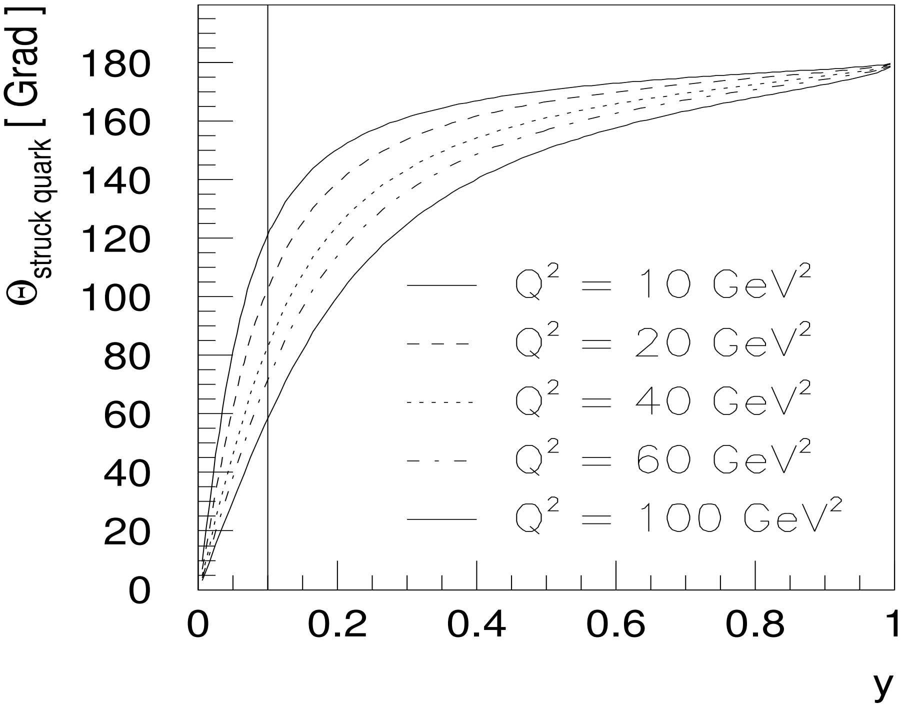

Figure 3.7: The Y_MIN cut. Dependence on y and Q^2 of the polar angle of the struck quark in the naive quark–parton model. Note that above y=0.1 the struck quark produces a jet in the central part of the LAr calorimeter.

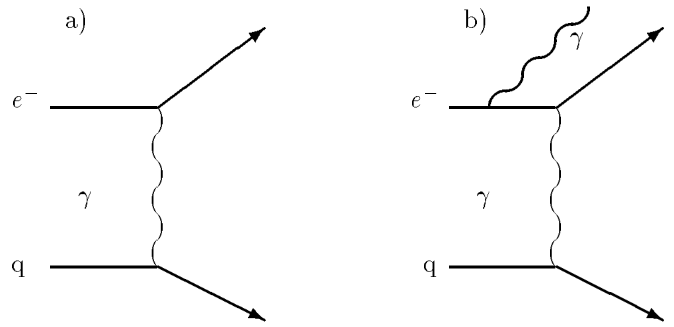

Figure 3.8: Diagrams with (right) and without (left) QED initial state radiation.

SQ_CUT: The event is accepted if there exist a cluster with an energy bigger than 0.5 GeV and pseudorapidity η_c in the range

$$\eta_j - 1.5R_j > \eta_c > -1.31 \tag{3.9}$$

where η_j is the forward jet pseudorapidity and $\eta = -1.31$ corresponds to a polar angle of $\theta = 150^o$, i.e. in the BBE module of the LAr calorimeter (*cf.* figure 2.2). Clusters built out of noise cells in this polar region have normally one cell (around 70 % of them), sometimes 2 cells (25 %) and seldom 3 cells (less than 4 %), while for a very few cases clusters consisting of 4 cells were found, and none consisting of 5 or more cells were found (500 events investigated). Taking into account that the RMS of the noise for each cell is around 30 MeV or less (see figure 2.8), it can be concluded that the requirement of a cluster with an energy bigger than 0.5 GeV is safely above the noise.

The last set of cuts to be discussed are those related with the kinematics of the forward jet and the acceptance of H1.

E_J: The event is accepted if

$$E_j > 28.7\text{GeV}, \tag{3.10}$$

using the approximation $x_j = E_j/p_0$ where $p_0 = 820\text{GeV}$ is the energy of the incoming proton, the equation (3.10) is equivalent to $x_j > 0.035$. This cut reflects the requirement of Mueller's proposal (see section 1.4.3) asking for x_j as large as experimentally possible.

Signal	**Background**	**Cuts**
ep event	p–gas, p–wall	E-P_Z, Z_VTX
Lepton	γp	CLU_R, D_BEMC_BPC
Jet	Struck quark	Y_MIN, SQ_CUT

Table 3.1: Cuts against background.

TH_J: The event is accepted if

$$7^o < \theta_j < 20^o. \tag{3.11}$$

Above 20^o there are very few events surviving all the cuts. The cut at 7^o is to ensure full containment of the jet in the LAr calorimeter of the H1 detector (see section 4.3.2).

PT2_Q2: Using the electron method to measure Q^2 (*cf.* eq. 1.2) the event is accepted if

$$0.5 < p_{T_j}^2/Q^2 < 2.0. \tag{3.12}$$

This is the key cut of the analysis and mirrors the requirement to have the transverse momentum at the end of the ladder of the same order than at the beginning as proposed by Mueller (see section 1.4.3).

PT_J: The event is accepted if

$$p_{T_j} > 3.5\mathrm{GeV}. \tag{3.13}$$

This cut is driven on the one hand by the necessity to extend the phase space for the PT2_Q2 cut, and on the other hand by the impossibility to resolve jets with lower transverse momentum due to uncertainties in hadronization.

3.5 Overview of the selection of data

The selection presented in this chapter could be divided in those cuts motivated to suppress the background and those motivated by the searched signal. They are summarized in tables 3.1 and 3.2 respectively.

For the 2.78 pb^{-1} of luminosity that were used in this analysis the number of events which were triggered and survived all cuts was 1945. Its distribution in the allowed phase space is shown in figure 3.9. Note that the limit for small x is given by the PT2_Q2 cut due to the lower limit in the PT_J cut and the kinematic constraint in x due to the size of Q^2 present at HERA and clearly seen in the figure. So the options to extend the kinematic range covered experimentally are to go to lower transverse momentum of the jet (quite difficult), to shorten the interval allowed in the PT2_Q2 cut (needs a big increase in statistics) and lower the limit of the E_E cut. This last improvement will be possible due to the inclusion of a new backward calorimeter – the so called SPACAL

Signal	**Physics**	**Cuts**
Lepton	small x	E_E, TH_E, X_CUT
Jet	high η_j	E_J, TH_J, PT_J
Both	BFKL	PT2_Q2

Table 3.2: Physics motivated cuts.

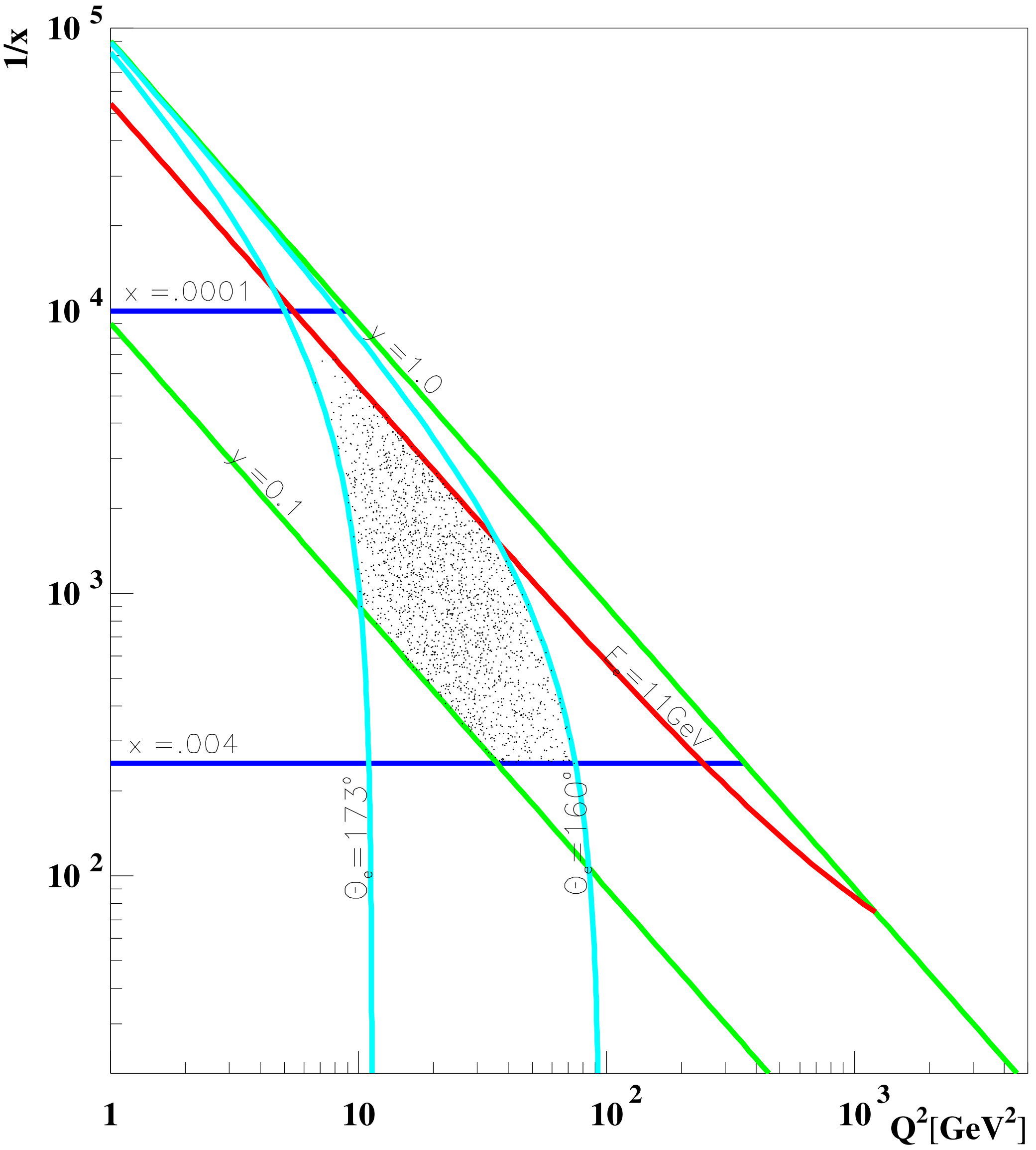

Figure 3.9: Distribution of the selected events in the (x,Q^2) kinematic plane. The depletion seen for low x and low Q^2 is due to the PT2_Q2 cut.

calorimeter [75] – in the H1 experiment which took place between the data taking periods of 1994 and 1995. Unfortunately as seen in figure 3.9 this improvement will only help in filling out the region currently measured but it will not increase the low x reach, which will still be defined by the PT2_Q2 cut.

Chapter 4

Treatment of data

The selection procedure presented in the previous chapter was motivated by Mueller's proposal, but its elements – the leptons and jets – are observed only indirectly through the signals they produce on the different subdetectors, rising the question of how many of the selected events and how much of the signals on them were created indeed by the lepton and jet looked for, and how much comes from other sources. So a detailed study of the correspondence of what it is called a lepton and a real lepton is obligatory (the same applies to jets). It is also necessary to subtract the events (or at least its contribution to the measurement) which did not originate from the desired interaction, but managed to survive the selection. These studies are done in part using only the detector, profiting from the redundancy in measurement that it offers, and in part using MCs.

In general after the selection is completed, studies are made to determine its efficiency and purity in the case of the lepton, and, in the case of jets to develop a correction function to account for detector effects. Afterwards the remaining background is statistically subtracted and the observables are corrected, which means that the calculated lepton efficiencies and correction factors associated to the jet are taken into account. These steps are discussed in the next sections.

4.1 MC generators used

There are computer programs called Monte Carlo generators (MC) which produce events according to the equations governing a given process. These equations are based on a given approximation or model and refer (at least for the cases treated here) to the interactions of the lepton with partons. Due to the confinement property of QCD, the partonic final state must be subject to a hadronization prescription to produce a final state of particles. So the output of MC generators is in two levels: the partonic and the hadronic level.

This hadron level can be viewed as the prediction of the model on which the MC is based or can be fed into a program which simulates the components of H1 [76] and whose output undergoes exactly the same analysis chain as normal data [77], producing a third MC level: the detector level. As there is a complete knowledge of what was put in, the response of the detector to a given input can be evaluated.

Here a brief description of the MCs used for the analysis is presented. Further details can be obtained in the references given. An introduction to the MC method can be found in [78, 79].

4.1.1 MCs used to correct the data

In this section the programs used to correct the data from detector to particle level will be presented. This programs were used to substract the background (PYTHIA and DJANGO) and to estimate the effect of the acceptance and efficiencies of the H1 detector (DJANGO and LEPTO). Their main characteristics are summarized in table 4.1

PYTHIA As has been already pointed out the background to the lepton signal is created by γp events. PYTHIA [80] in combination with JETSET [80] generates, among other processes, photo production events for ep colliders. The cross section for γp is huge compared to that of DIS. That means, that millions of generated events are needed to have a MC sample with a luminosity equivalent to the luminosity of data, so that a statistically stable subtraction of the background can be performed.
To avoid the detector simulation of each one of them, which is the most time consuming task, only the signals in BEMC were simulated and in case that they posed a possible danger as a background for DIS events, the complete response of the detector was totally simulated, otherwise the event was dropped. As the simulation of BEMC consumes only a small fraction of the total computer time needed to simulate a complete event, this so called turbo–simulation allowed to use MC events to subtract the remaining photo production background from the selected sample. In total 1783313 events were generated and only 12851 were simulated.The versions used for this analysis were PYTHIA 5.7 and JETSET 7.4.

DJANGO The physics background to the forward jet signal is produced by QED initial state radiation as explained in section 3.4. The DJANGO [82] program is composed of HERACLES [81], LEPTO [39] and JETSET. HERACLES contains the complete QED radiative corrections, LEPTO was used in the color dipole model (CDM) mode [33] (see section 4.1.2) and JETSET provided the hadronization via the string fragmentation model.
Also here a preselection scheme for the generator was developed to shorten the computer time needed to simulate the detector response. Events at hadron level with a lepton fulfilling $E_e > 8$ GeV, $159^o < \theta_e < 174^o$ and $y_e > 0.05$, where y_e is the kinematic y variable calculated without taking into account possible QED radiation, and a jet with $E_J > 12$ GeV, $p_T > 2$ GeV and $3^o < \theta_J < 30^o$ were selected and simulated. The efficiency of this preselection was calculated to be $98.3 \pm 0.77\%$ by simulating a sample of 0.6 pb^{-1} (80000 events) without preselection: the number of events which survived the detector cuts was 295, and from those 5 would have not survived the preselection cuts. The error is statistical.
The small losses due to the preselection scheme are to be compared to the factor of at least five won in the time needed to simulate the preselected

MC Program	SB	CAE	Version
PYTHIA	γp	—	PYTHIA 5.7, JETSET 7.4
DJANGO	QED–ISR	YES	HERACLES 4.4, ARIADNE 4.05
LEPTO	—	Cross Check	LEPTO–MEPS 6.5

Table 4.1: MC used to correct the data. The initials stand for: Subtracted Bakcground, Correction of Acceptances and Efficiencies, Initial State Radiation.

events instead of simulating the whole sample. These events were used to estimate the influence of QED radiation and to correct the measured cross section to hadron level. This sample is labeled DJ6+CDM. The versions used were: HERACLES 4.4, ARIADNE 4.05 (CDM model), JETSET 7.4. It is important to mention that although ARIADNE version was 4.05, it has been used as version 4.03[1], because then the best agreement between data and MC in detector level was obtained. The GRV parton density functions [24] have been used. They are computed in next to leading log and using the DIS regularization scheme.

LEPTO (see section 4.1.2). LEPTO has been used in the MEPS mode. The version 6.5 of the program was used with the GRV parton density functions and the values of its parameters were obtained from a fit to HERA data [84]. This MC was only used to obtain an estimation of the uncertainty in the hadronic energy scale (see section 4.3.6) and to estimate the systematic uncertainty on the correction function due to different models (see section 4.4).

4.1.2 MCs used to compare to the measured cross sections

In this section the MC programs used to obtain the expectation of different models to compare them to the measured data will be presented. Two of them (LEPTO–MEPS and HERWIG) are based in QCD matrix elements to order α_s complemented by parton showers according to the DGLAP prescription and the other one (LEPTO–CDM) uses the color dipole model complemented with the matrix element for boson–gluon fusion. Both LEPTO programs use the string model of hadronization, whereas HERWIG uses the clustering model. A summary of these models is given in table 4.2.

LEPTO This generator offers two modes: the matrix elements plus parton showers mode (MEPS) and the color dipole model mode (CDM, but also referred in the literature as ARIADNE).

In MEPS the ep process is generated using matrix elements to order α_s for the hard interaction and complemented with a prescription to develop parton showers based on the leading log DGLAP equations. The hadronization is

---

[1] For compatibility with older versions and to facilitate cross checks the ARIADNE MC has a switch that allows the user to select the version to be used to generate the events

	LEPTO–MEPS	LEPTO–CDM	HERWIG
QCD Model	MEPS + SOT	CDM + BGF	MEPS + CO
Hadronization	String Model	String Model	Clustering Model
PDF	MRSH	MRSH	MRSH
Parameters	Default	Default	Default
Version	6.5	4.08	5.8

Table 4.2: MC used to compare to data. The initials stand for: Strong Ordering of Transverse momenta along the ladder, Boson–Gluon Fusion matrix element, COherence effects along the ladder, Parton Density Function.

carried out using the Lund string model. From version 6.3 onwards it has in addition two non perturbative mechanisms: If a sea quark took part in the hard process, its partner builds a string with a quark from the proton remnant (in older versions it would have been part of a meson or a baryon in the remnant); the second mechanism allows to rearrange the color flow between the generated partons after the matrix elements and parton showering has been calculated, but before the hadronization has taken place. The version used here is LEPTO–MEPS 6.5 with the MRSH [85] parameterization of the parton densities. This parameterization was obtained in next to leading order and using the DIS scheme for regularization.

The second mode, LEPTO–CDM, is based on the emission of gluons forming a chain of independent radiating color dipoles and is complemented with the matrix element for boson–gluon fusion from LEPTO–MEPS. It also uses the Lund string model to perform the hadronization. The dipole emission does not show an ordering on the square of the transverse momenta of the gluons. This motivated the CDM model to be considered a kind of effective BFKL model. Nevertheless it has recently been put forward [86] that the actual difference between LEPTO–MEPS and LEPTO–CDM has a different origin. When in CDM the remnant is one of the two objects forming the dipole and a QCD Compton event is being generated, a factor $(\mu/p_T)^\alpha$ is introduced to take into account the remnant size (emissions of small wavelengths from an extended antenna are suppressed). Here μ is the inverse size of the remnant (the default value for this parameter is 0.6 GeV), p_T is the scale of the emission and α is a parameter of the program whose default value is 1.0. It should be noted that the predictions of the LEPTO-CDM model are quite dependent on this parameter varying about $\mp$ 25–30% for α values of 1.5 and 0.5 respectively. A first fit of the LEPTO-CDM MC to HERA data [84] suggest a value of 1.5 for alpha, which would mean about a 25–30% reduction of the MC cross sections presented here. The version used is LEPTO–CDM 4.08 with the parton densities given by the MRSH parameterization.

HERWIG This generator [83], like LEPTO–MEPS, is also based in a matrix element approach complemented by the emission of parton showers through the leading log DGLAP equations. It has two main differences with respect to LEPTO–MEPS: one is that the implementation of the parton showers takes into account coherence effects among the emitted partons and second it uses a clustering model for hadronization. The version used here is HERWIG 5.8 with the parton densities given by the MRSH parameterization.

Two comments about the following questions: why different CDM versions for correcting and comparing to data? why different parton densities? From the simulated versions of CDM that were available, the best description of the measured data was obtained using the version 4.03 (incidentally that is the reason why version 4.05 was set to behave like version 4.03) making it optimal to correct the data. Unfortunately there were some bugs in the code and the author produced quite recently a new version. Currently the newest one is 4.08 and it is the version to use to obtain the predictions of the model.

With respect to the parton densities there is a similar problem. The GRV parton densities give the best description of the F_2 data. Unfortunately LEPTO calculates the total cross section using the partons densities, and in the GRV case this means that the charm contribution is not present (GRV generate charm dynamically) and the prediction of the model can not be properly normalized to be compared with data. So the MRSH distributions, which also offer a good description of the inclusive data, especially in the kinematic domain considered here, were used.

4.2 Lepton studies

To this point the lepton has been defined through a series of requirements to be fulfilled (see section 3.3 and tables 3.1 and 3.2), now it is the time to check that the selection makes sense, i.e., that what it has been selected has indeed a leptonic origin and that it is possible to extract reliably its four momentum. The following subsections are devoted to clarify these issues.

4.2.1 Efficiencies of the lepton selection

For the angular domain selected in this analysis, the efficiency of the BSET_CL2 trigger depends only on the lepton energy. It is about 0.1 for 5 GeV and rises sharply to 0.95 about 8 GeV to reach a perfect efficiency for clusters with 11 GeV or more (see figure 4.1). To check that for this analysis the efficiency of the trigger is 1.0, the selection presented in last chapter was applied to all events triggered independently of the BSET_CL2 trigger. All events that survived the preselection were also triggered by BSET_CL2 demonstrating that indeed its efficiency is 1.

To estimate the efficiency of the CLU_R, D_BEMC_BPC and the Z_VTX cuts the selection was slightly changed: first the minimal lepton energy required was set to 20

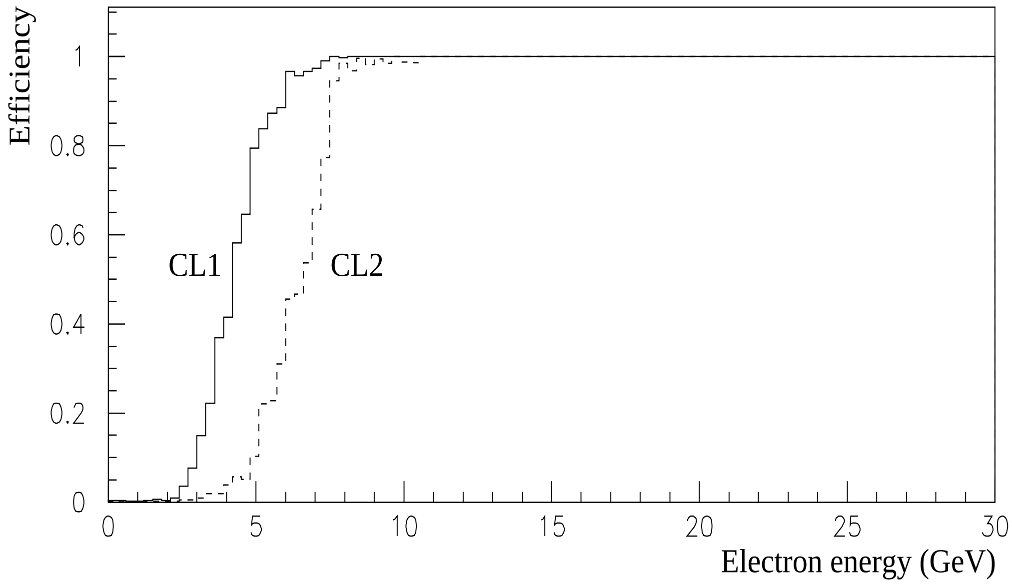

Figure 4.1: Efficiencies of the BSET_CL2 trigger. The dotted line shows the efficiency of the BSET_CL2 trigger as a function of the energy of the scattered electron. Also shown is the response for another threshold (solid line labeled CL1) which was used to monitor the performance of the BEMC. Figure from ref. [57].

GeV to be sure the sample does not contain photo production background (see figure 3.6) and second the PT2_Q2 cut was not imposed to increase the statistics of the sample. The efficiencies were then defined as the ratio of the number of events selected applying all cuts inclusive the cut under study to the number of events selected without applying the cut under study. This program was performed for H1 data and for the simulated DJ6+CDM sample. The results are shown in table 4.3 and figure 4.2. They show agreement between data and MC. They are also very close to unity.

4.2.2 Reconstruction of leptonic variables

To obtain the lepton four momentum via the electron method presented in section 1.2, it is necessary to measure the energy of the scattered lepton along with its polar and azimuthal angles. These angles are measured via the BPC and the reconstructed vertex. Unfortunately during the 1994 run period the z axis of the proton and lepton beams were

	Z_VTX	**CLU_R**	**D_BEMC_BPC**
H1	98±2	99±2	98±2
MC	99±1	99±1	99±1

Table 4.3: Efficiencies for the Z_VTX, CLU_R and D_BEMC_BPC cuts, given in %, for H1 data and the DJ6+CDM MC.

not the same (a run dependent tilt of about 0.45 mrad, see for example figure 4.3) and second the alignment of CJC and BPC was tilted 1.5 mrad. So to reconstruct correctly the measured angles of the scattered lepton the effect of these two problems had to be taken into account

Another effect to account for was that the reconstructed BPC point was shifted with respect to the BEMC cluster position 0.15 cm in x and 0.25 cm in y [87]. Finally, it has to be corrected for the influence of the H1 magnetic field on the azimuthal angle of the leptons.

The first three plots on the left column of figure 4.4 show the distribution of different variables for events of the forward jet selection presented in chapter 3 along with the distributions obtained using the DJ6+CDM MC. Both the data and MC distributions are normalized to their total number of events. The good agreement between both shapes for every distribution, along with the MC description of the efficiencies shown in section 4.2.1 allows to use the DJ6+CDM MC to correct for detector effects in the measurement of the scattered lepton.

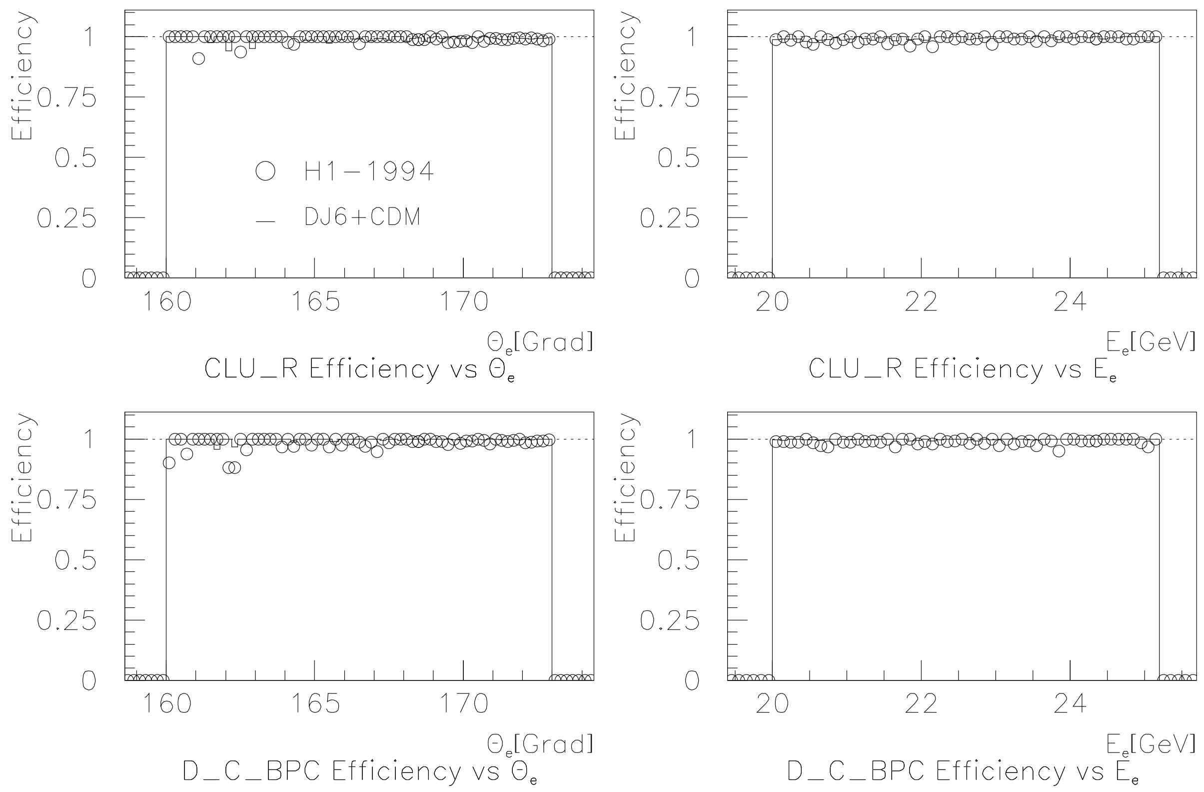

Figure 4.2: Efficiencies for the lepton selection. The efficiencies of the Z_VTX and CLU_R cuts and their dependence on the energy and polar angle of the scattered lepton are shown for H1 data from the present analysis (empty bullets) and compared to the DJ6+CDM MC simulation (solid histogram). The dotted line represents a perfect efficiency.

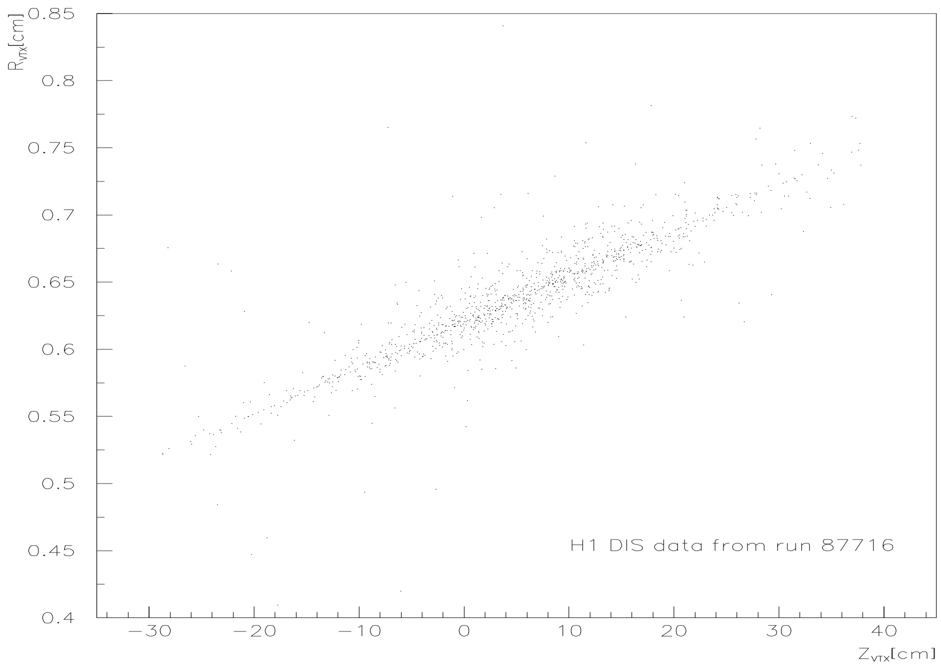

Figure 4.3: Example of the beam tilt. The z coordinate of the interaction vertex is plotted against the transversal distance of the vertex to the H1 z axis: $r_{VTX} = (x_{VTX}^2 + y_{VTX}^2)^{1/2}$.

4.2.3 Reconstruction of kinematics

As already pointed out, initial state QED radiation has the effect to shift the measured values of the kinematic variables with respect to their real value.

In figure 4.5 the DJ6+CDM MC, which includes initial state QED radiation, shows the difference between the measured and generated value of the x and y kinematic variables for the events of the forward jet sample. The shadowed part of the histogram shows those events which according to the generator have radiated a hard initial state photon ($E_\gamma > 3$ GeV) and which produce tails in the distributions. These events are statistically subtracted from the data. The percentage of events to be subtracted and the shape of their distribution is obtained by normalizing the data and MC distributions of the variable under study to one and subtracting then from the data the amount of background estimated by the MC.

4.2.4 Systematic uncertainties from the lepton

The absolute energy scale of the lepton in the BEMC was determined to 1% using a fit to the kinematic peak and cross checked using the double angle method[57]. Thus in this analysis the energy of the measured lepton was varied ±1.0% and the induced change in the cross section (see table 4.7) was considered as a part of the systematic error.

The polar angular measurement has an uncertainty of 1 mrad [29], accordingly the variation of this parameter contributes to the systematic error (see table 4.7). As in

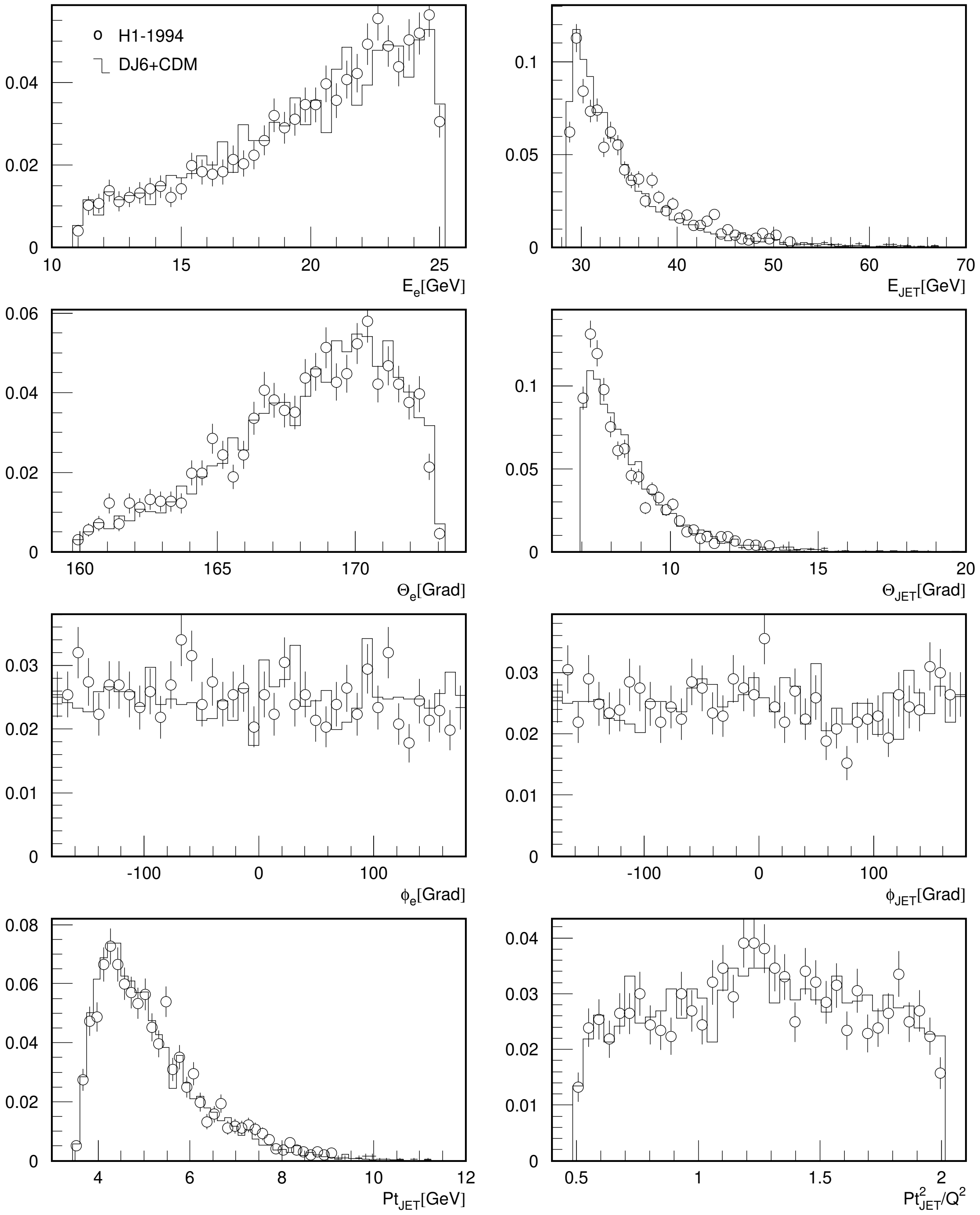

Figure 4.4: MC Description of measured variables. The first three plots of the left column show the leptonic variables whereas the other plots refer to the jet variables. The MC program DJ6+CDM was used and all the distributions are normalized to their total number of events.

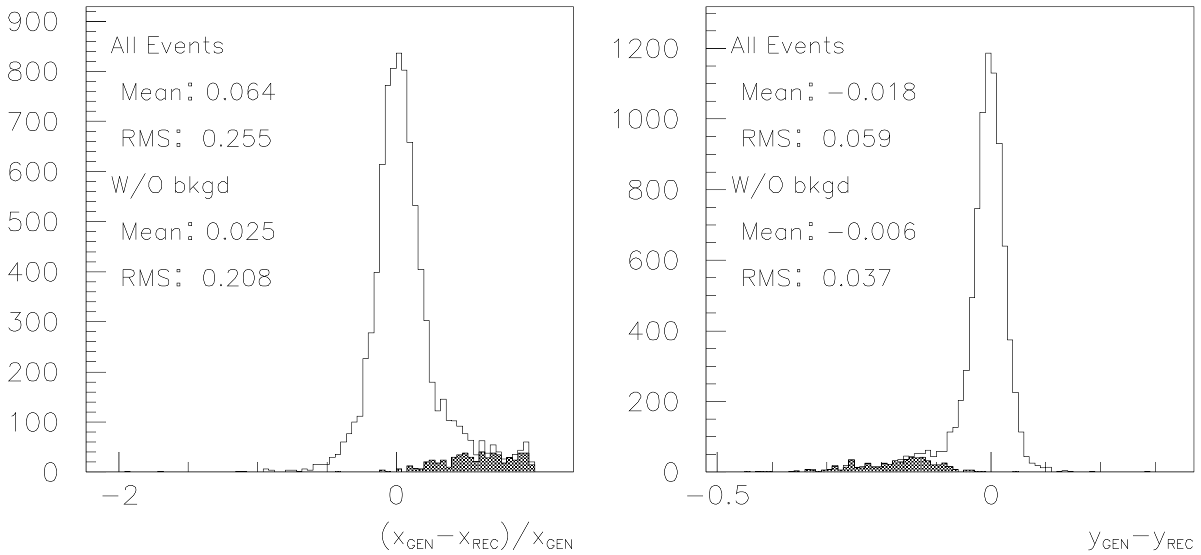

Figure 4.5: Reconstruction of the kinematic variables with the DJ6+CDM MC in the forward jet sample. The shadowed part of the histogram shows those events which according to the generator have radiated a hard initial state photon ($E_\gamma > 3$ GeV). These events are statistically subtracted from the data.

the selection procedure the azimuthal angle is not explicitly used, and the physics results which use this variable can not resolve the uncertainties in its measurement[2], no variation of it was considered for the systematic error.

4.2.5 Remaining background

As already mentioned photoproduction events were generated and simulated to estimate their contribution to the final sample, which turned out to be ~2.5% [3]. This is compatible with estimations using data:

Normal DIS events do not deposit energy in the electron tagger (see section 2.7), on the other hand a fraction of the γp events do. Also Bethe–Heitler events, which happen randomly in coincidence with other type of events originating at the IP, may cause a signal in the electron tagger, but fortunately they also produce a signal in the photon tagger and the total energy deposited by these events in the luminosity system is about that of the incoming electron beam, i.e., 27.5 GeV, making it possible to identify them.

---

[2] In this work only the difference $\Delta\phi$ of the azimuthal angle of the scattered lepton and the jet is studied (see section 5.2), and the resolution of the jet azimuthal angle is about 8 degrees (see section 4.3.5), so small variations (of the order of its resolution) in the lepton azimuthal angle have no influence on $\Delta\phi$.

[3] The luminosity of the photo production events was defined as the number of events generated divided by the cross section calculated by the MC program; and it was used to normalize the estimated background to the luminosity of the measured data.

In the final sample 1.3% of the events have a signal in the electron tagger; 0.6% present also a signal in the photon tagger, where the total energy deposited in both detectors is about that of the incoming energy of the lepton beam, so these events are product of a Bethe–Heitler process, which leaves only ~0.7% of events compatible with a photo production origin. Folding the electron tagger efficiency (36% [49]), a compatible result for the photoproduction background of about 2.0% is obtained. This background concentrates in low x and it is statistically subtracted from the data using the PHYTIA MC result.

The background coming from initial state QED radiation is, as mentioned in section 4.2.3, statistically subtracted from the sample using the DJ6+CDM MC program. In this case the amount of events subtracted is also compatible with estimations using data: Normal DIS events do not deposit energy in the photon tagger, on the other hand a fraction of the events with initial state QED radiation do. Here also the Bethe–Heitler events have to be tagged before estimating the background.

The photon tagger shows energy deposition in 4.5% of the cases, from them about 2.0% come from Bethe–Heitler events (electron tagger is ~30% efficient – see figure 4.7 in [88] – and photon tagger 100% [49] for this process) leaving about 2.5%. The acceptance of the photon tagger for initial state radiation is also in the order of 30% [89], so the total background amounts to about 8.0% to be compared to the MC prediction of 9.0%. Its contribution to the measurement is also statistically subtracted from the data.

4.3 Jet studies

The forwards jets have to be measured in a region near the end of the acceptance of the LAr calorimeter and also near to the proton remnant, so the main concern has been first to select the jet algorithm that is best adapted to measure in the forward region, and then to check that the influence of the losses due to the beam pipe are minimal, that the scattering of particles off the structure of the beam pipe were under control to allow a correct reconstruction of the jet four momentum and finally that the MC description of the measured variables were acceptable. These items will be discussed in the following subsections.

4.3.1 Use of different jet algorithms

The criteria used to define which algorithm is better than the others were, first the amount of events where a jet is found both at the detector and the hadron level. It can happen that in a given event a jet is found at one of the two levels, but not in the other. A perfect algorithm would find always in a given event for every jet at hadron level a jet at detector level and vice versa.

A second criteria was the matching of jets in both levels. If in a given event a jet is found at both the detector and the hadron level, then the difference of the jet variables between the two levels was constructed. For a perfect algorithm this difference would be

Acceptance	**Jet Radius**			
	1.0	0.9	0.8	0.7
$\theta_{min} = 3^o$	6^o	5^o	5^o	4^o
$\theta_{min} = 4^o$	7^o	6^o	6^o	5^o

Table 4.4: Minimal θ_{JET} to have full acceptance in the LAr calorimeter for different jet radius and two values θ_{min} for the acceptance of the LAr calorimeter.

zero (i.e., the energy of the jet at hadron level would be exactly as the energy measured at detector level, and the same for the production angles of the jet). Also the width of the distributions for the differences between levels was taken into account. The smaller this width is, the better. Narrow distributions mean that the influence of the smearing due to detector effects is small.

To address the question of the optimal jet algorithm to measure forward jets, several studies were made in collaboration with J. Kurzhöfer to compare the JADE algorithm [91] both in its original version and with the inclusion of pseudo particles to the CONE algorithm. The results showed the CONE algorithm to be better suited for this analysis (see section 5.3 of [90]). Later work with J. Spiekermann showed that the KT algorithm [92] is, albeit slightly worse, of comparable quality to the CONE algorithm (see appendix C). A detailed study of the behavior of different jet algorithms in the frame of photoproduction events found also that the CONE algorithm is the best adapted to measure at HERA [93].

4.3.2 Influence of the polar angular cuts on the CONE algorithm

The LAr calorimeter of H1 is not completely hermetic due to the beam pipe, being able to measure only those particles which have a polar angle of at least 3 to 4 degrees depending on the position of the interaction vertex. Monte Carlo studies were done using the DJ6+CDM MC to determine the lowest jet polar angle which have a complete acceptance in the LAr.

Jets were built from the hadronic level of generated events taking into account all produced particles, then it was looked for all the particles in the jet whose polar angle were smaller than 3^o respectively 4^o. These particles would be outside the acceptance of the LAr calorimeter and their contribution to the jet four momentum would be lost. Then the minimal polar jet angle was selected, where at most 10% of the particles had a polar angle smaller than 3^o respectively 4^o. The results for different jet radii and both acceptance polar angles are shown in table 4.4. In average the particles whose polar angle was smaller than θ_{min} carried less than 2% of the jet energy.

Another important observation to consider here is that the 3 hadrons in the jet with the highest energy carried on average 80% of the jet energy and also determined to a great extent the jet direction and transverse momentum. For jets in the H1 detector it was found that the 5 clusters with the highest energy carried 75% of the jet energy and likewise determined its direction and transverse momentum. The average number of hadrons and clusters in the forward jets were 9.3 and 17.8 respectively. These results together with table 4.4 explain why the small loses due to the limited acceptance of the LAr calorimeter in the forward region are negligible for the jet selection used in this analysis.

4.3.3 Influence of scattering off the beampipe structures

Besides the struck quark which takes part in the hard interaction in a DIS process, there are the other constituents of the incoming proton to take into account. They give rise to the so called remnant, which has a small transverse momentum, but carries a lot of energy. It could be that one of these particles interacts with some of the structures which form the beam pipe. For example the C4 collimator (see figure 4.6) where particles produced with a polar angle as low as 0.73^o (for collisions exactly at the IP) may scatter and deposit energy into the LAr calorimeter.

To know if particles from the remnant could create forward jets through scattering in beampipe structures, special MC events were simulated and reconstructed. These events were generated in a standard way with the DJ6+CDM MC and then only particles whose polar angle was below a parameter θ_{MAX} were retained for simulation and reconstruction. The cases where θ_{MAX} was 4, 3, 2, 1 and 0.5 degrees were studied. For each case 5000

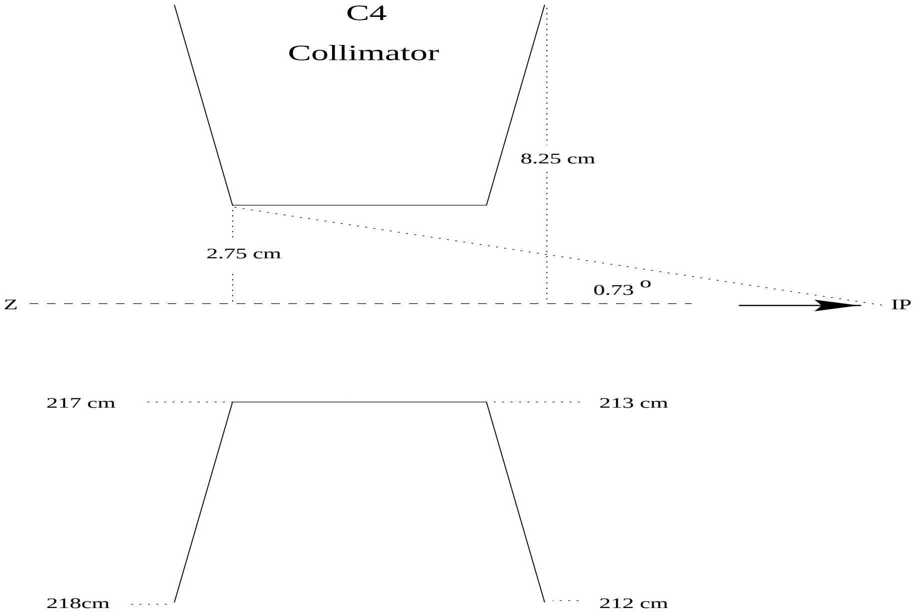

Figure 4.6: The C4 collimator. It is located a bit more than +2 meters away from the interaction point in the direction of the proton beam, and covers so small angles as $\sim 0.7^o$

events were studied and in none of them a jet in the forward direction ($7^o < \theta_j < 20^o$) with more than 3.5 GeV of transverse momentum was found. Note that if these events were fully reconstructed, about 20 events would survive the complete forward jet selection.

Furthermore the influence of particles emitted below 3 or 2 degrees on the measurement of the transversal energy flow from cells of the LAr calorimeter is on average slightly bigger than 0.2 GeV per unit in pseudorapidity between 7 and 20 degrees and shows a steeply falling behavior with increasing polar angle (see figure 4.7). The peak seen just above 20 degrees has its origins in the overlap of different wheels of the LAr calorimeter (see figure 2.6: about 20 degrees are where the modules IF1E, OF1H, FB2H and FB2E come together). Remember that the noise suppression scheme of the LAr calorimeter tends to select noise with positive energies as explained in section 2.6.1, so as more cells fall under the polar angular region around 20 degrees than in other angular domains, then the contribution from noise is bigger. That the noise cuts tend to retain positive noise energies is also the explanation why the transverse energy flow does not goes to zero for big polar angles –negative rapidities.).

Taking into account that the azimuthal angle has been integrated out, that the mean transverse momentum of the forward jets is around 5 GeV and that the description of the data by the DJ6+CDM MC is satisfactory (see figure 4.4) one can conclude that the

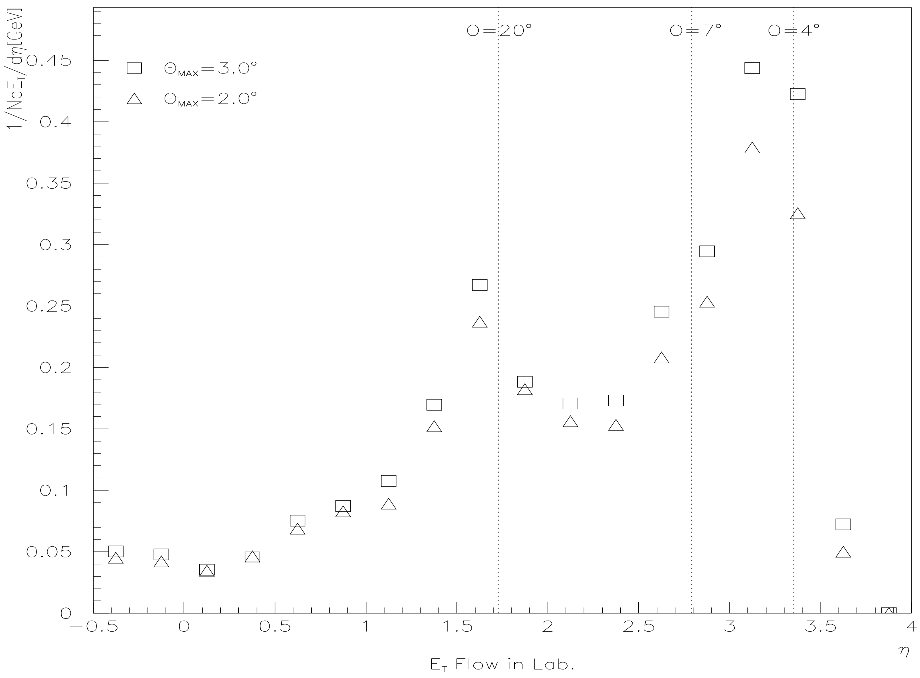

Figure 4.7: Transverse energy flow in H1 from "remnant" particles per unit in pseudorapidity for DJANGO events where only particles whose polar angle were less than θ_{MAX} were simulated and reconstructed

influence of scattering off beampipe structures in the forward jets is less than 2.5% (As ϕ has been integrated out, one unit of pseudorapidity is equivalent to the area of two jets. Taking as representative numbers 5 GeV in the total transverse momentum of the Jet and 0.25 from figure 4.7 one arrives to the quoted 2.5 %) and can be understood through the DJANGO MC.

4.3.4 The SQ_CUT

This cut was implemented to suppress events where the struck quark has a small polar angle and may mimic the signature of the forward jet. This happens mainly due to a wrong reconstruction of the kinematic variable y which renders the Y_MIN cut useless.

Figure 4.8 shows that indeed the SQ_CUT reject mainly those events with a very small y. As the Y_MIN cut has been applied all these events have a reconstructed y bigger than 0.1. The reason why the kinematic variable was so badly reconstructed is that in almost all these events a photon was radiated by the incoming electron. Then according to figure 3.7 these events have the struck quark jet in the forward region of H1.

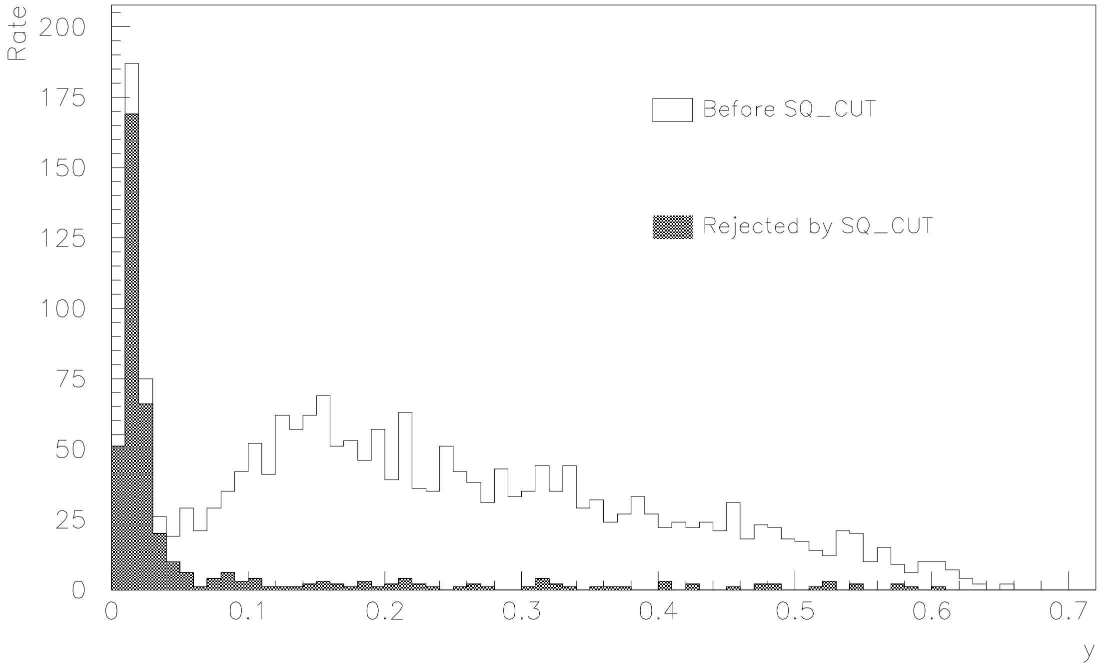

Figure 4.8: Distribution in the generated kinematic variable y of DJ6+CDM events for the forward jet sample before applying the SQ_CUT (all other cuts shown in tables 3.1 and 3.2 have been applied). The shadow histogram shows those events that were rejected by the SQ_CUT.

4.3.5 Reconstruction of jet variables

It has already been shown in figure 4.4 that the DJ6+CDM MC reproduce the shape of the distributions for the jet variables reasonable well. It also describes the jets profiles reasonable well: figure 4.9 shows, for different values of the minimal p_{T_j} allowed for the jet the η and ϕ jet profiles for a band in ϕ and η respectively, centered in the jet and two times the jet radius in width.

Another test to see if the selected jets behave as expected from jets is to study the dependence of the jet width in the transverse momentum of the jet [94]. If the ϕ jet profiles are parameterized according to

$$f(\Delta\Phi) = A \cdot \exp -(|\Delta\Phi|^{1/2} + b)^4 + b^4 + P \tag{4.1}$$

then the jet width Γ is given by

$$\Gamma = 2 \cdot ((\ln 2 + b^4)^{1/4} - b)^2 \tag{4.2}$$

where A, b and P are parameters to be fitted. The QCD expectation from [94] is that $\Gamma \propto 1/P_{T_j}$. To perform this test the forward jet sample was divided in 5 P_{T_j} intervals and for each intervals a jet profile was built and fitted with eq. 4.1. Then the corresponding value of Γ was calculated with eq. 4.2. The results are summarized in table 4.5

A fit of the form $\Gamma = 0.2 + 2.65 GeV/P_{T_j}$ to the values of columns two and four of table 4.5 is shown in figure 4.10, demonstrating the expected behavior of the width of the jet profiles with transverse momentum.

Figure 4.11 shows that the jets observed in the detector are strongly correlated in all four variables to the hadron level jets. The resolution in the reconstruction of the jet energy for the forward jet sample is around 20%, whereas for the transverse momentum and polar angle of the jet a value of around 16% is found. For the azimuthal angle the resolution is about 8 degrees which is quite bigger than the resolution on the azimuthal angle of the scattered lepton as mention in section 4.2.4.

P_{T_j} [GeV]	$< P_{T_j} >$ [GeV]	b	Γ
3.5–4.0	3.8	0.244±0.009	0.89±0.02
4.0–5.0	4.5	0.295±0.004	0.76±0.01
5.0–6.0	5.4	0.345±0.005	0.65±0.01
6.0–7.0	6.4	0.359±0.007	0.62±0.01
7.0–11.0	7.9	0.399±0.007	0.54±0.01

Table 4.5: Jet width for different P_{T_j}. The parameter b and the width Γ were obtained from eqs. 4.1 and 4.2 respectively.

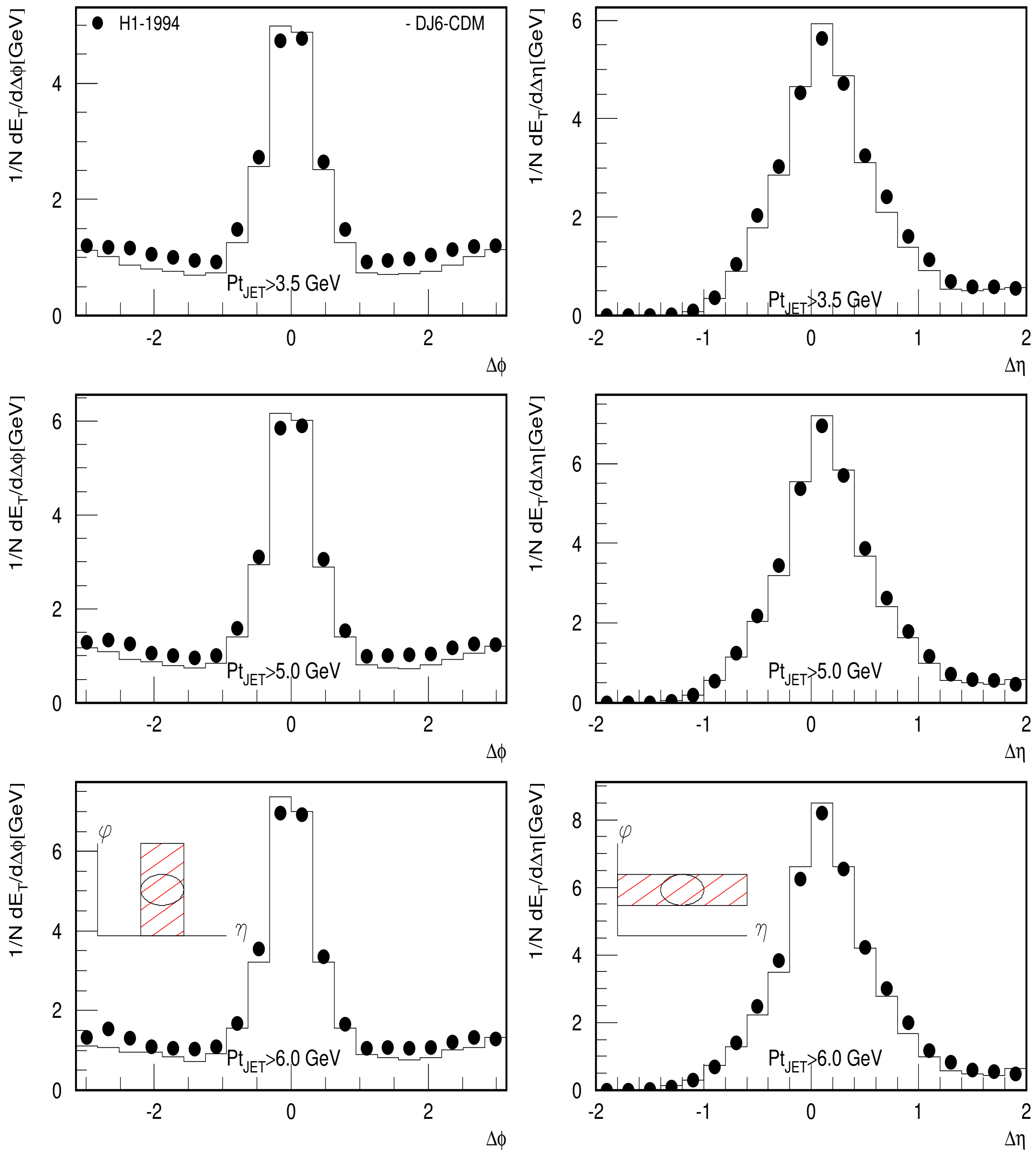

Figure 4.9: Jet profiles for different PT_J cuts. Transverse energy flow around the jet axis in pseudorapidity and the azimuthal angle, for different PT_J cuts and in a band of 2 times the jet radius. See the (η, ϕ) plane in the bottom plots where the circle represents the jet, and the shadow shows where are the cells which contribute to the jet profile. For every cell in the band the differences $\Delta\Phi = \phi_j - \phi_c$ and $\Delta\eta = \eta_j - \eta_c$ have been plotted. The subscripts j and c refer to the jet and the cell respectively.

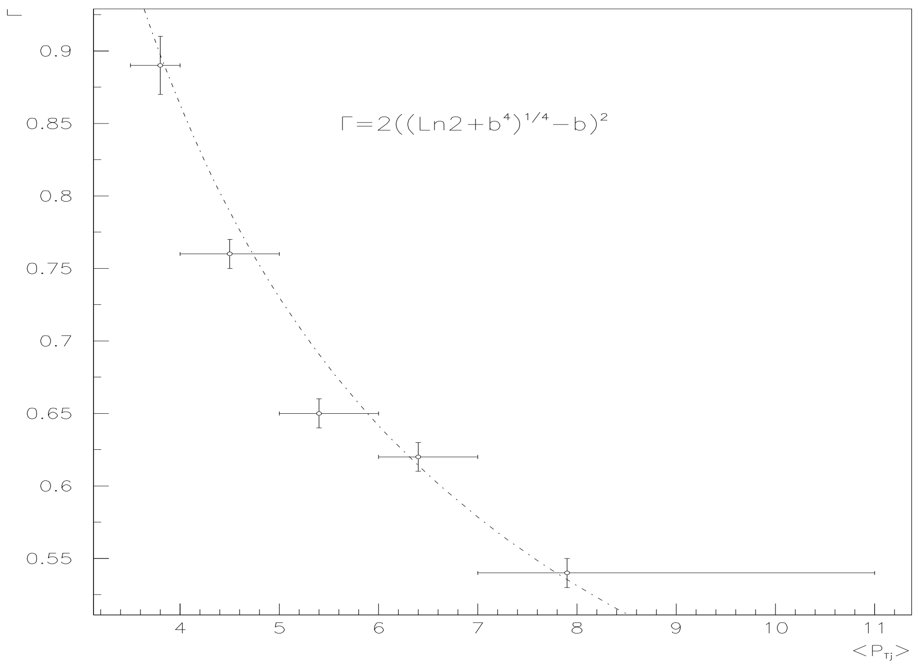

Figure 4.10: Jet widths for different P_{T_j}. The points show the width Γ of forward jets for different values of P_{T_j} (in GeV) along with a fit of the form $\Gamma = 0.2 + 2.65 GeV/P_{T_j}$.

4.3.6 Hadronic energy scale

The hadronic energy scale of the LAr calorimeter is determined from the balance between the transverse momentum of the scattered lepton and the transverse momentum of the hadronic final state. This balance, normally calculated as P_T^h/P_T^e is compared to the prediction of MC models and the differences found are taken as an estimation of the uncertainties on the scale of the measurement of hadronic energy. Several studies using different data samples have been made producing a possible variation of the energy scale of up to 4% (for a summary see [95]).

Here two samples were studied. The forward jet sample and a DIS sample obtained from the application of the cuts presented in chapter 3 except those cuts referring to

	DIS sample		**Forward Jet sample**	
	MEAN	RMS	MEAN	RMS
DATA	0.82±0.01	0.37±0.01	0.95±0.02	0.42±0.02
LEPTO–MEPS	0.83±0.01	0.36±0.02	0.94±0.03	0.42±0.04
DJ6+CDM	0.81±0.01	0.40±0.02	0.96±0.01	0.37±0.02

Table 4.6: Comparison of P_T^h/P_T^e among data and MCs.

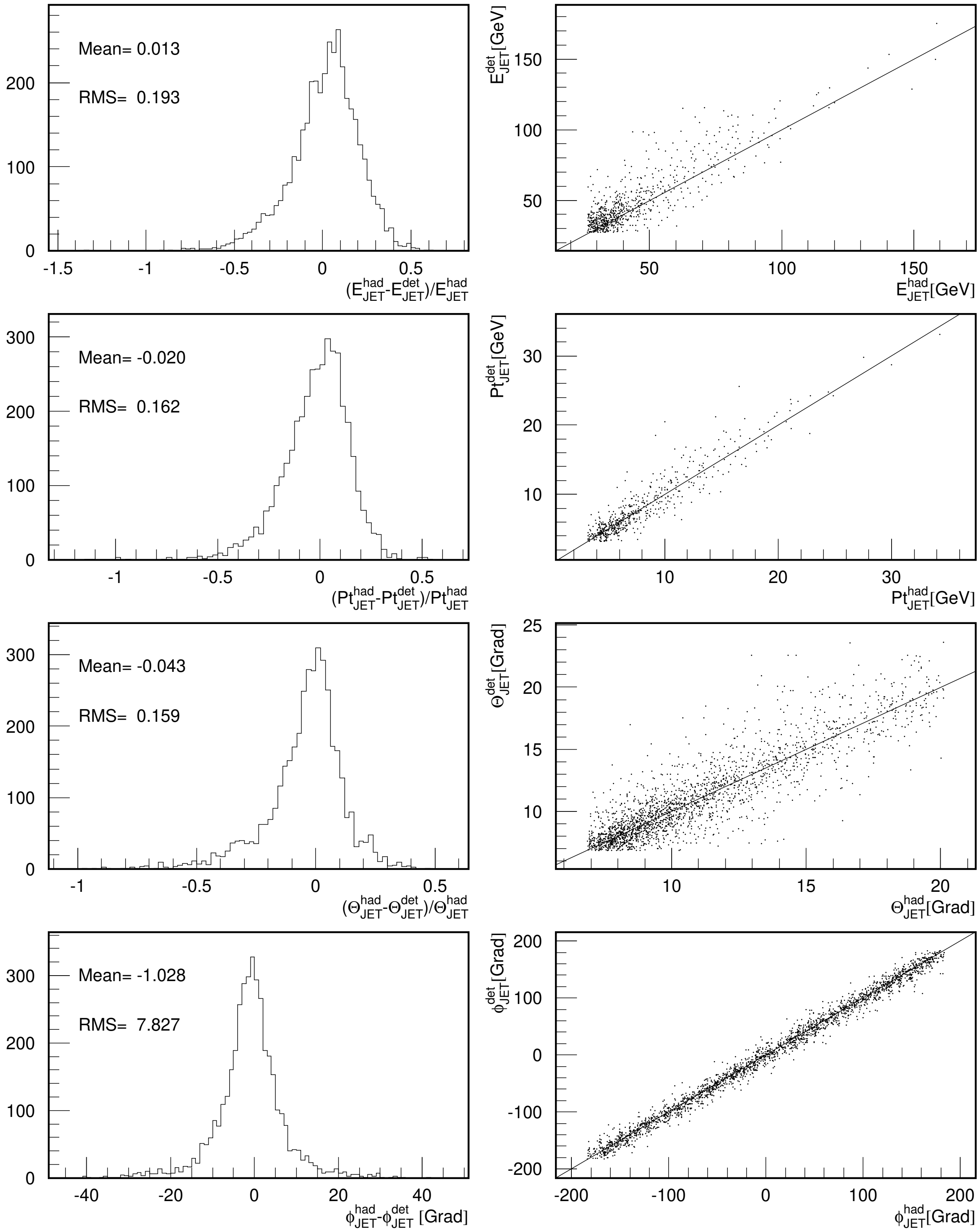

Figure 4.11: Correlation of jets variables in hadron and detector levels in the DJ6+CDM MC for the forward jet sample.

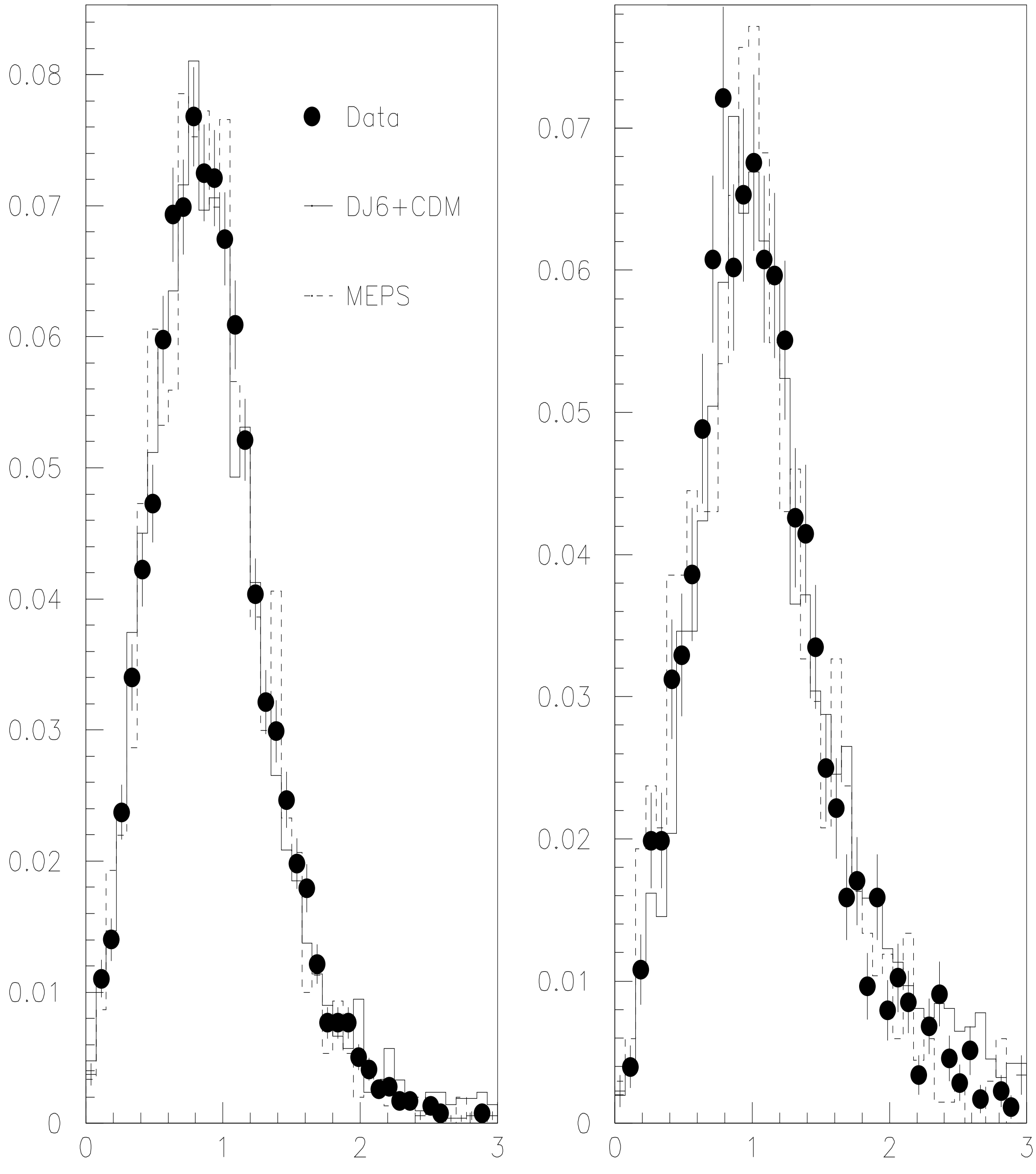

Figure 4.12: P_T balance. The balance between the transverse momentum of the hadronic final and the transverse momentum of the scattered lepton P_T^h/P_T^e of data is compared to the DJ6+CDM and the LEPTO–MEPS MCs for the DIS (left) and the forward jet (right) samples described in the text

the forward jet, i.e., only the cuts on the scattered lepton and kinematics were used. Figure 4.12 shows the variable P_T^h/P_T^e (left the DIS sample, right the forward jet sample) for data, and reconstructed MCs. In table 4.6 the values of a Gaussian fit (for the DIS sample the fit was from $0.3 < P_T^h/P_T^e < 1.3$, whereas for the forward jet sample the corresponding interval was chosen between 0.4 and 1.4) to the distributions shown in figure 4.12 is presented. The variation between data and the MCs is consistent with the findings of other H1 analysis as reported in [95], thus the variation of the event rate due to the change of the hadronic energy scale on ±4%, as proposed in [95], was included in the systematic error (see table 4.7).

4.4 Correction of data for detector effects

Events from the 1994 H1 data taking period are selected according to the scheme presented in chapter 3. Also DJ6+CDM MC events are generated, simulated and are subject to the same analysis chain of the H1 data. In this way the same distributions are plotted for the real and MC samples. It has been shown in this chapter that the DJ6+CDM MC describes reasonable well the shape of data for all relevant distributions. Given this agreement, the same cuts (except CLU_R, D_BEMC_BPC and SQ_CUT) are applied to the generated events at hadron level to obtain a hadron sample. For each observable under study a ratio of its distributions for the hadron level and data MC samples is constructed for each bin. This ratio is multiplied to the contents of the appropriated bin in the distribution of the real data on the observable in question to obtain a corrected real data distribution. This process is called a bin to bin correction and relies on the fact that the MC is able to describe the measured data. E. Mroczko ([96]) has shown that for the forward jet selection the same (within statistical errors) corrected distributions are obtained using either the bin to bin procedure explained here, or the unfolding prescription of d'Agostinni [97].

To estimate the uncertainties caused by the MC model used, the correction functions obtained with DJ6+CDM were compared to those from the LEPTO–MEPS MC. A difference of 7±0.4% in the global correction factor (number of events selected in hadron level divided by the number of selected events in detector level) was found: for DJ6+CDM the correction factor is 0.86±0.02, and for LEPTO-MEPS is 0.79±0.04. The DJ6+CDM MC

Source	Variation	Rate change
Lepton energy scale	+1%	-3.1 %
	-1%	+3.5%
Lepton polar angle	+1 mrad	-1.4%
	-1 mrad	+1.3%
Hadronic energy scale	+4%	+10%
	-4%	-12%

Table 4.7: Global systematic errors.

was selected to correct the data, due to the bigger amount of simulated events and the fact that it includes QED radiative corrections. To the correction functions so obtained a very conservative systematic error of ±7% was added in quadrature to the statistical error given by the finite amount of simulated events.

In summary the events are selected, the remaining background is statistically subtracted, the systematic uncertainties are estimated, added in quadrature with the statistical error and the distributions of interest are corrected to hadron level via a bin to bin correction function.

Chapter 5

Results

The data has been selected and it has been shown to be well understood in terms of cross checks via the H1 detector and the simulated events from the DJ6+CDM MC. Using the procedure described in section 4.4 a number of corrected distributions will be presented in this chapter. They will be compared to MC predictions in hadron level. In addition the results of analytical calculations will be discussed, bearing always in mind that they are only valid for parton level. Tables with the cross section values presented in this chapter can be found in appendix D

5.1 Dependence of the data on x

The total cross section per x bin measured for events from the 1994 data taking period of H1 selected according to the scheme presented in chapter 3 is shown in figure 5.1 where the statistical (inner bars) and systematic error bars are added in quadrature. The distribution of the subtracted background, the influence of the systematic errors in each bin and the correction function used are shown in figure 5.2. Note that most of the background concentrates at low x (mainly photoproduction), that the error due to the uncertainty on the hadronic energy scale dominates in figure 5.2 b).

The data show a strong rise for decreasing x, except for the lowest x bin where there is not enough phase space left due to the PT2_Q2 cut. Also to notice is the size of the error bars dominated by the uncertainty on the appropriate hadronic energy scale to be used for jets measured in the LAr calorimeter and the uncertainty on the correction function due to different MC models. Another important factor is the size of the statistical error bars which is still quite big.

The data points are compared to MC models at the hadron level and to analytical calculations performed at the parton level. Due to the phase space selected in this analysis, it is expected that the cross section for events coming from DGLAP evolution is more and more suppressed with respect to that from BFKL events the smaller x is probed, because lowering x means going away from the DGLAP regime into the region of applicability of BFKL. A numerical confirmation of these expectations can be found in [45], where it is calculated on the one hand the cross section for matrix elements to order α_s^2 in the high energy limit for events surviving the set of cuts used in this analysis and on the other hand the cross section for the same matrix elements, but with the possibility to radiate gluons according to the BFKL equation. These cases, whose relevant diagrams

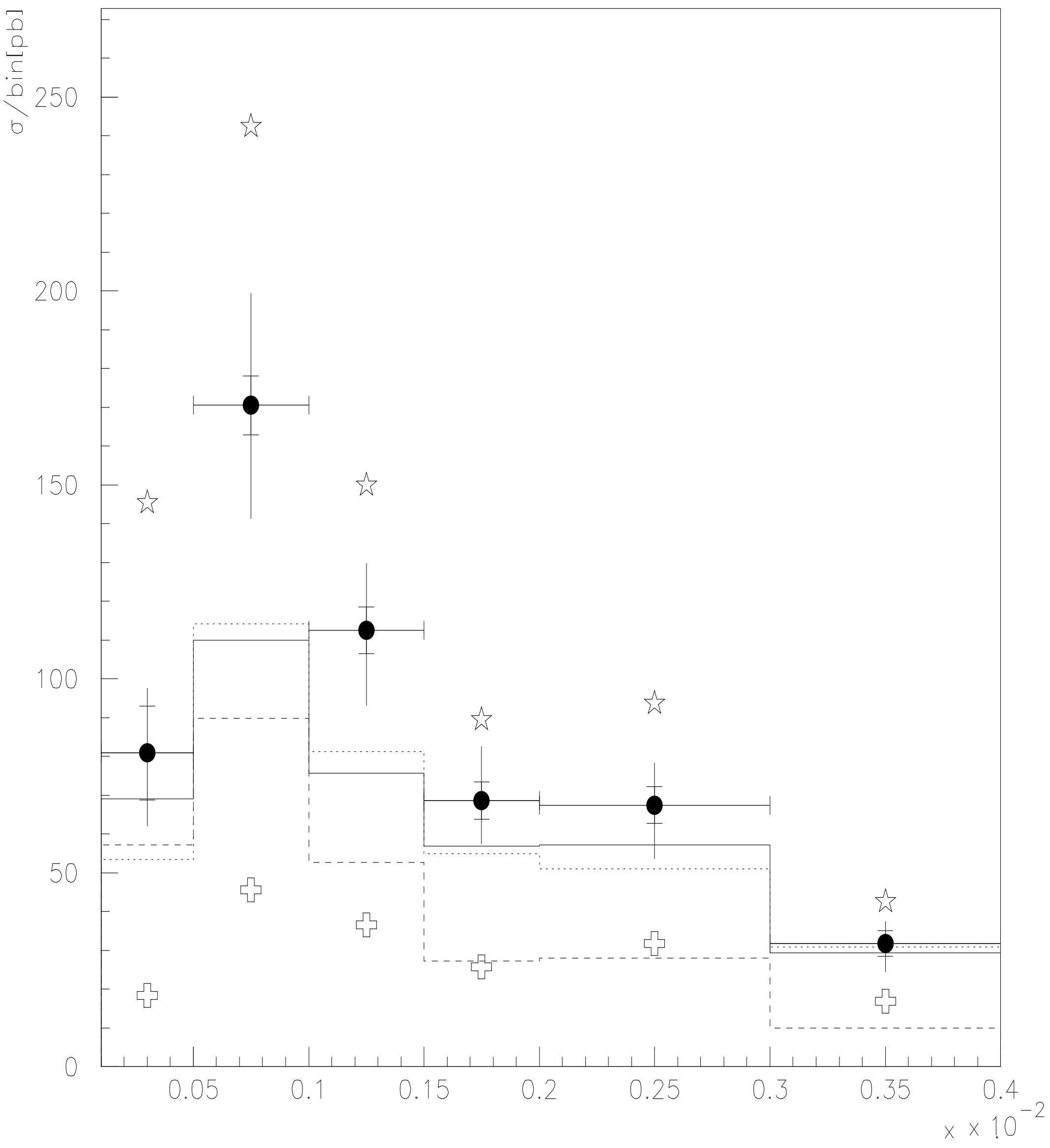

Figure 5.1: Cross sections for the selected events per bin in x. H1 data (full bullets, the inner error bars are statistic error and the outer error bars are the statistic and systematic errors added in quadrature) is shown with statistical and systematic errors added in quadrature. The MC predictions at hadron level are: LEPTO–CDM (solid line), HERWIG (dashed line) and LEPTO-MEPS (dotted line). The result of analytical calculations at parton level from [45] for the BFKL (stars) and Born (crosses) cases, explained in the text, are also shown.

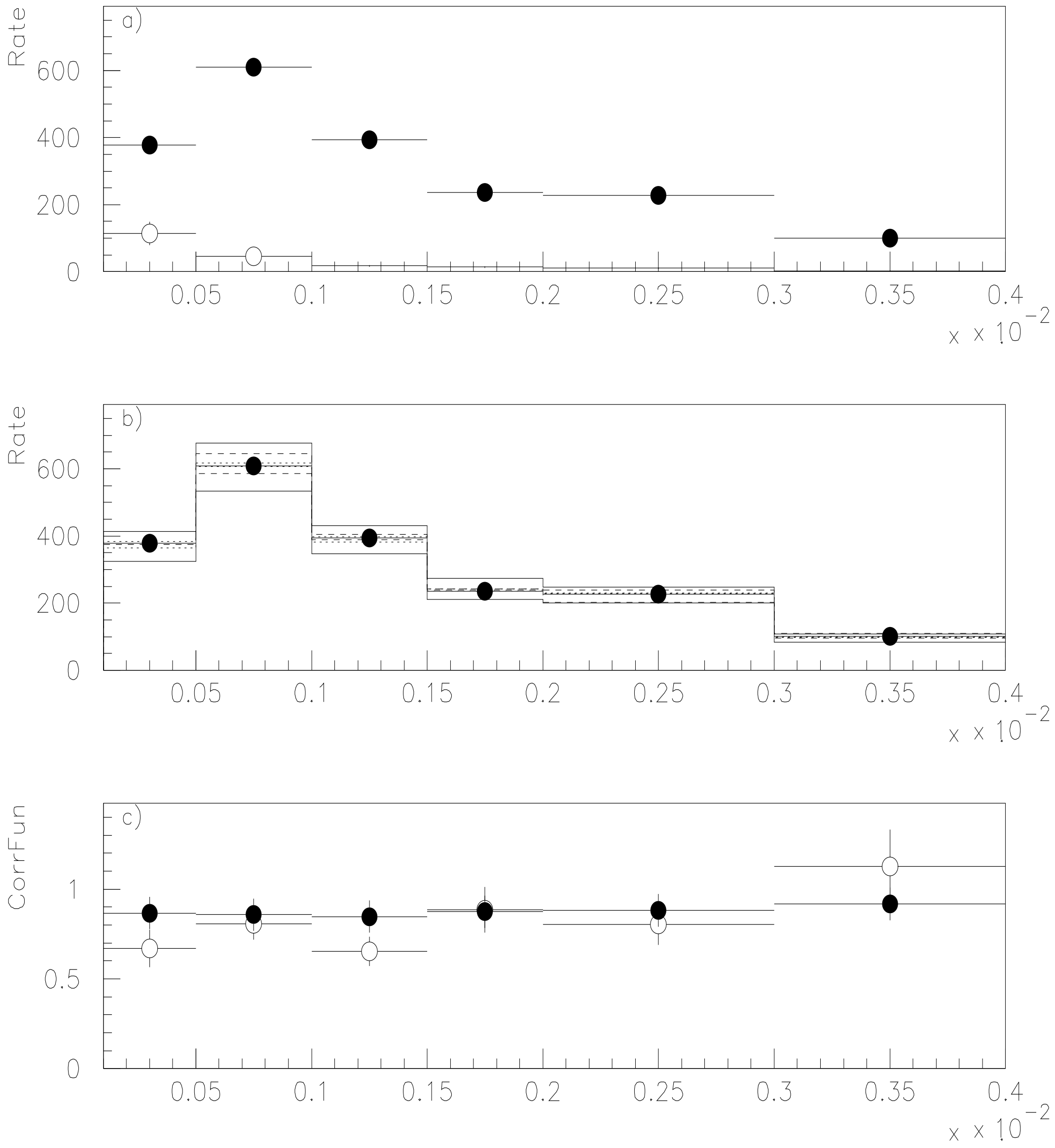

Figure 5.2: Background, systematic errors and corrections factors for the x distribution of forward jet events. In a) the x distribution of the background subtracted via MC (photoproduction plus ISR-QED added in quadrature) is shown in empty bullets and compared to the total rate of forward jet events prior to the subtraction of the background (full bullets). The change in the forward jet rate (full bullets) due to the variation of the hadronic energy scale (solid line), lepton energy (dashed line) and polar angle of the lepton (dotted line) is shown in b). The correction functions obtained from DJ6+CDM (full bullets) and LEPTO–MEPS (white bullets) are shown in c).

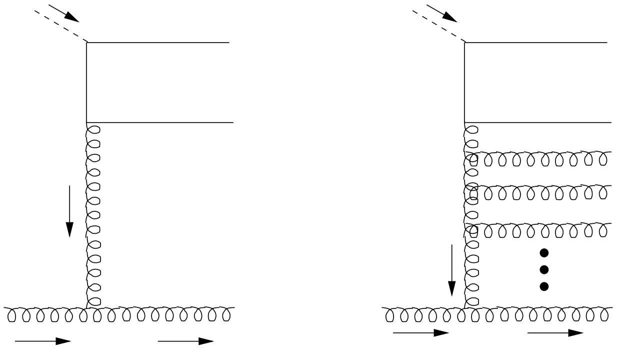

Figure 5.3: Diagrams for the Born and BFKL cases from [45]. They correspond to the matrix elements to order α_s^2 in the high energy limit with (right) and without (left) BFKL radiation.

are shown in figure 5.3, will be called Born and BFKL respectively to keep the notation used by the authors.

The result for both of them is also shown in figure 5.1. It is worthwhile to emphasize again that the comparison of analytical calculations to data corrected to hadron level has to be done with the utmost care. Nevertheless it can be seen that the data lies between both cases and that it would probably stay so with the addition of hadronization to the theoretical prediction, because the experience has shown that for hard processes i.e. jets, this is normally a relatively small effect (see for example the first chapter of [8]. To study this, the PT_J cut was varied from its value of 3.5 GeV to 5 and 6 GeV respectively. The results of this variations can be seen in figure 5.4. Note that in spite of the higher PT_J cut which would suggest less influence of hadronization in the parton level predictions the data remains always between the BFKL and the Born cases. The analytic predictions were calculate in [98].

Comparing now the MC predictions based in the leading log DGLAP equations (LEPTO–MEPS and HERWIG) and the CDM model (LEPTO–CDM) to the measured data it is seen (figure 5.1) that data is well above the MC and that the difference among them increases with decreasing x. Both LEPTO MC have a comparable cross section and the HERWIG MC has a smaller cross section. Here it should be noticed that in HERWIG a lot of events (amounting to 20–30% of the total cross section) are produced with a rapidity gap between the proton remnant and the hard process. Due to these spurious events there is a uncertainty in the total cross section for the HERWIG prediction. Even if their contribution to the cross section were subtracted, the data would stay above the MC prediction. The importance of the events at low x is also seen in figure 5.4 where a bigger PT_J cut rejects, due to the PT2_Q2 cut, predominantly low x events and induces a better agreement between data and the LEPTO MCs.

To get a deeper insight the distribution of the cross section in x bins is also presented for two bins in the forward jet energy, which for partons is related to x_j via $x_j \approx E_j/p_0$, where p_0 is the energy of the incoming proton beam. Due to the different ordering of

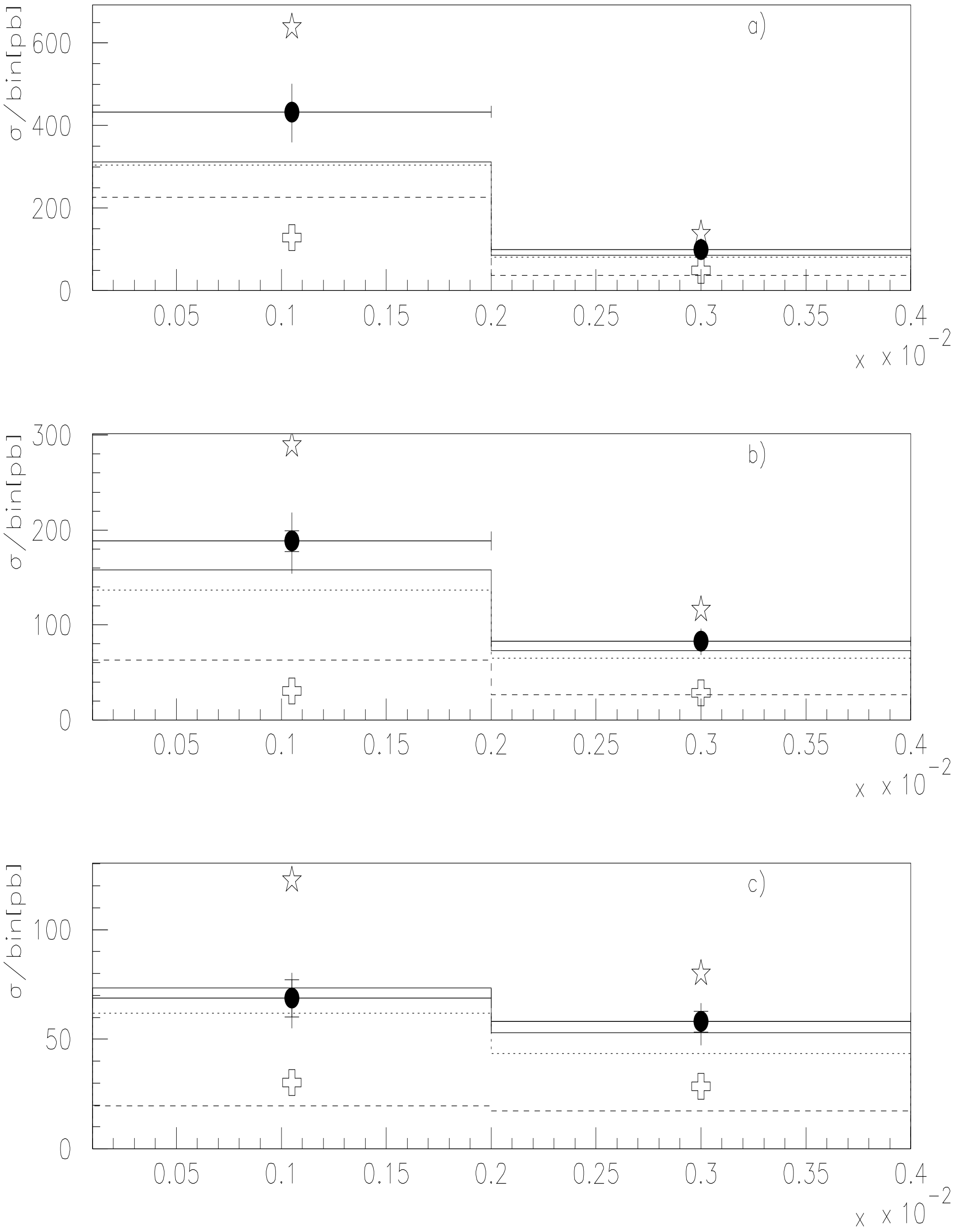

Figure 5.4: The cross section per bin in x for forward jets events for different PT_J cuts. The notation is explained in figure 5.1. The cases where the PT_J cut took the value of 3.5, 5.0 and 6.0 GeV are shown in a), b) and c) respectively.

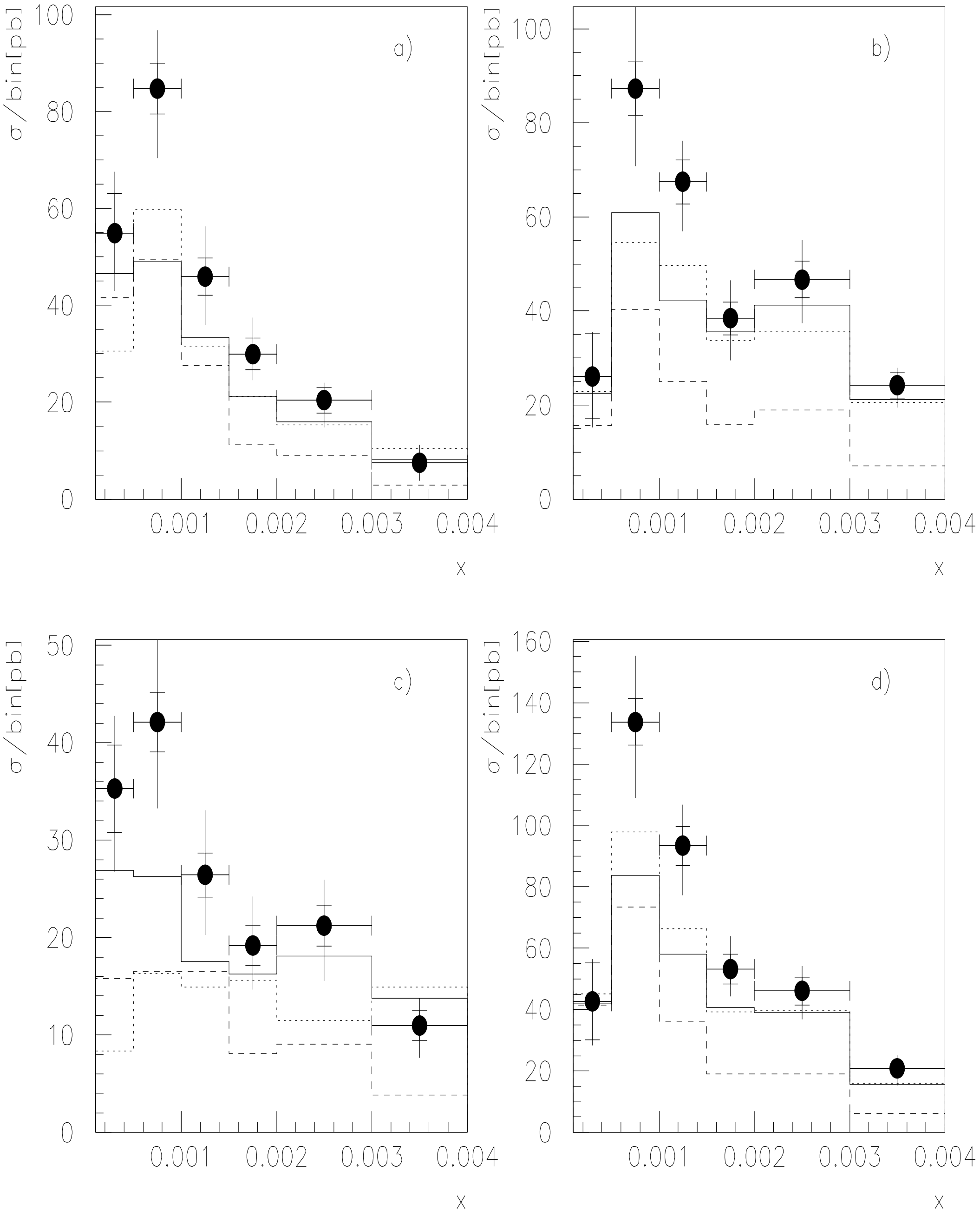

Figure 5.5: Cross section of forward jet events per bin in x for two ranges in E_J and E_T^C. The notation is explained in figure 5.1. The selected ranges are $E_j < 32.8$ GeV (a), $E_j > 32.8$ GeV (b), $E_T^C < 5.0$ GeV (c) and $E_T^C > 5.0$ GeV (d).

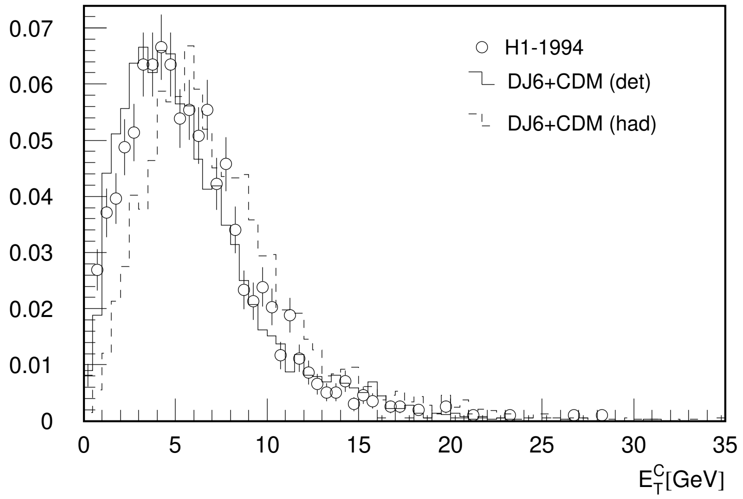

Figure 5.6: Distribution of E_T^C. Note that again the DJ6+CDM MC produce a reasonably good description of the data, but the MC distribution for hadrons is harder than in detector level. This can be understood due to the H1 magnetic field, material between the interaction point and the calorimeter and the existence of cracks and irregularities in the LAr calorimeter.

the longitudinal momenta of the partons along the ladder to increase x_j should enlarge more the available phase space for BFKL than for DGLAP evolution. The bins (chosen to have about the same number of measured events) are $E_j < 32.8$ GeV and $E_j > 32.8$ GeV (see plots a) and b) in figure 5.5).

The ladder diagram in figure 1.2 shows besides the parton giving rise to the forward jet, several other partons and the quark box on top of them, so the next natural question is to consider which role do they play. To do it the variable E_T^C (shown in figure 5.6) is defined as the sum of the transverse energy deposited between the rapidities $\eta_j - 1.5 * R_j$ and -1.31 corresponding to a polar angle of 150^o. Here the radius of the jet has been taken $R_j = 1$. These limits mirror the ones used to define the SQ_CUT. The bins (also chosen to have about the same number of measured events) are $E_T^C < 5.0$ GeV and $E_T^C > 5.0$ GeV (see plots c) and d) in figure 5.5).

The correction functions for the four cases shown in figure 5.5 are presented in plots a)–d) of figure 5.7. The shift of the hadron distribution with respect to that in the detector level for the E_T^C variable (see figure 5.6) is the source of the variation in the value of the correction functions c) and d) in figure 5.7. For all four cases shown in figure 5.5 the same conclusion applies: The difference between data and MC concentrates at low x, except for the lowest x bin where, as already pointed out, there is not enough phase space left due to the PT2_Q2 cut.

In summary the MC fail to describe the data in the low x region, and the comparison with analytical predictions seems to indicate that the sample consist of events whose origin is compatible with a mixture of DGLAP and BFKL evolution.

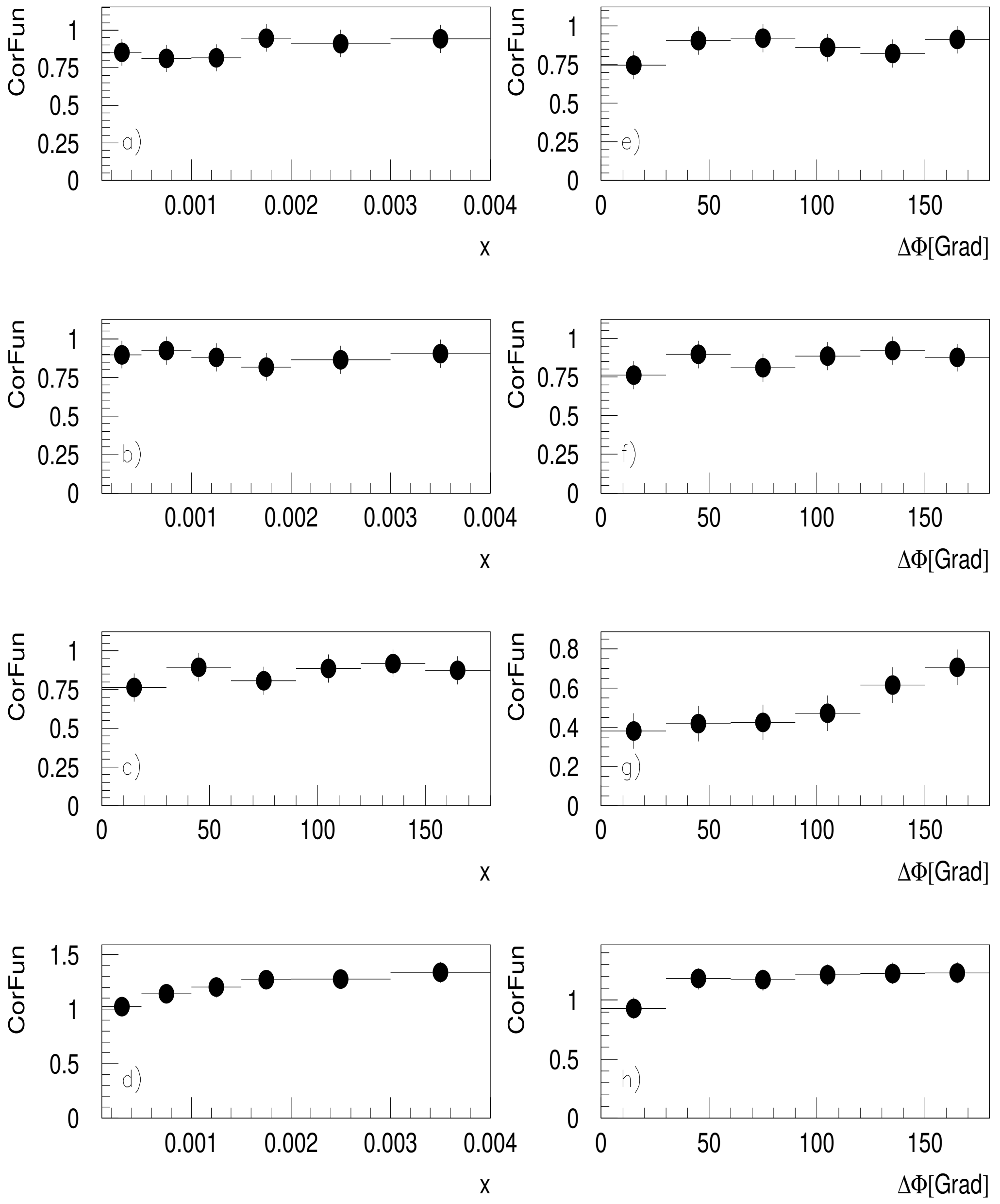

Figure 5.7: Correction functions for the different cross sections. They are defined as number of selected events in detector level divided by the number of selected events in hadron level. The MC used is DJ6+CDM and in plot a) the correction function for the $E_j < 32.8$ GeV case is shown, in b) for $E_j > 32.8$ GeV, in c) and g) for $E_T^C < 5.0$ GeV, in d) and h) for $E_T^C > 5.0$, in e) for x in (0.0001,0.002) and in f) for x in (0.002,0.004).

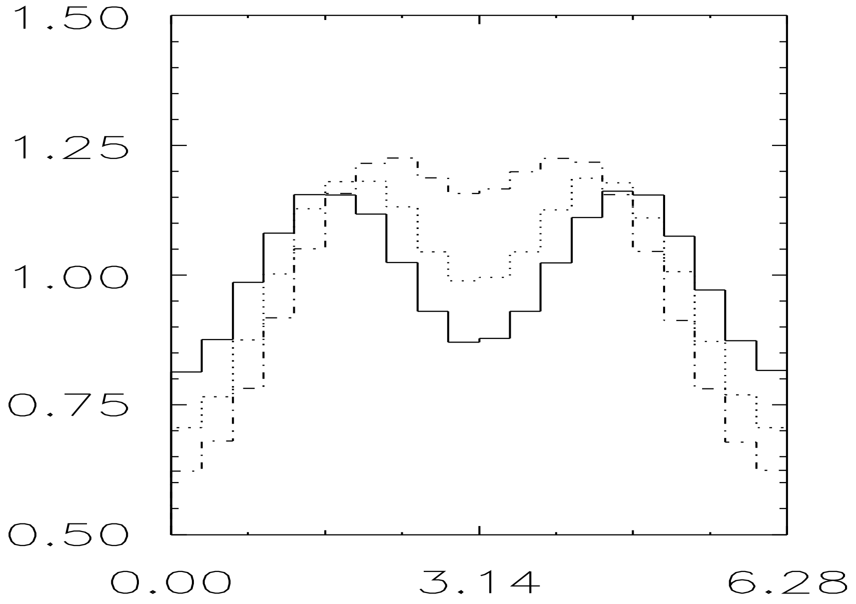

Figure 5.8: The variable $\Delta\phi = \phi_e - \phi_j$ for three different x bins:(0.0002,0.0004) solid line, (0.0018,0.002) dots and (0.0034,0.0036) (dots and dashes) for the Born case of reference [45]. The scale is arbitrary.

5.2 Correlation of the jet and lepton azimuthal angles

The increased amount of radiation in the middle of the ladder (*cf.* figure 1.2) for the BFKL case with respect to the DGLAP evolution dilute the correlation between the azimuthal angles of the scattered lepton and the forward jet, which for the naive parton model where the forward jet would come from the struck quark, is complete because, due to momentum conservation, they have to be back to back. So the variable $\Delta\phi = \phi_e - \phi_j$, where ϕ_e and ϕ_j are the azimuthal angles of the scattered lepton and the forward jet respectively may yield information about the dynamics of the ladder.

The predictions are [45] that for the BFKL diagrams the variable $\Delta\phi$ will show a flat behavior, while their expectations for the Born case are shown in figure 5.8 for three different x bins: The smaller x the more that QCD radiation alters the correlation.

The points measured by H1 for the $\Delta\phi$ observable are shown folded in π in figure 5.9 where the statistical (inner bars) and systematic error bars are added in quadrature. The distribution of the subtracted background, the influence of the systematic errors in each bin and the correction function used are shown in figure 5.10. Note that the subtracted background is flat in $\Delta\phi$ and hence does not influence the measurement. Also it is worth to take into account that the error bars are strongly correlated: when the hadronic energy scale is varied, the rate in every bin changes in the same direction, for +4% the rate increases, for -4% it decreases (see figure 5.10 b).

Data show a behavior consistent with the Born prediction for x in [0.0034,0.0036]

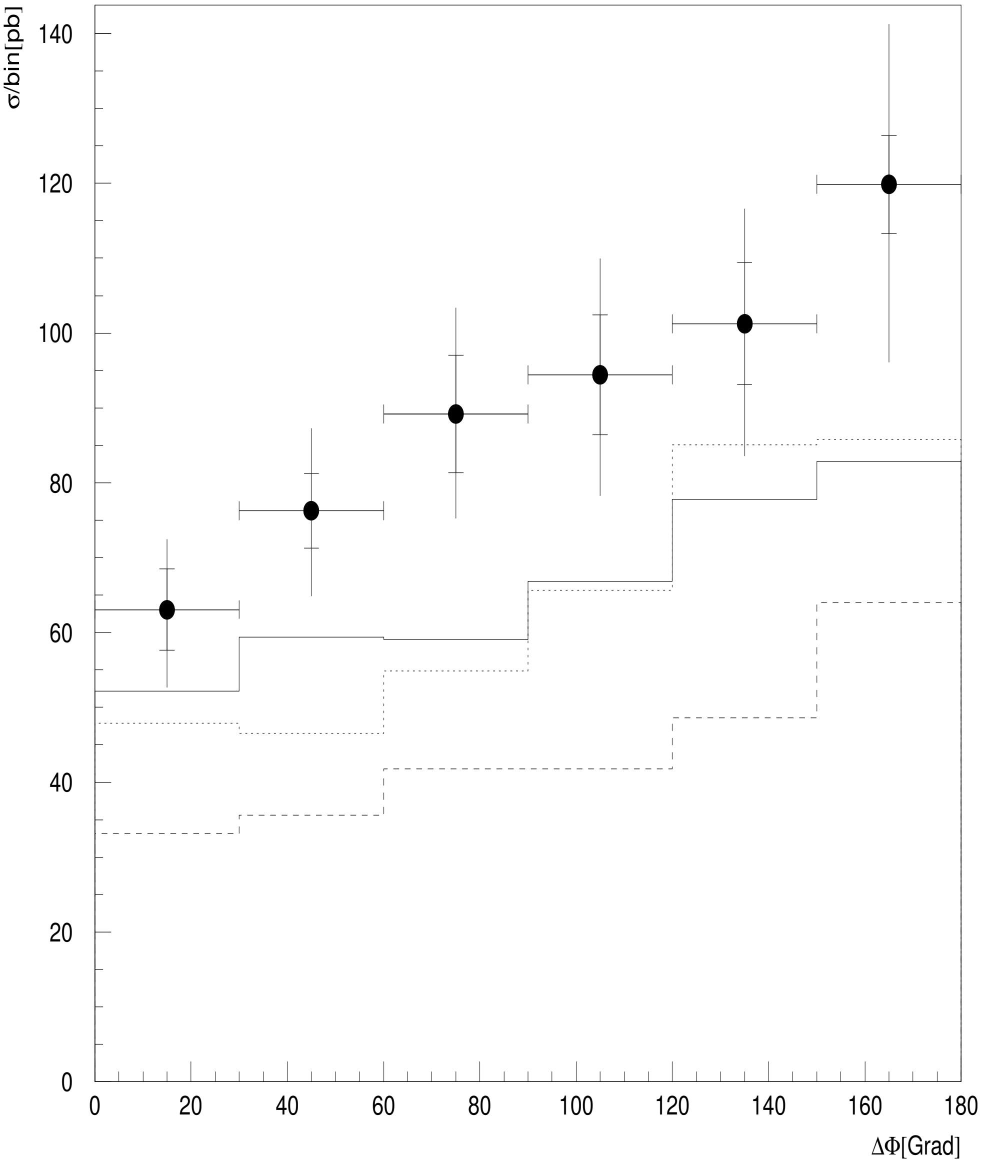

Figure 5.9: Cross sections for the selected events per bin in $\Delta\phi$. H1 data (full bullets) is shown with statistical and systematic errors added in quadrature. The MC predictions at hadron level are: LEPTO–CDM (solid line), HERWIG (dashed line) and LEPTO-MEPS (dotted line).

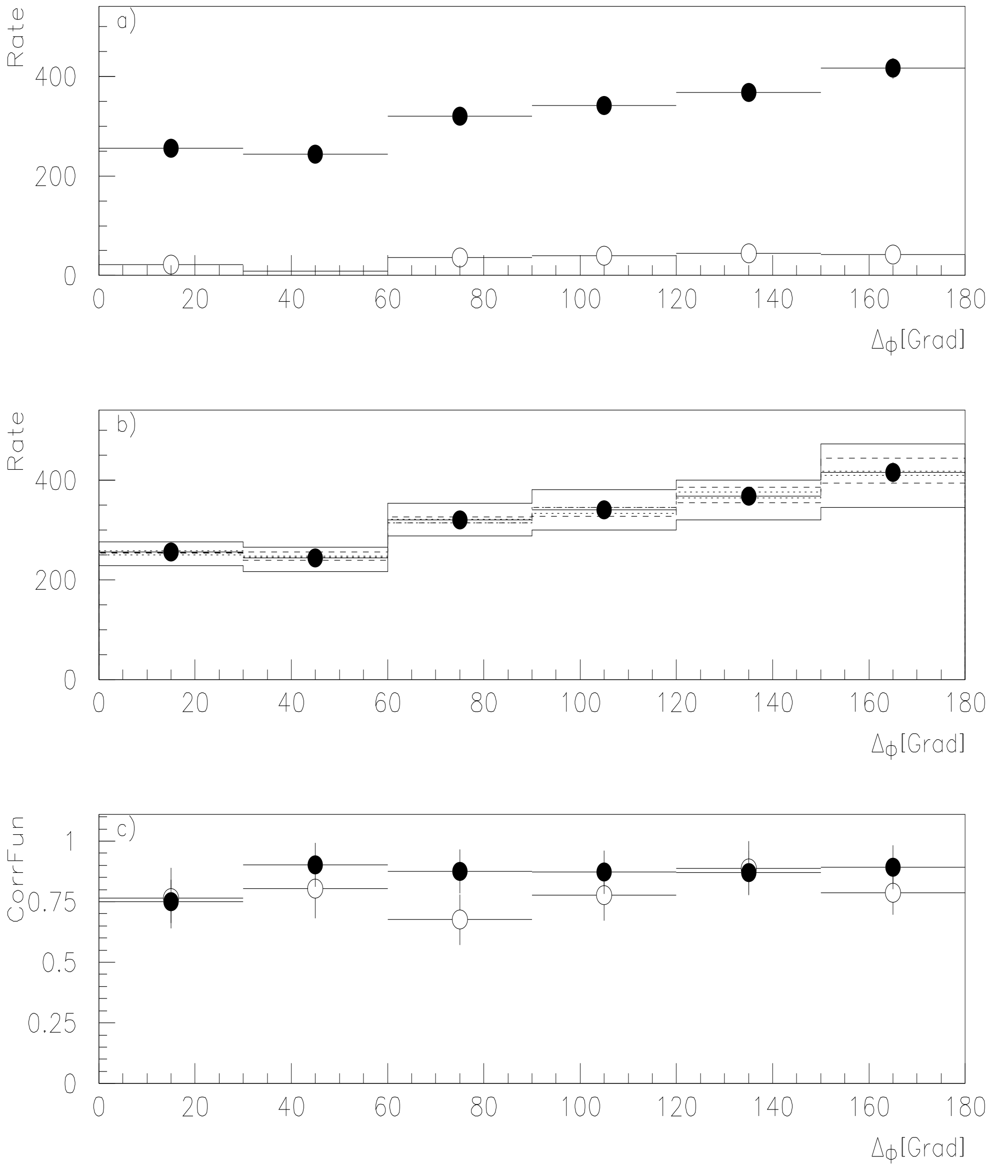

Figure 5.10: Background, systematic errors and corrections factors for the $\Delta\phi$ distribution of forward jet events. In a) the $\Delta\phi$ distribution of the background subtracted via MC (photoproduction plus ISR-QED added in quadrature) is shown in empty bullets and compared to the total rate of forward jet events prior to the subtraction of the background (full bullets). The change in the forward jet rate (full bullets) due to the variation of the hadronic energy scale (solid line), lepton energy (dashed line) and polar angle of the lepton (dotted line) is shown in b). The correction functions obtained from DJ6+CDM (full bullets) and LEPTO–MEPS (white bullets) are shown in c).

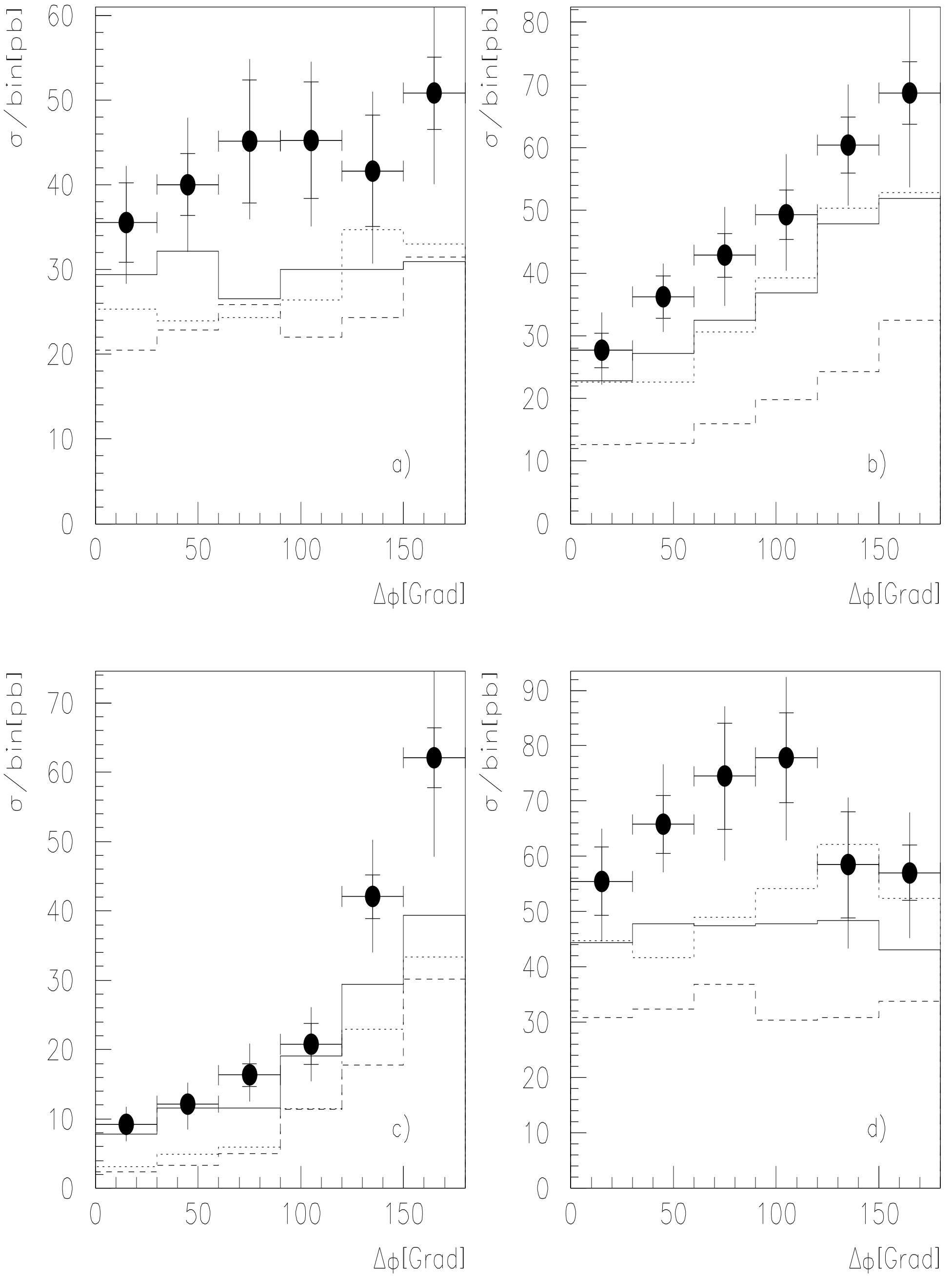

Figure 5.11: Cross section of forward jet events per bin in $\Delta\phi$ for two ranges in x and E_T^C. The notation is explained in figure 5.9. The selected ranges are $0.0001 < x < 0.002$ (a), $0.002 < x < 0.004$ (b), $E_T^C < 5.0$ GeV (c) and $E_T^C > 5.0$ GeV (d).

(compare full bullets in figure 5.9 to the dash–dotted line of figure 5.8) with an increase of about a factor two from the first to the last bin in $\Delta\phi$. The shape of the MC appears to be not so steep as the data.

It is interesting to see if this behavior is indeed dependent on x. Plots a) and b) of figure 5.11 show the $\Delta\phi$ variable for two bins in x: (0.0001,0.002) and (0.002,0.004) respectively. The corresponding correction functions are shown in plots e) and f) in figure 5.7. Here indeed a complete different behavior is observed for both x ranges: the plot corresponding to lower x is flatter than the one at bigger x (remember that the error bars are correlated as shown in plot b) of figure 5.10). Nevertheless the MC offer a similar shape for both cases.

The last point to discuss in this section is the behavior of $\Delta\phi$ for different E_T^C ranges (see two lower plots in figure 5.11 for the cross section and plots g) and h) in figure 5.7 for the corresponding correction functions). The cross sections have again a very different behavior for both ranges in E_T^C. In the first case there is again a strong rise of the distribution, this time up to a factor 6 from first to last bin, while in the second plot the cross section shows a behavior similar to the Born case for x in (0.0018,0.002) (see figure 5.8).

Here should be noticed that these observables, E_T^C and $\Delta\phi$ are slightly correlated for the case $E_T^C < 5$ (see figure 5.12). This correlation has a kinematic origin: when there is few transverse energy deposited between the scattered lepton and the forward jet, four momentum conservation tend to put them back to back. Its effect is clearly seen in the correction function (plot g) in figure 5.7).

There is no clear conclusion for the $\Delta\phi$ observable. On one hand the MC seem to follow more or less the trend of the data for all the cross sections shown, indicating that

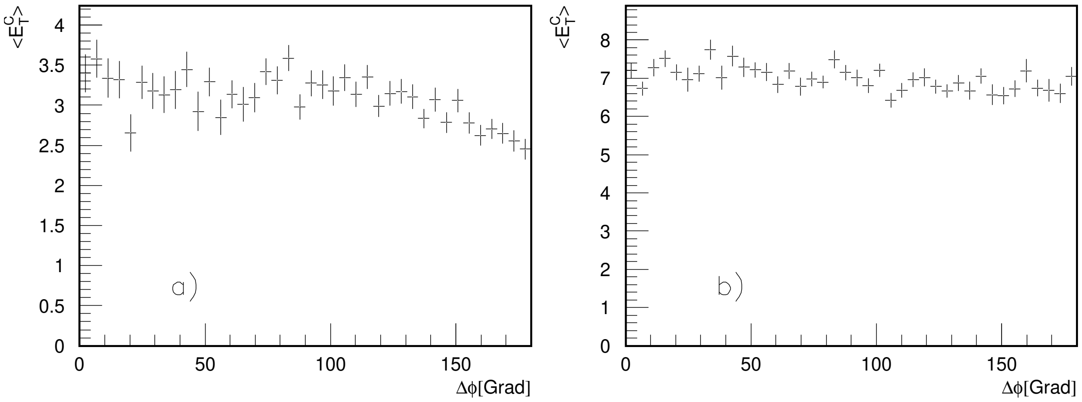

Figure 5.12: Correlation between E_T^C and $\Delta\phi$. Every point is the average of the values in the bin, and the error bars correspond to the spread of these values. The events are from the DJ6+CDM MC. For data the same behavior is observed (within statistical fluctuations).

the dominant effect may has a kinematic and not a dynamic origin. On the other hand this observable is quite sensitive to the x range chosen and also to the amount of central transverse energy. The analytical calculation are not really conclusive: for the two bins in x it would seem that for large x the Born cases is the adequate, whereas the distribution for low x looks a lot more flatter and could well be assigned to both the BFKL and the Born case. It would be definitely very interesting to have more statistics to study the small x behavior (say for x below 0.001) of $\Delta\phi$ for different ranges in E_T^C. Nevertheless when drawing conclusions it should not be forgotten, that the cross section of data is well above the cross sections predicted by the MC models.

5.3 Events with two forward jets

From the 1945 events selected, 52 have a second jet fulfilling all forward jet cuts. The total cross sections for the case of at least one forward jet and the case of two forward jets are presented in table 5.1.

It should be stressed that for the small amount of events and the existence of extra migrations due to the second jet a simple correction factor may be a too coarse procedure. Nonetheless this part of the analysis is only to shed light in the possibilities that the study of these two jet events offer.

These two forward jet events do not concentrate in a given x or $\Delta\phi$ bin. Further observations are that both forward jets are always back to back for the data and the MCs. This is according to expectations: the two forward jets are produced in neighbor rungs along the ladder (figure 1.2), so due to local momentum conservation they are expected to be back to back; on the other hand the correlation between the forward jets and the scattered lepton is washed out due to the emission of radiation between them. These observations are shown in figure 5.13. The two forward jet events also fulfill the condition $0.5 < p_{T_j1}^2/p_{T_j2}^2 < 2.0$. A more precise study can not be done due to the smallness of the sample.

	At least one jet	**Two jets**
Data σ[pb]	$531\pm^{84}_{91}$	$6.0\pm^{3.3}_{3.2}$
LEPTO–CDM	398	5.6
LEPTO–MEPS	385	4.2
HERWIG	265	3.4

Table 5.1: Total cross section for the forward jet cuts and the cases of at least one forward jet and exactly 2 forward jets given in pb.

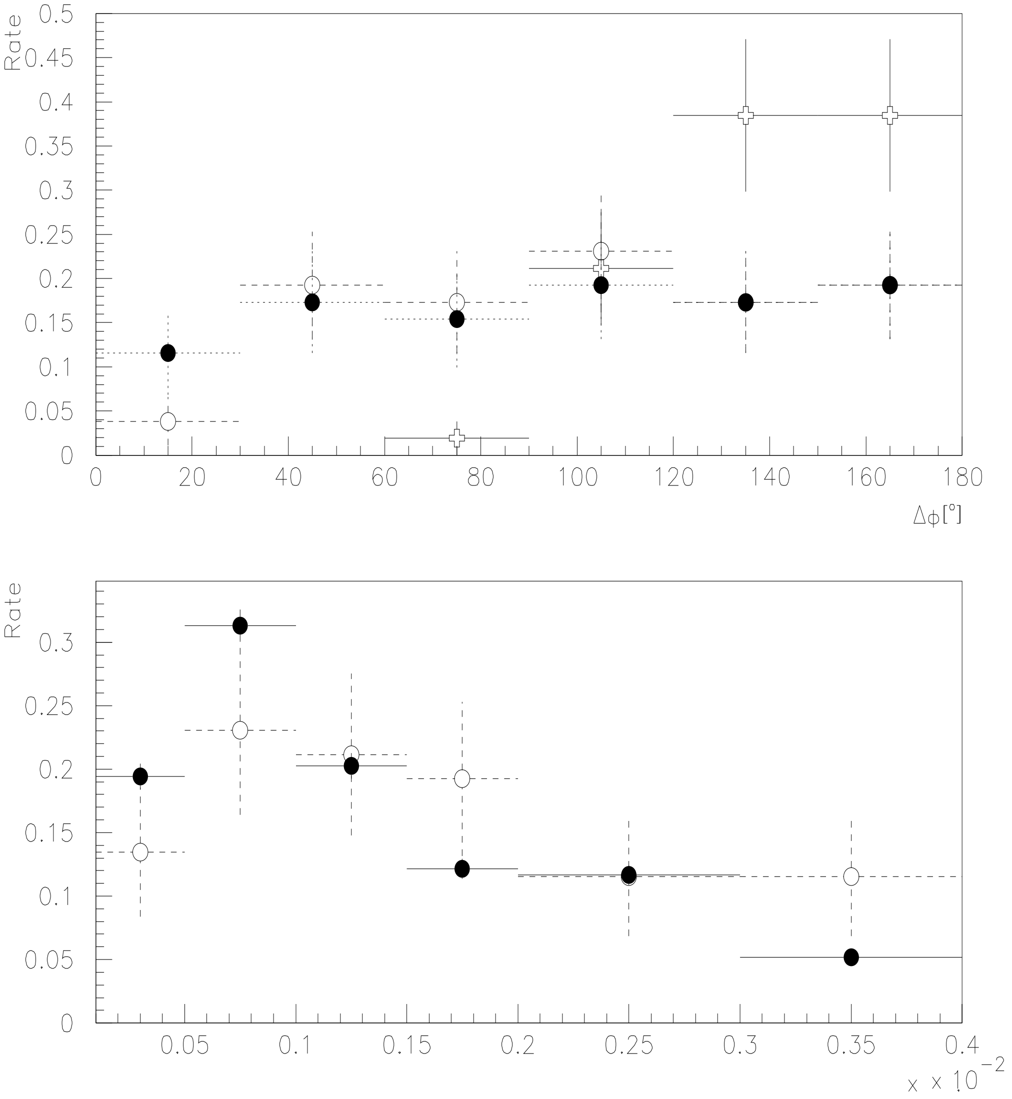

Figure 5.13: Two forward jet events. The rate of events with two jets surviving the forward jet selection are shown. In the upper plot the azimuthal difference between the first forward jet (the one with the highest energy) and the lepton is shown with empty bullets and dashed error bars due to statistics. The same for the second jet and the scattered lepton is shown with full bullets and dotted error bars. Finally the azimuthal difference between both forward jets is shown with crosses and solid error bars. In the lower plot the x distribution is shown for the forward jet sample (full bullets) and for those events of the forward jet sample which have two forward jets (empty bullets). All histograms were normalized to unit to compare the shapes.

5.4 Conclusions

On the one hand a measurement has been performed and the distributions for the dependence of the cross section in x and $\Delta\phi$ for a number of cases have been presented along with the fraction of two forward jet events. These measurements exhibit large error bars caused mainly by the uncertainty on the hadronic energy scale, the uncertainty in the correction function due to different MC models and the small amount of selected events. None of the MCs describes the data. It should be stressed that these MC describe a number of other distributions in DIS and also in e^+e^- and/or $p\bar{p}$ colliders (see for example [79]) so these discrepancies are interesting to say the least.

On the other hand is the interpretation of this measurement. With regard to the motivation of the selection, namely the issue of BFKL versus DGLAP evolution equations it can be said that the analytical calculations suggest a mixture of both cases for the cross section in x bins, but fail to describe the behavior for the cross section in $\Delta\phi$ bins. Unfortunately there is to date no available BFKL MC, which would help to draw stronger conclusions.

Finally it must be clear that the measurement is independent of its motivation and the discrepancies observed in the comparison of the data to the MCs could have their origin not necessarily on BFKL phenomena, but on something else. Nevertheless the fact that BFKL effects offer a natural explanation of these differences is encouraging from the point of view of Mueller's proposal and the quest to understand partonic dynamics at low x.

Chapter 6

Summary

In this work the selection of deep inelastic events with a jet at high rapidities in the frame of the H1 experiment has been presented and used to extract cross sections at particle level for the following observables:

- The first measurement here presented consist in studying the behavior of the cross section as x varies. It has been found that the measured cross section lies well above the predictions of different MC models and that analytical calculations are compatible with the assumption of a mixed contribution of DGLAP and BFKL effects. The x dependence of the cross section was also presented for the first time for different bins in the jet energy and in the amount of energy between the scattered lepton and the forward jet.
- The correlation of the azimuthal angles of the scattered lepton (ϕ_e) and forward jet (ϕ_j) was for the first time presented here in the form of a cross section in bins of $\Delta\phi = \phi_e - \phi_j$. It has been shown that the $\Delta\phi$ behavior of the cross section varies strongly for different ranges in x and the amount of energy between the scattered lepton and the forward jet. The analytical calculation are not really conclusive: for the two bins in x it would seem that for large x the Born cases is the adequate, whereas the distribution for low x looks a lot more flatter and could well be assigned to both the BFKL and the Born case.
- Finally and also for the first time the cross section for events having two forward jets was presented along with some comments on the behavior of such events.

It should be stressed that the measurement is completely independent of its motivation, namely BFKL versus DGLAP dynamics in the proton, so the results of this analysis can be directly compared to any model. It is also important to note that although the MC programs used in this analysis failed to reproduce the measured characteristics of the forward jet data, they have been quite successful in describing other observables in DIS, e^+e^- and $p\bar{p}$ collisions. Thus the discrepancies found in this analysis between the measurements and the expectations of the models will contribute to our understanding of the proton structure.

Appendix A

Clusters versus cells in the forward region of the LAr calorimeter

In section 2.6.1 was mentioned that that it was better to use cells than cluster in the forward region of the LAr calorimeter (wheels IF and OF in figure 2.6). Here the reason will be explained.

Once the cells which survived the noise cuts are selected they are used as input for the clustering algorithm of H1. This algorithm tries to merge cells which are near each other. To do this it must take into account the mechanical design of the calorimeter.

In section 2.6.1 it was mentioned that each wheel is formed out of eight modules named octants. From the mechanical point of view this is only true for wheels BB, CB and FB. The wheels OF and IF are formed by two halves screwed together as seen in figure A.1. The existence of separated octants in wheels BB, CB and FB, produce the so called ϕ cracks between neighboring octants. If a particle goes into a ϕ crack the energy deposition will be separated in signals in two octants and loss of signal in the crack. The cluster algorithm tries to take this effect into account by unifying into a cluster cells from both sides of the cracks. On the other hand the forward wheels of the LAr calorimeter do not have ϕ cracks, but the clustering algorithm assumes they do. This produces an artificial increase in the number of cells per cluster in the places of the assumed cracks (see figure A.2), which in turn produces a structure in the transversal energy distribution of the azimuthal angle of the clusters in the IF and OF wheels as shown in figure A.3, where the case of clusters with more than 3 GeV was chosen, because clusters with small energies (and they are the majority) are formed by few cells or even by just one cell and then the effect of the clustering of cells assuming ϕ cracks is not so clear.

As this effect is an artifact of the cluster algorithm and as the jet algorithm used in this analysis is in principle independent from having cells or clusters as input it was decided to use cells to build the forward jets.

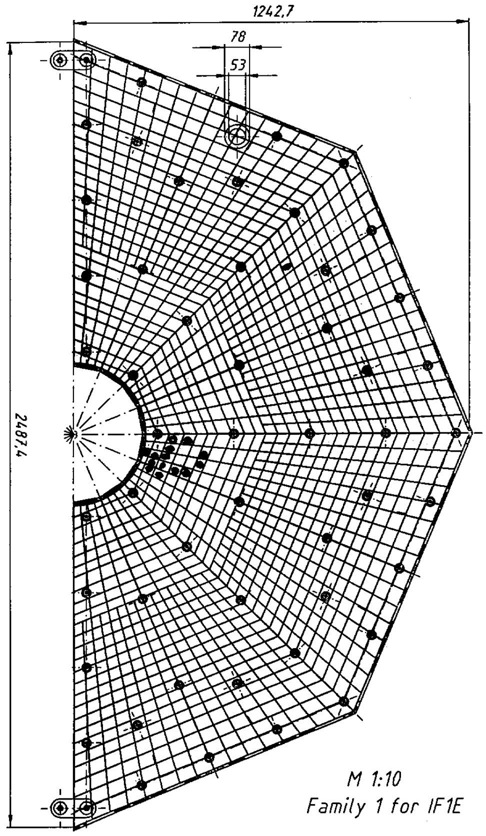

Figure A.1: The IF wheel of the LAr calorimeter. A plate of one of the two halves which form the mechanical structure of the LAr calorimeter is shown.

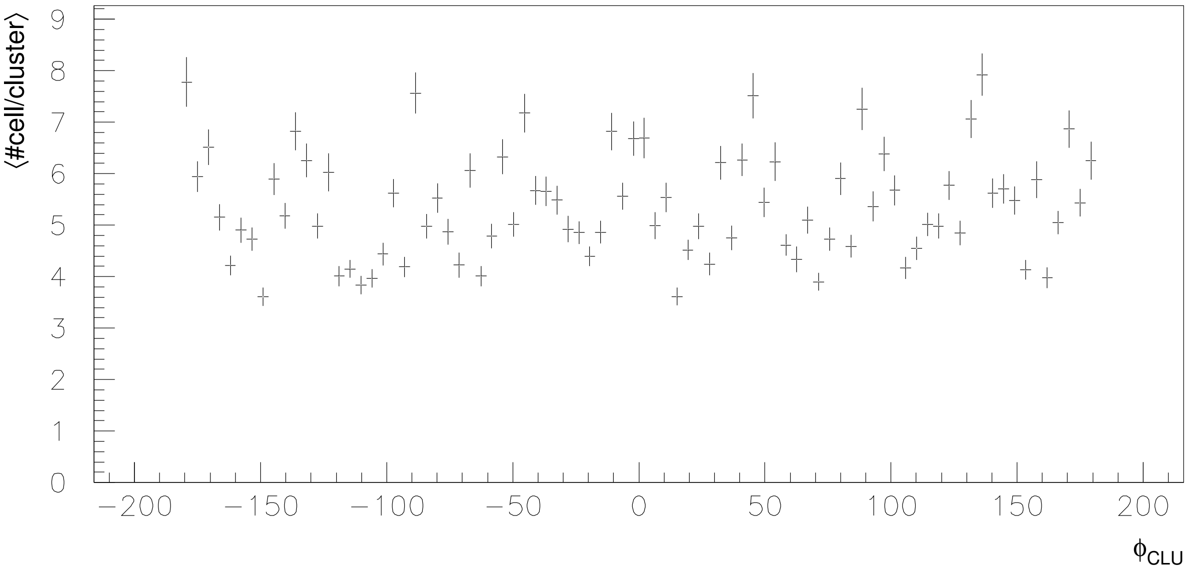

Figure A.2: Azimuthal distribution of the number of cells per cluster in the IF/OF wheels of the LAr calorimeter

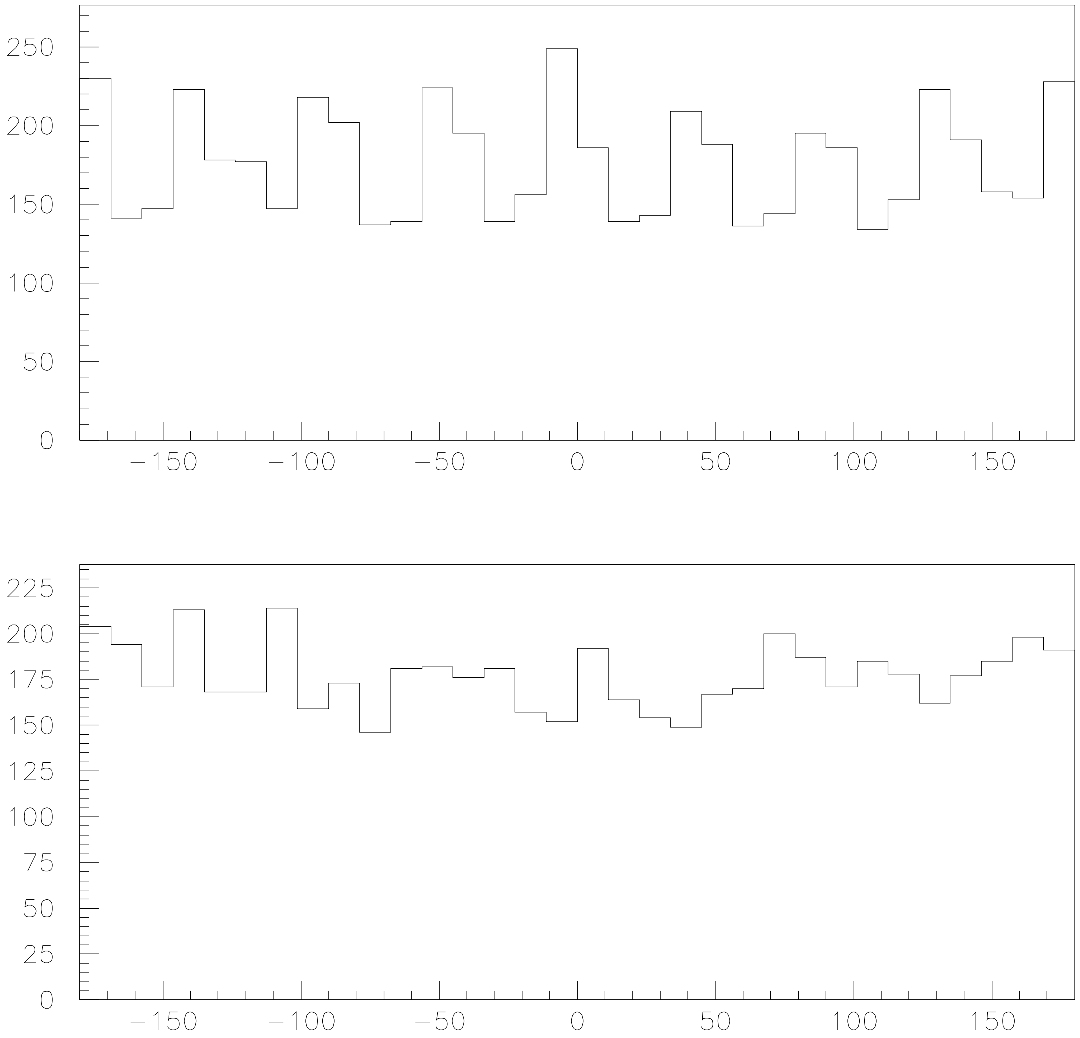

Figure A.3: Azimuthal distributions of objects in the forward wheels of the LAr calorimeter. Distribution of the azimuthal angle of clusters (upper plot) in the forward wheels of the LAr calorimeter, for cluster whose energy is bigger than 3 GeV. Azimuthal distribution of the cells (lower plot) which build the clusters shown in the upper plot.

Appendix B

The modified CONE jet algorithm

The standard cone algorithm used in H1 [74] is defined in the (η, ϕ) plane. There a grid is defined. This grid has NRAPB times NAZMB cells, where NRAPB is the number of cells in pseudorapidity and NAZMB the number of cells in the azimuthal coordinate. The η variable expands the interval (-RAPMAX,RAPMAX), while the whole 2π of the azimuthal variable is taken into account.

The transverse energy E_t of the input objects, in the case of this analysis the cells of the LAr calorimeter, are filled in this grid. Here the Snow Mass convention [72] is used: The transverse momentum of two objects is the sum of the respective transverse momenta. Note that this convention is not covariant.

Once the grid is filled, all those cells with transverse energy E_{tc} bigger than ETMIN are considered as a possible initiator of a jet and with them a list in decreasing order of E_{tc} is built. Starting with the cells with the higher E_{tc} a jet candidate is built as follows: loop over all cells in the grid and select those which are closer to the initiator than the parameter R_j defined as

$$\sqrt{(\eta_{initiator} - \eta_{cell})^2 + (\phi_{initiator} - \phi_{cell})^2} < R_j.$$

Then the transverse energies of all selected cells are added using the Snow Mass convention to form the transverse energy of the jet candidate E_j. If E_j is bigger then the parameter ETSMIN the candidate is accepted as a rightful jet, all the cells which were assigned to it are locked so that they can not belong to another jet and the procedure of forming a jet candidate is repeated with the next initiator in the list until the list is empty.

In summary the standard H1 cone algorithm uses following input parameters: RAPMAX, NRAPB, NAZMB, ETMIN, ETSMIN and R_J. The motivation of building a grid was the high number of cells in the LAr calorimeter which could cause the algorithm to be slow. The normal values of NRAPB and NAZMB varied between 20 and 30 which produces a grid with 400 or more cells. On the other hand for the forward jet sample the average number of cells in the LAr which survived the noise cuts presented in section 2.6.1 is about 300, so to define a grid is not really necessary.

The need to have a well defined grid is the origin of the RAPMAX parameter, but if no grid is defined this parameter is not needed anymore. Also the fear of a slow jet algorithm motivated the ETMIN, so that not all cells could be considered initiators. This has the drawback that the amount of jets found depends on this completely artificial parameter, which is not really needed if the computer time used by the algorithm is reasonable.

Given that the reason to have so many parameters, namely the possibility of having too many cells as input of the algorithm is not supported by the data, and that all this extra parameters are artificial the algorithm was modified such that instead of filling a grid and using the coordinates (η, ϕ) of the cells of the grids, the cells of the LAr were directly used. With this the input parameters needed were only: ETSMIN and R_J.

There was other modification to the algorithm. Instead of the Snow Mass convention to add the momenta of the jet components a covariant convention was used here:

$$p_{\mu_j} = \sum p_{\mu_i}$$

where i runs over all cells forming a jet. This change is a matter of taste when dealing with data where it is not possible to assign a mass to each cell of the calorimeter, but in principle for MC studies at parton level where the four momentum of every parton is known, the correct option is to use a covariant convention to be able to deduce the four momentum of the original parton which produced the jet. As in this analysis no correction to parton level was attempted this modification is, as already said, a matter of taste, and as far as one definition is consistently used it is not important which one is used.

Appendix C

KT versus CONE jets

C.1 The KT algorithm

The KT jet algorithm [92] is a clustering algorithm in the Breit system which function as follows:

- For every pair of the input objects to the jet algorithm calculate
$$d_{ij} = \min(E_i, E_j)^2 \cdot 2 \cdot (1 - \cos\theta_{ij})$$
where E_i is the energy (in the Breit frame) of object i and $\cos\theta_{ij}$ is the angle between the momenta of both objects. Note that for small θ_{ij}, $\sqrt{d_{ij}}$ is the transverse momentum of the object with the smaller energy in relation to the other object.
- For all objects calculate $d_i = P_{T_i}^2$, where $\sqrt{d_i}$ is the transverse momentum of the object with respect to the remnant.
- In case $\min(d_i, d_{ij}) < y_{CUT}$ then if the minimum was d_i then this object is assigned to the remnant, if the minimum was d_{ij} then both objects are put together and built a new object with momentum $p^\mu = p_i^\mu + p^m u_j$. Afterwards the processed is started again with the new defined objects in place of the old ones.
- In case $\min(d_i, d_{ij}) < y_{CUT}$ the process is terminated and the remaining objects are the jets.

C.2 The files used

Monte Carlo events with the following characteristics were generated with LEPTO–MEPS version 6.3:

- An electron with more than 11 GeV was scattered between 160 and 173 degrees.
- Two jets with more than 2 GeV of transverse energy were found either with the CONE or the KT algorithm. One in the polar angle range between 3 and 25 degrees and the other with a polar angle bigger than 65 degrees.

This preselection was done at parton level and in the HERA system. These events were simulated to produce a detector level for them.

C.3 Comparing the algorithms

The behavior of the P_T, energy and polar angle of the jets in detector level with respect to hadron level was studied for different parameters of the algorithms for events where the forward jet had more than 5 GeV of transverse momentum in the HERA frame. It was found that the CONE algorithm is much more stable under variation of its parameter than the KT algorithm and that for the better value of their respective parameters ($y_{CUT} = 20$ and $R_{CONE} = 1$) both algorithms have a similar quality. This observations are summarized in figure C.1

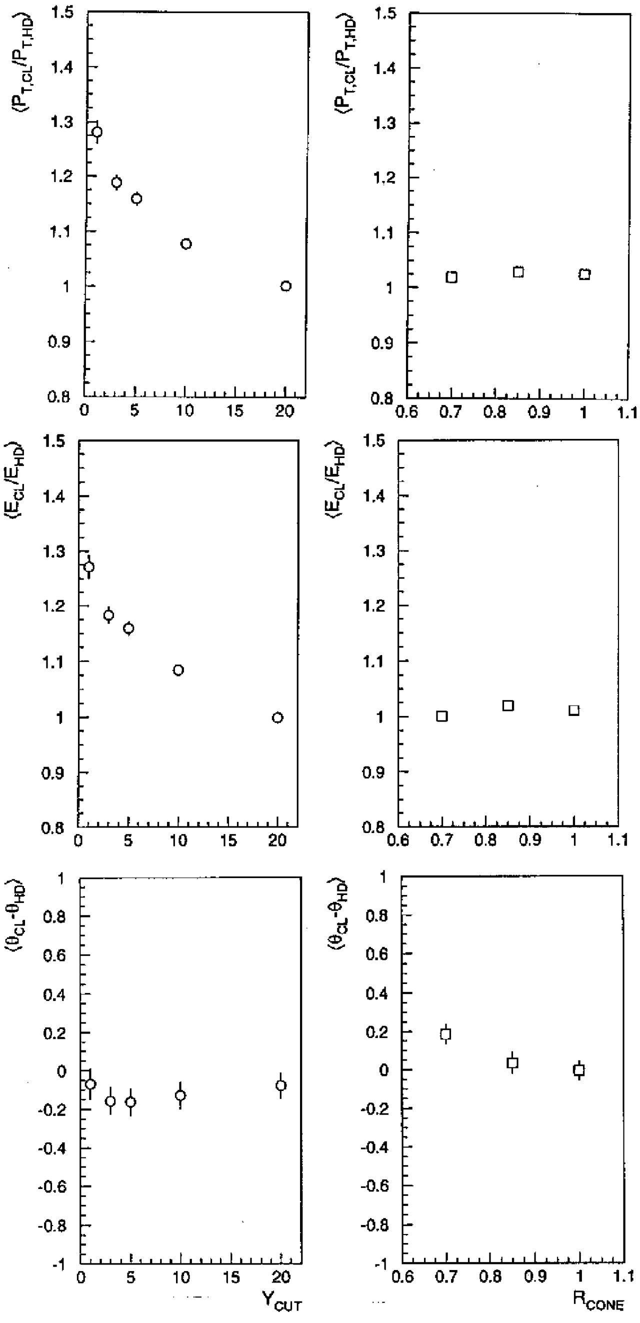

Figure C.1: KT versus CONE jet algorithms. The behavior of the relationship between the measurement in hadron and detector level for the P_T, energy E and polar angle θ of the jets for different values of the parameters of the jets algorithms is shown. In the left side are the results of the KT algorithm for different values of y_{CUT} and in the right side the CONE algorithm id presented for different values of the radius R_{CONE}. The subscripts CL and HD refer to measurements done at the detector or hadron level respectively.

Appendix D

The measured cross sections in tables

The following tables give the numerical values of the measured cross sections presented in chapter 5. Each table contains five columns. The first column contains the boundaries of the bins, where x is given by eq (1.4) and $\Delta\phi$ is the difference in the azimuthal angles of the scattered lepton and the forward jet. The second column gives the value of the cross section, the third the statistical error, the forth the total positive error and the fifth column the total negative error. The total errors are obtained by adding in quadrature the statistic and systematic error bars. The total luminosity considered was 2.78 pb^{-1}.

x bin	σ [pb]	stat. [pb]	tot+ [pb]	tot− [pb]
0.0001–0.0005	81	12	16	18
0.0005–0.001	171	8	27	27
0.001–0.0015	112	6	16	18
0.0015–0.002	69	5	13	10
0.002–0.003	67	5	10	13
0.003–0.004	32	3	5	7

Table D.1: Values of the H1 data points of figure 5.1

x bin	σ [pb]	stat. [pb]	tot+ [pb]	tot− [pb]
0.0001–0.0005	55	8	12	11
0.0005–0.001	85	5	10	13
0.001–0.0015	46	4	10	9
0.0015–0.002	30	3	7	5
0.002–0.003	20	3	3	5
0.003–0.004	8	2	4	4

Table D.2: Values of the H1 data points of figure 5.5 a)

x bin	σ [pb]	stat. [pb]	tot+ [pb]	tot− [pb]
0.0001–0.0005	26	9	9	11
0.0005–0.001	87	6	19	16
0.001–0.0015	67	5	8	10
0.0015–0.002	38	4	8	9
0.002–0.003	47	4	8	9
0.003–0.004	24	3	3	5

Table D.3: Values of the H1 data points of figure 5.5 b)

x bin	σ [pb]	stat. [pb]	tot+ [pb]	tot− [pb]
0.0001–0.0005	35	5	7	8
0.0005–0.001	42	3	8	8
0.001–0.0015	26	2	6	5
0.0015–0.002	19	2	5	4
0.002–0.003	21	2	4	5
0.003–0.004	11	2	3	3

Table D.4: Values of the H1 data points of figure 5.5 c)

x bin	σ [pb]	stat. [pb]	tot+ [pb]	tot− [pb]
0.0001–0.0005	43	13	13	14
0.0005–0.001	134	8	21	24
0.001–0.0015	93	6	13	15
0.0015–0.002	53	5	10	9
0.002–0.003	46	5	8	9
0.003–0.004	21	3	4	6

Table D.5: Values of the H1 data points of figure 5.5 d)

$\Delta\phi$ bin [°]	σ [pb]	stat. [pb]	tot+ [pb]	tot− [pb]
0–30	63	5	9	10
30–60	76	5	11	11
60–90	89	8	14	14
90–120	94	8	16	16
120–150	101	8	15	18
150–180	120	7	21	24

Table D.6: Values of the H1 data points of figure 5.9

$\Delta\phi$ bin [^{o}]	σ [pb]	stat. [pb]	tot+ [pb]	tot– [pb]
0–30	36	5	6	7
30–60	40	4	8	7
60–90	45	7	9	9
90–120	45	7	9	10
120–150	42	7	9	11
150–180	51	4	10	10

Table D.7: Values of the H1 data points of figure 5.11 a)

$\Delta\phi$ bin [^{o}]	σ [pb]	stat. [pb]	tot+ [pb]	tot– [pb]
0–30	28	3	6	5
30–60	36	3	5	5
60–90	43	4	7	7
90–120	49	4	9	8
120–150	60	4	9	9
150–180	69	5	13	14

Table D.8: Values of the H1 data points of figure 5.11 b)

$\Delta\phi$ bin [^{o}]	σ [pb]	stat. [pb]	tot+ [pb]	tot– [pb]
0–30	9	1	2	2
30–60	12	1	3	3
60–90	16	2	4	3
90–120	21	3	5	5
120–150	42	3	7	7
150–180	62	4	12	13

Table D.9: Values of the H1 data points of figure 5.11 c)

$\Delta\phi$ bin [^{o}]	σ [pb]	stat. [pb]	tot+ [pb]	tot– [pb]
0–30	55	6	9	10
30–60	66	5	10	8
60–90	74	10	12	15
90–120	78	8	14	15
120–150	59	10	12	15
150–180	57	5	11	12

Table D.10: Values of the H1 data points of figure 5.11 d)

Bibliography

[1] W. K. H. Panofsky, Proc. of the 14th. International Conference on High Energy Physics, Vienna (1968) p. 23; SLAC–PUB–0502 (1968).

W. Albrecht *et al.*, 4th. Int. Symp. on Electron and Photon Interactions, Liverpool (1969); DESY preprint 69–046.

[2] See for example Perturbative Quantum Chromodynamics, ed. A. H. Mueller, World Scientific, Singapure (1989).

QCD 20 years later, ed. H. A. Kastrup and P. M. Zerwas, World Scientific, Singapure (1993).

[3] S. Bentvelsen, P. Kooijman and J. Engelen, Proc. of the Workshop on Physics at HERA, ed. W. Buchmüller and G. Ingelman, Hamburg (1992) 23.

[4] K.C. Hoeger, Proceedings of the Workshop on Physics at HERA, ed. W. Buchmüller and G. Ingelman, Hamburg (1992) 43.

[5] U. Bassler and G. Bernardi, Nucl. Inst. and Meth. A361 (1995) 197.

[6] J.C. Collins, D.E. Soper and G. Sterman in Perturbative Quantum Chromodynamics, ed. A.H. Mueller, (World Scientific, Singapore, 1989) .

[7] K.G. Wilson, Phys. Rev. 179 No. 5 (1969) 1499.

[8] Yu. L. Dokshitzer, V. A. Khoze, A. H. Mueller and S. I. Troyan, Basics of perturbative QCD (Editions Frontieres, France, 1991)

[9] M. Ciafaloni, Nucl. Phys. **B296** (1988) 49;
S. Catani, F. Fiorani and G. Marchesini, Phys. Lett. **B234** (1990) 339; Nucl. Phys. **B336** (1990) 18.

[10] V.N. Gribov and L.N. Lipatov, Sov. J. Nucl. Phys. **15** (1972) 438;
G. Altarelli and G. Parisi, Nucl. Phys. **B126** (1977) 298;
Yu. L. Dokshitzer, Sov. Phys. JETP **46** (1977) 641.

[11] E.A. Kuraev, L.N. Lipatov and V.S. Fadin, Phys. Lett. **B60** (1975) 50; Sov. Phys. JETP **44** (1976) 443; Sov. Phys. JETP **45** (1977) 199.
Ya. Ya. Balitsky and L.N. Lipatov, Sov. J. Nucl. Phys. **28** (1978) 822.

[12] L. V. Grivbov, E. M. Levin and M. G. Ryskin, Phys. Rep. 100 (1983) 1.

[13] A.H. Mueller, Nucl. Phys. B (Proc. Suppl.) **18C** (1990) 125; J. Phys. **G17** (1991) 1443.

[14] D. H. Perkins, Introduction to high energy physics, Addison–Wesley, 1987.

[15] F. Halzen, A. D. Martin, Quarks and Leptons, John Wiley & Sons, 1984.

[16] J. Kwieciński, A.D. Martin, P.J. Sutton, Phys. Rev. **D46** (1992) 921.

[17] J.R. Forshaw and P.N. Harriman, Phys. Rev. **D46** (1992) 3778.

[18] J.C. Collins and P.V. Lanshoff, Phys. Lett. **B276** (1992) 196.

[19] J. Bartels and H. Lotter Phys. Lett. **B309** (1993) 400.

[20] CTEQ Collaboration: H.L. Lai *et al.*, MSUHEP–60426, Jun 1996.

[21] A.D. Martin, R.G. Roberts and W.J. Stirling, Phys.Lett. **B387** (1996) 419.

[22] A.D. Martin, R.G. Roberts and W.J. Stirling, Phys. Lett. **B354** (1995) 155.

[23] CTEQ Collaboration: H.L. Lai *et al.*, Phys. Rev. **D51** (1995) 4763.

[24] M. Glück, E. Reya and A. Vogt, Z. Phys **C67** (1995) 433.

[25] A. M. Cooper–Sarkar and W. J. Stirling, J. Phys. G: Nucl. Part. Phys. **19** (1993) 1601.

[26] ZEUS Collaboration: M.Derrick *et al.*, Phys. Lett. **B316** (1993) 412.

[27] H1 Collaboration: I. Abt *et al.*, Nucl. Phys. **B407** (1993) 515.

[28] ZEUS Collaboration: M. Derrick *et al.*, Z. Phys. **C70** (1996) 1.

[29] H1 Collaboration: S. Aid *et al.*, Nucl.Phys. **B470** (1996) 3 .

[30] A. De Roeck, J. Phys. **G19** (1993) 1549.

[31] I. Bojak and M. Ernst, preprint DO–TH 96/18.

[32] H1 Collaboration: I. Abt *et al.*, Z.Phys. **C63** (1994) 377.

[33] L. Lönnblad, Comp. Phys. Comm. **71** (1992) 15.

[34] L. Lönnblad, Z. Phys. **C65** (1995) 285;
L. Lönnblad, Proc. of PHOTON'95, eds. D.J. Miller, S.L. Cartwright and V.A. Khoze, Sheffield (1995) 443.

[35] A.H. Mueller, Nucl. Phys. **B415** (1994) 373.

[36] K. Golec–Biernat, J. Kwieciński, A.D. Martin and P.J. Sutton, Phys.Lett. **B335** (1994) 220; Phys. Rev. **D50** (1994) 217.

[37] ZEUS Collaboration: Proc. of Int. Europhysics Conf. on HE Physics, Brussels, 1995. Ref. 0391.

[38] H1 Collaboration: S. Aid *et al.*, Phys.Lett. **B356** (1995) 118.

[39] G. Ingelman, Proc. of the Workshop on Physics at HERA, eds. W. Buchmüller and G. Ingelman, Hamburg (1992) 1366.

A. Edin, G. Ingelman and J. Rathsman, LEPTO 6.5, DESY preprint 96–057.

[40] A. Edin, J. Rathsman and G. Ingelman, Phys. Lett. **B**366 (1996) 371.

[41] J. Bartels, M. Besancon, A.De Roeck, J. Kurzhöfer, Proc. of the Workshop on Physics at HERA, eds. W. Buchmüller and G. Ingelman, Hamburg (1992) 203.

[42] J. Kwieciński, A.D. Martin, P.J. Sutton, Phys. Rev. **D46** (1992) 921; Phys. Lett. **B287** (1992) 254; Nucl. Phys. B (Proc. Suppl.) **29A** (1992) 67.

[43] J. Bartels, A. De Roeck and M. Loewe, Z. Phys. **C54** (1992) 635; Nucl. Phys. B (Proc. Suppl.) **29A** (1992) 61.

[44] W.K. Tang, Phys. Lett. **B278** (1992) 363.

[45] J. Bartels *et al.*, Phys. Lett. **B**384 (1996) 300.

[46] J. G. Contreras, Proc. of the XXXI Rencontres de Moriond in QCD and high energy hadronic interactions, ed. by J. Tran Thanh Van, Editions Frontieres (1996) 411.

[47] B.H. Wiik, Proc. of the Workshop on Physics at HERA, eds. W. Buchmüller and G. Ingelman, Hamburg (1992) 1.

[48] N. Gogitidze, S. Levonian, An offline luminosity determination for the 1995 H1 e^+p data, H1 internal note H1–02/96–471.

[49] H1 Collaboration: I. Abt *et al.*, H1 report FH1–96–01, submitted in abbreviated form to Nucl. Instr. and Meth.

[50] ZEUS Collaboration, DESY–HERA–ZEUS 1 (1986)

[51] HERA–B Collaboration, DESY–PRC 93–04.

[52] HERMES Collaboration, DESY–PRC 90–01.

[53] F. Sefkow *et al.*, Experience with the First Level Trigger of H1, H1 internal note H1–11/94–407.

[54] R. Prosi, Pedestrian's guide to the L4 filter farm, H1 internal note H1–11/94–412.

[55] J. Bürger *et al.*, Nucl. Instr. and Meth. **A279** (1989) 217.

[56] T. Heatherington *et al.*, ToF timing correlation for upstream vertex events, H1 internal note H1–02/94–340.

[57] H1 BEMC Group: J. Ban *et al.*, Nucl. Instr. and Meth. A372 (1996) 399.

[58] BEMC Group, Calibration and reconstruction of the BEMC, H1 internal note H1–08/92–234.

[59] H1 Calorimeter Group: B. Andrieu *et al.*, Nucl. Instr. and Meth. **A336** (1993) 460.

[60] J. Gayler *et al.*, Reprocessing of LAr data and LAr MC for 1994, H1 internal note H1–01/95–421.

[61] L. Goerlich, H. P. Wellisch, Documentation of the LAr clustering, H1 internal note H1–12/91–204.

[62] J. P. Kubenka *et al.*,Hadronic Calibration of the H1 LAr Calorimeter using Software Weighting Techniques, H1 internal note H1–02/94–346.

[63] Ç. Işsever, Diploma thesis, Universität Dortmund.

[64] J. G. Contreras, Minutes of the Data Quality Meeting, 12.03.96.

[65] H1 Collaboration: S. Aid *et al.*, Z.Phys. C66 (1995) 529.

[66] H1 Collaboration: *Luminosity Measurement in the H1 Experiment at HERA*, contributed paper to the International Conference on High Energy Physics, Warsaw 1996, ICHEP96–pa17–026.

[67] T. Kurča, PhD thesis, Universität Hamburg, 1993.

[68] S. Levonian, A. Panitch, Treatment of the Proton Satellite Bunches in 1994 Data, H1 internal note H1–09/95–454.

[69] F. Charles *et al*, Photoproduction as background in Deep Inelastic Scattering at low x, H1 internal note H1–09/94–380.

[70] C. W. Fabjan, Calorimetry in high–energy physics, CERN–EP 85–54.

[71] B. R. Webber, Proceedings of Hadronic aspects of collider physics, ed. by M. P. Locher, Zouz, Switzerland, PSI (1994) 49.

[72] J. E. Huth *et al*, Proceedings of the 1990 DPF summer study on high energy phisics, Snowmass, Colorado, ed. E. L. Berger (World Scientific, Singapur,1992) 134.

[73] M. H. Seymour, Jets in QCD, CERN–TH 95–176.

[74] J. Kurzhöfer, The QJCONE jet algorithm and its implementation in H1PHAN, H1 internal note H1–09/94–375.

[75] H1 Collaboration, Technical Proposal to Upgrade the Backward Scattering Region of the H1 Detector, PRC 93/02, March 8, 1993.

[76] H1 Collaboration, Guide to Simulation program H1SIM, 17 October 1991.

[77] H1 Collaboration, H1REC code (no manual).

[78] I. Manno, Introduction to the Monte–Carlo method, INFN/AE–94/16.

[79] I. G. Knowles *et al.*, QCD event generatores, Proc. of Physics at Lep 2, eds. G. Altarelli, T. Sjöstrand, F. Zwirner, CERN 96–01 (1996) Vol. 2 p. 103.

[80] T. Sjöstrand, Comp. Phys. Comm. **82** (1994) 74.

[81] A. Kwiatkowski, H. Spiesberger, H.–J. Möring, Proc. of the Workshop on Physics at HERA, ed. W. Buchmüller and G. Ingelman, Hamburg (1992) 1294.

[82] G. A. Schuler, H. Spiesberger, Proc. of the Workshop on Physics at HERA, ed. W. Buchmüller and G. Ingelman, Hamburg (1992) 1419.

[83] G. Marchesiani *et al.*, Comp. Phys. Comm. **67** (1992) 465.

[84] N. Brook *et al.*, Proc. of the Workshop Future Physics at HERA, ed. G. Ingelman, A. De Roeck and R. Klanner, Hamburg (1996) 613.

[85] P. N. Harriman, A. D. Martin, W. J. Stirling and R. G. Roberts, Phys. Rev. **D42** (1990) 798.

[86] J. Rathsman, SLAC–PUB–7344, (29, Oct,1996).

[87] A. Pantich, PhD thesis, Université Libre de Bruxelles, 1996.

[88] L. Favart, PhD thesis, Université Libre de Bruxelles, 1995.

[89] M. Hütte, Ph. D. Thesis, Universität Dortmund, 1996.

[90] J. Kurzhöfer, PhD thesis, Universität Dortmund, 1995.

[91] W. Bartel *et al.*, Z. Phys. C **33** (1986) 23.

[92] S. Catani, Yu. L. Dokshitzer, B. R. Weber, Phys. Lett. **285B** (1992) 291.

[93] P. Pfeifenschneider, B.Sc. Thesis, Rheinisch–Westfälische Technische Hochschule Aachen, (1994).

[94] G. Kramer and S. Salesch, Phys. Lett. B317 (1993) 218 and Phys. Lett. B333 (1994) 519.

[95] J. Gayler, Proceedings of the energy scale working group, (5, Feb.,1996).

[96] E. Mroczko, Ph.D. thesis in preparation, Institute of Nuclear Physics in Cracow .

[97] G. D'Agostini, DESY preprint 95–242.

[98] A. De Roeck, personal communication based on the work presented in ref. [45].